ABSTRACT

Title of thesis: APPLICATION OF UNCERTAINTY QUANTIFICATION OF TURBULENCE INTENSITY ON AIRFOIL AERODYNAMICS

Atif Salahudeen, Masters of Science, 2017

Thesis directed by: Dr. James Baeder
Department of Aerospace Engineering

Traditional CFD results have a number of freestream inputs. In the physical world, these input conditions often have some uncertainty associated with them. However, this uncertainty is often omitted from the CFD results. The effects of uncertainty in CFD can be determined through application of Uncertainty Quantification (UQ). The primary objective of the present work is to determine the effect of uncertainty in freestream turbulence intensity (FSTI) on the coefficients of lift, drag, and moment for four different airfoils: S809, NACA 0012, SC1095, and RC(4)-10. In this work, the Monte Carlo method is used to calculate the sensitivities of the aerodynamic coefficients to Gaussian distributions of uncertainty in FSTI over a range of angles of attack (AOA) at various Reynolds numbers and Mach numbers. However, the Monte Carlo method would require hundreds of thousands of CFD calculations in order to

converge to the correct results. A surrogate surface is therefore generated using a parametric study using the in-house flow solver OVERTURNS. Rather than run a separate CFD run for each Monte Carlo run, all of the results can be attained virtually instantaneously via the surrogate surface.

The UQ analysis shows how varying these parameters affects the sensitivies of the aerodynamic coefficients to uncertainty in FSTI. In most cases, the response is nearly Gaussian and the mean response is not too different from the discrete FSTI response without uncertainty. However, the output standard deviation for drag and pitching moment can become large when the transition location changes rapidly with changing FSTI.

APPLICATION OF UNCERTAINTY QUANTIFICATION OF TURBULENCE INTENSITY ON AIRFOIL AERODYNAMICS

by

Atif Salahudeen

Thesis submitted to the Faculty of the Graduate School of the
University of Maryland, College Park in partial fulfillment
of the requirements for the degree of
Masters of Science
2017

Advisory Committee:
Dr. James Baeder, Chair/Advisor
Dr. Inderjit Chopra
Dr. Anubhav Datta

Acknowledgments

First and foremost I would like to express my gratitude to God Almighty for showering me with His blessings and enabling me to achieve all that I have achieved.

This thesis is the result of an amazing supporting cast whose help was invaluable. I would like to thank my advisor, Dr. James Baeder, for his wisdom, guidance, and patience. I would have never been able to overcome the many challenges in my research without his help. I would also like to thank my committee members, Dr. Inderjit Chopra and Dr. Anubhav Datta, for the time they spent to serve on my committee as well as the invaluable feedback they provided.

Next, I would like to thank Dr. Nishan Jain, Bumseok Lee, Dr. Camli Badrya, and Dylan Jude for all of their help with this research, their constructive criticism, and for their patience with my endless questions. I would also like to thank all of my friends, especially my good friend Luthfe Siddique, for making both my undergraduate and graduate experiences at the University of Maryland truly enjoyable.

Finally, I am forever indebted to my parents, grandmothers, and sister. Without their unwavering love and support, I would not be where I am today.

Contents

List of Tables

List of Figures

Nomenclature

a	Speed of sound $= \sqrt{\gamma R T}$
c	Chord length
C_d	Sectional drag coefficient $= \dfrac{D}{\frac{1}{2}\rho_\infty U_\infty^2 c}$
C_f	Sectional friction coefficient $= \dfrac{\tau_w}{\frac{1}{2}\rho_\infty U_\infty^2}$
C_l	Sectional lift coefficient $= \dfrac{L}{\frac{1}{2}\rho_\infty U_\infty^2 c}$
C_p	Pressure coefficient $= \dfrac{p - p_\infty}{\frac{1}{2}\rho_\infty U_\infty^2}$
d	Nearest wall distance
D	Drag force
e	Internal energy
H	Shape factor $= \dfrac{\delta^*}{\theta}$
k	Turbulent kinetic energy $= \dfrac{1}{2}\left[\overline{(u')^2} + \overline{(v')^2}\right]$
L	Reference length / Lift force
M	Mach number
p	Static pressure
Pr	Prandtl number
r	Distance along rotor blade non-dimensionalized by rotor radius
Re	Reynolds number $= \dfrac{\rho_\infty U_\infty L}{\mu_\infty}$
Re_θ	Reynolds number based on momentum thickness $= \dfrac{\rho_\infty U_\infty \theta}{\mu_\infty}$
$Re_\theta t$	Re_θ at transition onset location
$\overline{Re_\theta t}$	Transport variable for $Re_\theta t$

Re_v	Vorticity Reynolds number $= \dfrac{\rho d^2 \Omega}{\mu}$
t	Time
Tu_∞	Freestream turbulence intensity $= \dfrac{\sqrt{2k/3}}{U_\infty}$
u, v	Flow velocity components along Cartesian coordinate directions
u', v'	Turbulent fluctuation velocities along Cartesian coordinate directions
$\overline{u_i' u_j'}$	Time-average of Reynolds stress tensor components
U_∞	Total freestream velocity magnitude
U_e	Boundary layer edge velocity magnitude
x, y	Cartesian coordinate directions

Symbols

δ	Boundary layer thickness
$\delta*$	Displacement thickness
γ	Ratio of specific heats / Intermittency
λ	Pressure gradient parameter $= \dfrac{\rho \theta^2}{\mu} \dfrac{dU}{ds}$
μ	Molecular viscosity / Mean
μ_t	Turbulent/Eddy viscosity
ω	Specific dissipation rate
Ω	Vorticity magnitude
ρ	Density
σ	Standard deviation
τ_w	Wall shear stress
θ	Momentum thickness

Subscripts

e	Boundary layer edge
i	Inviscid quantities
v	Viscous quantities
∞	Freestream flow variables

Abbreviations

AOA	Angle of Attack
CFD	Computational Fluid Dynamics
DES	Detached Eddy Simulation
FSTI	Freestream Turbulence Intensity
MUSCL	Monotone Upstream-centered Schemes for Conservation Laws
NREL	National Renewable Energy Laboratory
OVERTURNS	Overset Transonic Unsteady Rotor Navier-Stokes
PDF	Probability Density Function
QOI	Quantity of Interest
RANS	Reynolds-Averaged Navier Stokes
UQ	Uncertainty Quantification
V& V	Verification and Validation

Chapter 1

Introduction

1.1 Motivation

The field of computational fluid dynamics (CFD) has witnessed advances in several different areas, including advanced mesh generation techniques, increased solution accuracy, and reduced computational costs. However, while CFD is able to provide quantitative data through numerical simulation, the effect of uncertainties in the input quantities is often omitted. Therefore, reliability tests often resort to physical tests rather than CFD. Yet, it is possible to provide this information through numerical simulation via uncertainty quantification (UQ). UQ is the science of determining how uncertainties in inputs propagate through a system and affect the final results. It draws heavily from statistics and can be applied to CFD to provide additional information to augment solution results, such as confidence intervals and statistical variance. This information can aid in sensitivity analysis, design, and reliability analysis.

UQ can be defined within the framework of Verification and Validation (V&V). Verification is the process of determining whether the equations modeling a system are being solved correctly. This field essentially deals with the mathematics of the model. When applied to CFD, verification traditionally deals with mesh refinement and/or use of high order methods. On the other hand, validation compares how well the model compares against the real world. The UQ analysis presented in this work falls under the validation regime, as it attempts to take physical uncertainties into account for CFD simulations.

The need for UQ in CFD stems from uncertainties present in the real world that are essentially ignored by traditional CFD analysis. While these uncertainties may be small in magnitude, they may lead to varying results. The use of UQ allows for improved decision-making, more accurate validation, and more robust designs. In terms of decision-making, UQ can determine how confident one can be that the results obtained from a CFD simulation are correct, given certain uncertainties in the input. UQ can also be used in validation to bridge the gap between experiments and simulations by accounting for the physical uncertainties which are absent from the simulations. Finally, UQ can be utilized to determine the trade offs between an optimal design with high sensitivity to certain parameters and a sub-optimal design that is not as sensitive to those parameters. All of these benefits can be primarily achieved by determining the true mean and quantifying the variance present for quantities of interest.

One particular area where UQ can be utilized is boundary layer transition modeling in CFD. The transition from laminar to turbulent flow is a very significant phenomenon, especially for rotorcraft. This transition results in an increase in viscous drag over various rotorcraft components, as well as an increase in heat transfer, and possible flow separation. It is therefore desirable to design airfoils and aircraft which promote laminar flow and delay the onset of transition.

Transition is highly dependent on a number of factors, including the freestream turbulence intensity (FSTI), stream-wise pressure gradient, surface curvature and roughness, and compressibility. It is therefore important to determine how uncertainties in these quantities propagate and how sensitive aerodynamic quantities such as lift, drag, and moment are to these uncertainties. Determining this sensitivity will allow for better decision-making, validation, and design. The present work will focus on the effect of uncertainty in FSTI specifically.

Drag is subject to strong non-linear effects; this makes UQ extremely important when applied to quantities affecting drag, like FSTI. As mentioned previously, UQ can be used to determine the sensitivity of lift, drag, and moment to input quantities such as FSTI. In addition, UQ can be used to calculate the expected aerodynamic coefficients, given specified uncertainty in the input. Since the aerodynamic quantities are not necessarily linear as FSTI varies, it cannot be assumed that the expected quantities are equivalent to the values obtained using the expected FSTI. UQ can therefore be used to determine how valid such an assumption would be as well as calculate more accurate values of lift, drag, and moment, given the input uncertainty. This is achieved in the present work by applying the

UQ techniques (to be described later) to determine the true means and expected standard deviations for the coefficients of lift, drag, and moment, given a specific uncertainty distribution in FSTI.

1.2 Boundary Layer Transition

When air flows over a surface, a boundary layer forms over the surface. The boundary layer is a thin region in contact with the surface and is formed due to presence of friction and viscosity. The friction/viscosity present between the surface and the air slows the air down and prevents it from moving at freestream conditions. The boundary layer is defined as the region extending up to the point where the flow velocity is equal to 99% of the freestream velocity. It may initially be in a laminar state. However, as the air moves over the surface, the boundary layer may transition from laminar flow to turbulent flow. For a description of laminar and turbulent flow, see section 1.2.1 below. There are a number of factors that may contribute to the transition from laminar to turbulent flow, including freestream turbulence intensity, surface roughness, surface curvature, vibrations, and adverse pressure gradients. In order to minimize drag, it is desirable to delay the onset of boundary layer transition.

1.2.1 Laminar, Turbulent, and Transitional Flow

Laminar flow is a term used in fluid dynamics to describe a flow in which the fluid moves in parallel layers. There is no lateral mixing, cross-currents, eddies, or swirls present in this flow as the layers flow without any interaction with each other. The flow can be characterized as “smooth.” Typically, laminar flow occurs at low flow velocities.

On the other hand, turbulent flow is characterized as “rough”, with irregular/chaotic flow paths. The turbulence is due to the inertial forces from the velocity of the flow dominating the viscous forces of the flow. Turbulent flows contain unsteady vortices of varying sizes, resulting in the rotationality of the flow. The flow creates eddies, which are made up of smaller eddies, which in turn are made up of even smaller eddies, and so on. Thus, in turbulent flow, there is mixing between the various layers in the boundary layer. These eddies dissipate kinetic energy as heat, resulting in an increase in skin friction drag when compared to laminar flow. This increase in drag is the primary reason why laminar flow, turbulent flow, and the transition between them, are important to the aerospace field.

1.2.2 Reynolds Number

The *Reynolds number* is a non-dimensional parameter that is used as a general measure of turbulence. The Reynolds number is defined as the ratio of the inertial forces of a fluid to the viscous forces of the fluid and is defined by Eq. 1.1:

$$Re = \frac{\rho U L}{\mu} \tag{1.1}$$

In this equation, ρ is the fluid density, U is the fluid velocity, and L is the characteristic length, and μ is the fluid's dynamic viscosity. For flows with a low

Reynolds number, the viscous forces are dominant and the Reynolds number is laminar. Turbulent flows are dominated by inertial forces and therefore have high Reynolds numbers.

1.2.3 Transition

Transitional flow describes the flow as it changes from laminar to turbulent flow or vice versa. As the flow moves across a surface, it may begin to undergo transition from laminar flow to turbulent flow. Usually transition is defined as the region during which the skin friction coefficient (C_f) increases to its fully turbulent value. Fig 1.1 illustrates how transition affects the skin friction over a flat plate. The momentum thickness Reynolds number (Re_θ) also increases during transition. The increase in skin friction leads to an increase in drag and a transfer of heat to the surface. In addition, the flow may eventually reverse and the boundary layer may separate from the surface [1]. During transition, the velocity of the flow no longer varies uniformly across the boundary layer and oscillations begin to appear in the flow. The flow is no longer steady with respect to time. Small eddies begin to form in the flow. As the eddies grow, the flow transitions into turbulent flow. This is illustrated in Fig. 1.2. Fig. 1.3 shows a comparison between the eddy viscosity plots for a fully turbulent case and a case with transition. As can be seen from the figure, the eddy viscosity decreases when the transition model is applied when compared to the fully turbulent solution.

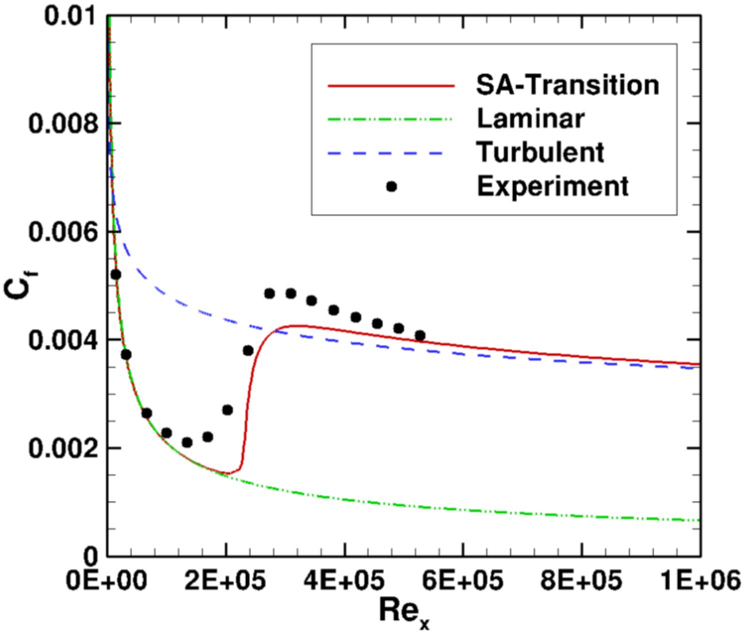

Figure 1.1: Skin friction over flat plate, Tu = 2.0% (reproduced from [6])

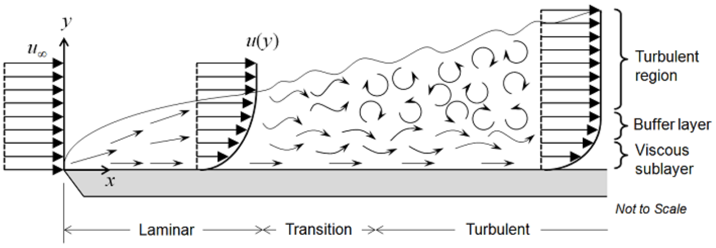

Figure 1.2: Boundary layer transition (reproduced from Comsol website)

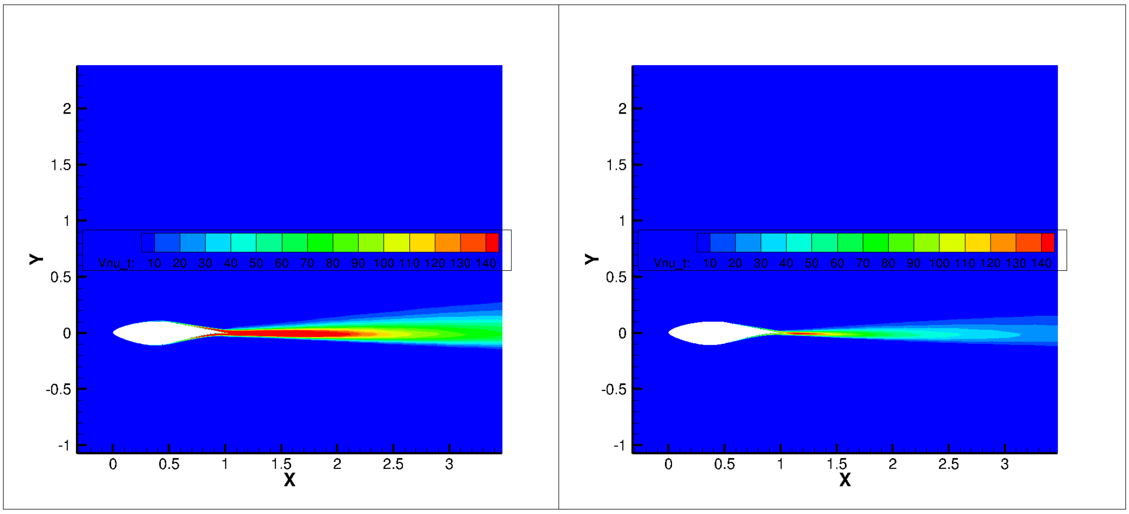

(a) Eddy viscosity field plot - fully turbulent (b) Eddy viscosity field plot - transition

Figure 1.3: S809 Airfoil at Mach = 0.2, Re = 2×10^6, AOA = 1 degree, FSTI = 0.05%

1.2.4 Physical Mechanisms of Transition

One way to approach the transition of a laminar boundary layer is to treat the transition as a "non-linear response of a very complicated oscillator - the laminar boundary layer - to a random forcing function" with "infinitesimal amplitude compared with the appropriate laminar-flow quantities" [2]. This forcing function's characteristics (i.e. amplitude, frequency, and phase) are determined by *receptivity*, a concept introduced by Morkovin [3]. Receptivity refers to the way in which a disturbance enters the boundary layer. The disturbances induce a response. The response amplitude grows until it reaches the "breakdown phase". During the breakdown phase, spots of intermittent turbulence develop in the flow and begin to grow. As these spots grow, they begin to merge with one another until the entire flow becomes turbulent [4].

1.2.5 Intermittency

One way to quantify the transition from laminar to turbulent flow is to use the *intermittency factor*, γ [5]. As the flow transitions, intermittent turbulent spots appear and grow. γ is defined as the fraction of time any point spends in turbulent flow (i.e. one of these intermittent turbulent spots). When γ is equal to one, this means that airflow at this location is now fully turbulent, whereas when γ is equal to zero, the flow is laminar.

1.2.6 Types of Transition

There are a number of different types of transition, including natural transition, separation-induced transition, bypass transition, and crossflow transition. Each type of transition will be reviewed briefly, with the exception of crossflow transition, since the scope of the present work is limited to two-dimensional airfoils.

Natural Transition

Natural transition is the most common form of transition for aircraft. For this type of transition, transient growth is negligible. The initial disturbances are small and breakdown is reached through the growth of the disturbances via linear processes. These processes include Tollmien-Schlichting, Gortler, and crossflow instabilities [6]. Tollmien-Schlichting waves are free disturbances that are the normal modes of the boundary layer. Gortler and cross-flow instabilities appear in three-dimensional flows. Gortler instabilities are induced by concave surface curvature while crossflow instabilities manifest due to sweep and pressure gradients. Linear stability theory and the Orr-Sommerfeld equations [7, 8] can be used to predict this kind of transition accurately. A depiction of natural transition induced by Tollmien-Schlichting waves is shown in Fig. 1.4.

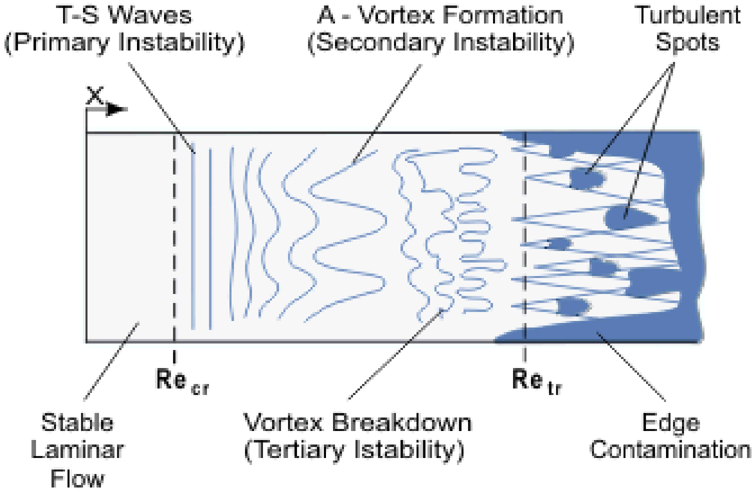

Figure 1.4: Natural transition due to Tollmien-Schlichting waves (reproduced from White 1991)

Separation-Induced Transition

Another type of transition is *separation-induced transition.* This process occurs in the presence of a strong adverse pressure gradient. The pressure gradient causes the laminar boundary layer to separate over a “laminar-separation bubble” (Fig. 1.5). The boundary layer then undergoes rapid transition before reattaching as a turbulent boundary layer. For low Reynolds numbers, the separation bubble can extend up to 50% of the airfoil chord, resulting in significant amounts of viscous drag. Stall is induced when the adverse pressure gradient is increased to the point where the bubble "bursts," causing the flow to remain unattached.

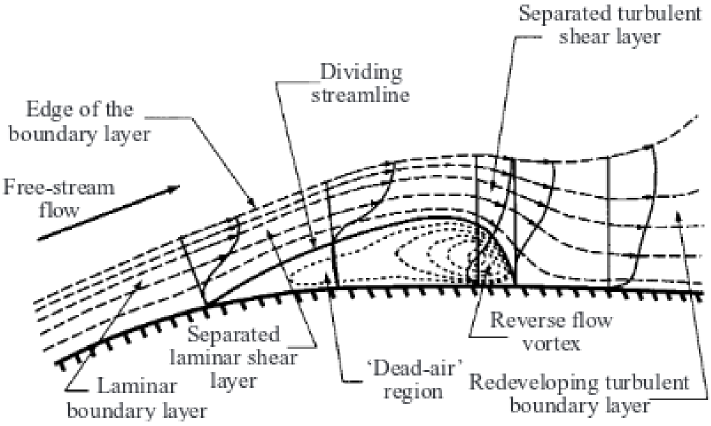

Figure 1.5: Flow structure of laminar-separation bubble (reproduced from Horton 1968)

Bypass Transition

When the initial disturbance amplitude is relatively large, the transition may *bypass* the stage of linear growth and directly reach the breakdown phase [3]. This is known as *bypass transition*. The large initial disturbances associated with this type of transition are typically due to a high level of freestream turbulence intensity (FSTI) or surface roughness. In bypass transition, the intermittent turbulent spots form quickly. This type of transition has been observed experimentally and is most common in turbomachinery, where high FSTI levels are present in the wake of upstream blade rows. However, the phenomenon cannot be described by linear stability theory due to the non-linear growth of the disturbances. Bypass transition is still not well understood and is a topic of ongoing research.

1.2.7 Transition Modeling

In CFD, transition models predict a “transition zone”, in which the flow is in between the laminar and turbulent states. The transition models are then incorporated into the flow solvers in order to simulate transition within the solver. There are a number of different transition models in use today, ranging from models based on hydrodynamic stability theory [9, 12] to correlation-based models [6, 16]. The first category involves using linear stability analysis to determine where transition occurs. The complete unsteady Navier-Stokes equations are linearized locally. The Orr-Sommerfeld stability equations can then be obtained, which are used to check if the disturbance amplitude grows or decays. The change in disturbance amplitudes determines when transition occurs. On the other hand, correlation models use the relationship between transition location and certain quantities, such as intermittency and transition momentum thickness Reynolds number ($Re_{\theta t}$) to predict the transition location [6].

There are a number of transition models currently in use in CFD. These models include the e^N model [12], the K-V model [10], the Langtry-Menter Model [16], and the Medida model [6] which is derived from the Langtry-Menter model. A brief description of each of these models is presented here.

The e^N Transition Model

The e^N transition model is a linear stability based model that utilizes the Orr-Sommerfeld equations to calculate the growth of spatial disturbances. The model compares the initial unstable amplitude to the amplitude corresponding to the most unstable frequency. Transition occurs when the latter exceeds the former by more than e^N . Typically, N ranges between 8 and 10 [10]. This method is derived from an eigenvalue analysis of the Orr-Sommerfeld equations, with the assumption that viscous parallel flow is present. However, this assumption is not necessarily valid. This is addressed by the linear Parabolized Stability Equations (PSE) method. A non-linear PSE method has also been developed to take into account bypass transition, roughness-induced transition, and other non-linear phenomena [11].

In order to implement this model, the laminar velocity and temperature profiles have to be calculated at different locations in the flow. The local linear stability equations (or the PSE) are then solved in order to obtain the local amplification rates. N is then calculated by integrating the local amplification growth rate along the streamline. Transition takes place once N exceeds a certain value [12]. Some versions of the model use a database to evaluate the instability data. The inputs to the database are determined via two equations: 1) the von Karman integral relation and 2) the kinetic energy thickness equation. These equations allow for two N-factors to be calculated and used to estimate the growth rate in the database [13].

The K-V Transition Model

Kapsalis et al published a paper in 2016 proposing a new transition model. The model, dubbed the “K-V transition model”, is a linear stability theory model which utilizes the velocity shape factor Λ to determine the instability point. Like the e^N model, the various parameters of the laminar boundary layer are calculated along the surface. After this, the critical Reynolds number, $Re_{\delta 1,cr}$, can be calculated at each point based on the known distribution of Λ. $Re_{\delta 1}$ is the Reynolds number based on displacement and is defined by Eq. 1.2:

$$Re_{\delta 1} = \frac{U_b \delta_1}{\nu} \tag{1.2}$$

where U_b is the velocity at the edge of the boundary layer, δ_1 is the displacement, and ν is the air kinematic viscosity. The critical Reynolds number is the value which correlates to the instability/inflection point as Λ varies. Once $Re_{\delta 1,cr}$ is computed, it can be used to calculate $Re_{\theta t}$ along the airfoil. Each point is then assumed to be the transition point, and the value $DRe_{\theta t}$ is calculated. This value represents the difference in the Reynolds number based on momentum thickness at the transition point and the instability point. The transition point is then determined to be the point when $DRe_{\theta t}$ exceeds the critical value $Re_{\theta t,cr}$. In the work of Kapsalis, this method is shown to be more accurate than the two equation implementation of the e^N model. In addition, the K-V model only uses one parameter (Λ) and therefore is able to converge faster than the e^N model [10].

The Langtry and Menter Transition Model

In 2009, Langtry and Menter published a paper establishing a new correlation-based transition model. It has become one of the most widely used transition implementations in industry [6]. The model has also been adapted to create a hybrid method, where this model is used to calculate the amplification factor N from the e^N model [14].

This model utilizes the two equation Shear Stress Transport (SST) $k - \omega$ turbulence model in order to calculate the turbulence. The key concept behind this model is the use of the vorticity Reynolds number Re_v , which was derived by Van Driest and Blumer [15]. Langtry and Menter were able to establish an empirical correlation between the local boundary layer quantities and Re_v . They were therefore able to avoid the requirement of integrating the boundary-layer velocity profile. Instead, they calculate Re_θ with the simple equation:

$$Re_\theta = \frac{max(Re_v)}{2.193} \tag{1.3}$$

Re_v can be easily calculated at each mesh point, allowing this model to be efficient. Meanwhile, $Re_{\theta t,cr}$ can be calculated with experimental correlations and solving a transport equation. Another transport equation is then used to solve for the intermittency, using Re_v [16].

The model then uses a transport equation to solve for intermittency. The local intermittency values are used in conjunction with the $k - \omega$ turbulence model. The transition onset location is determined using equation 1.3. Using correlations based on the local transition momentum thickness Reynolds number, Langtry and Menter were able to determine the F_{length} function, which sets the length of the transition zone, and F_{onset}, which enables the transition from laminar to turbulent flow. Meanwhile, the intermittency production term is calculated using F_{length} and

$Re_{\theta t,cr}$. A second transport equation is used to solve for the transport variable for the momentum thickness Reynolds number, $\overline{Re_{\theta t}}$. A transport equation is used rather than a correlation based on experiment in order to account for the large variance of turbulence intensity in some applications. However, the local $Re_{\theta t}$ value is calculated using experimental correlations. These correlations take turbulence intensity into account and require an iterative process in order to compute the final value of $Re_{\theta t}$ [16].

The Medida Transition Model

The Medida model [6] is a derivation of the Langtry-Menter model. The model has been modified to be compatible with the one equation Spalart-Allmaras (S-A) turbulence model rather than the $k-\omega$ two-equation turbulence model. Another modification is the adjustment of the correlations between $Re_{\theta t}$ and the turbulence intensity. The model implements a linear piece-wise form of the correlations which better account for data from the T3-series zero-pressure gradient flat plate experiments and laminar flow simulations. The intermittency production and destruction terms have been adjusted in order to improve intermittency recovery in the turbulent boundary layer. The model assumes constant freestream turbulence intensity in the flow field and omits separation-induced transition. In addition, the destruction term is not scaled by intermittency when using the term in the S-A turbulence model [6].

1.3 Uncertainty Quantification

1.3.1 Definitions

In order to provide a comprehensive understanding of uncertainty quantification (UQ), it is necessary to review the definitions of certain terms and concepts:

Uncertainty: Uncertainty is defined as a potential deficiency that is due to a lack of knowledge. Uncertainty can be divided into two categories: aleatory uncertainty and epistemic uncertainty [18].

Aleatory uncertainty: Aleatory uncertainty is uncertainty associated with the inherent randomness/variation in a population. This type of uncertainty is also known as irreducible uncertainty, since this uncertainty cannot be eliminated from the model [19]. An example of aleatory uncertainty in CFD is the variation of an input parameter, such as free stream Mach number. This uncertainty usually has a probability distribution associated with it, such as a normal or uniform distribution.

Epistemic uncertainty: Epistemic uncertainty is uncertainty stemming from a model's failings due to a lack of knowledge. Research into the area where knowledge is lacking can result in an improved model, which can in turn reduce or even eliminate epistemic uncertainty [19]. One current source of epistemic uncertainty in CFD is turbulence model assumptions [18].

Sensitivity analysis: Sensitivity analysis (SA) is the study of how much an output varies due to a change in a certain input. SA can be categorized as either local or global. Local SA measures how much the output changes due to infinitesimal changes in the input. On the other hand, global SA measures how the output changes when the input is varied over all feasible values. [20]

Non-intrusive and intrusive techniques: *Non-intrusive* techniques are UQ techniques which do not require the modification of the deterministic function, model, and/or codes that are used. These techniques are relatively simple to implement since they simply require the selection of certain inputs into the model without any "tinkering under the hood" of the CFD solvers. On the other hand, *intrusive* methods modify the actual mathematical equations being solved by the CFD codes.

1.3.2 Overview

UQ falls under the framework of Verification and Validation [17]. Verification addresses errors that occur when solving equations and deals primarily with the numeric solvers and algorithms using numerical analysis. On the other hand, validation deals with how accurate the numerical simulations are when compared to the physical world and experimental data. When conducting experiments, *uncertainty bars* are provided along with the data to quantify the repeatability and measurement errors associated with the experiment. UQ can be used to calculate computational *uncertainty bars* that are analogous to the uncertainty bars from experiments as well as quantify the numerical errors attributed to the computational solver [18].

When applying UQ to CFD, it is useful to consider each CFD simulation as a function $y = g(\vec{x})$, where $\vec{x}$ is a vector of inputs to the CFD simulation, such as angle of attack, freestream Mach number, Reynolds number, and FSTI and y represents the quantities of interest (QOI), such as the coefficients of lift, drag, and moment. Uncertainties in $\vec{x}$ result in $\vec{x}$ becoming a stochastic variable. The uncertainty propagates through the system, resulting in y also becoming a stochastic variable. The actual UQ techniques depend on the type of uncertainty. Aleatory and epistemic uncertainties are each handled differently in UQ. The present work focuses on aleatory uncertainties attributed to variation in FSTI. For aleatory uncertainty, UQ can be used to determine the distribution of the output and/or statistics related to this distributions, such as the expected mean and standard deviation [20]. The following sections will review the different UQ techniques typically used to obtain these quantities.

1.3.3 Monte Carlo Method

The Monte Carlo method [21] is one of the oldest UQ techniques. It is a simple non-intrusive sampling method that utilizes the law of large numbers to converge to the correct solution. The law of large numbers states that as the frequency of a probabilistic event increases, the mean of the results will converge to the expected/theoretical mean. The Monte Carlo method involves randomly sampling the input parameters; the inputs can have a uniform distribution, a normal distribution, or any other distribution desired.

The randomly generated samples are then used as the inputs for the system and the desired output quantities are computed. This is done repeatedly until the average of the outputs converges. This converged mean output is the expected value. The simplicity of this method allows for easy implementation and universal application. However, the method is slow to converge and may require an excessive amount of samples to converge to the correct solution [18]. For CFD simulations that take some time to run, this may make the Monte Carlo method infeasible from a computational cost standpoint without the use of a surrogate surface (see section 1.3.5).

1.3.4 Stochastic Collocation

Stochastic collocation is the application of quadrature to integrate integrands composed of random variables. This can be used to determine the expectation of a random variable. The goal of stochastic collocation is to calculate the expected mean output values $\mathbf{E}[y]$ and the variance of the output values $Var[y]$ (using the notation introduced in section 1.3.2). One way to determine these quantities is to use the probability density function (PDF) f_y. If the PDF has been computed, $\mathbf{E}[y]$ and $Var[y]$ can be calculated as follows:

$$\mathbf{E}[y] = \int_{-\infty}^{\infty} z f_y(z) dz \tag{1.4}$$

$$Var[y] = \int_{-\infty}^{\infty} (z - \mathbf{E}[y])^2 f_y(z) dz = \mathbf{E}[y^2] - (\mathbf{E}[y])^2 \tag{1.5}$$

These integrals can be computed numerically through quadrature techniques.

Consider the case where there is a single uncertain parameter ξ. Stochastic collocation is achieved by expressing the integrals in Eq. 1.4 and 1.5 as weighted sums of the integrands evaluated at a number of locations on the ξ-axis. These locations are referred to as abscissas. The abscissas and weights are typically chosen by selecting a basis function which is easy to integrate, usually a polynomial. The accuracy of the stochastic collocation method increases as the number of abscissas increases [18].

Gaussian quadratures are often used as they are highly accurate. For Gaussian quadrature, equation 1.4 is rewritten in terms of a weighted sum:

$$\int_a^b y(\xi) f(\xi) d\xi = \sum_{k=1}^{n} w_k y(\xi_k) + R_n(y) \tag{1.6}$$

where ξ_k are the zeros of the chosen *orthogonal* polynomial for the quadrature, w_k are the weights, which are calculated using the weighting function f. n is the total number of abscissas used for the quadrature and R_n is the remainder term, which also denotes the order of accuracy of the method.

Like the Monte Carlo method, stochastic collocation is non-intrusive and relatively simple to implement. Once the abscissas have been determined, the CFD simulation is simply run using the abscissas as the inputs. Thus, stochastic collocation usually requires far fewer CFD runs to achieve convergence.

Gauss-Hermite Quadrature

The Gauss-Hermite quadrature is used to approximate integrals of the form [22]:

$$\int_{-\infty}^{\infty} e^{-\zeta^2}\phi(\zeta)d\zeta \approx \sum_{k=1}^{n} w_k\phi(\zeta_k) \tag{1.7}$$

where w_i and ζ_i are defined by the Hermite polynomial and M is the number of nodes used for the quadrature. The Hermite polynomial can be expressed recursively as follows [23]:

$$H_n(x) = n!\sum_{m=0}^{n/2}(-1)^m \frac{1}{m!2^m(n-2m)!}(2x)^{n-2m} \tag{1.8}$$

ζ_i are defined by the zeros of 1.8 and w_i is defined by [25]:

$$w_i = \frac{2^{n-1}n!\sqrt{\pi}}{n^2[H_{n-1}(\zeta_i)]^2} \tag{1.9}$$

If the uncertain parameter X is characterized with a normal distribution with a mean μ and standard deviation σ, the Gauss-Hermite quadrature can be used to compute $\mathbf{E}[y]$ and $Var[y]$ by applying a simple transformation $\zeta = (x - \mu)/(\sqrt{2}\sigma), \phi(\zeta) = g(\mu + \sqrt{2}\sigma\zeta)/\sqrt{\pi}$ ($g(x)$ is defined as the CFD simulation). Using this transformation and the abscissas and weights defined by the Hermite polynomial, $\mathbf{E}[y]$ and $Var[y]$ can be written as follows:

$$\mathbf{E}[y] = \int_{-\infty}^{\infty} \frac{1}{\sqrt{2\pi\sigma^2}} e^{-(x-\mu)^2/2\sigma^2} g(x)dx \approx \sum_{k=1}^{n} \frac{w_k}{\sqrt{\pi}} g(\mu + \sqrt{2}\sigma\zeta_k) \tag{1.10}$$

$$Var[y] \approx \sum_{k=1}^{n} \frac{w_k}{\sqrt{\pi}} (g(\zeta_k) - \mathbf{E}[y])^2 \tag{1.11}$$

1.3.5 Surrogate Surfaces

One of the main drawbacks of both the Monte Carlo method and stochastic collocation is the computational time required to compute the mean and variance of the QOIs. Stochastic collocation methods can require 5-10 CFD runs for a single case, while Monte Carlo sampling may require tens of thousands of runs to achieve convergence. This can make these methods cost-prohibitive unless combined with a surrogate surface. A surrogate surface approximates the relationship between the output QOIs of the CFD simulation and the uncertain input parameters [20]. Each QOI requires its own surrogate surface. Although several CFD simulations are necessary to create the surrogate surfaces, this method provides a way to perform Monte Carlo sampling and stochastic collocation inexpensively.

There are several methods that can be used to generate the surrogate surface. The simplest method is to run a parametric sweep through the uncertain variable and extrapolate between the points. More complex methods include using radial basis functions [26], support vector regression [27], polynomial chaos [28, 29], and Kriging [30–33].

1.4 Thesis Contributions

The purpose of this thesis is to examine the effects of introducing uncertainty into the input FSTI and investigate the sensitivity of the aerodynamic coefficients of lift, drag, and moment to this uncertainty. This was achieved by applying UQ techniques such as stochastic collocation and surrogate surfaces to determine the expected mean values of QOIs and the expected standard deviations for these QOIs. A comparative analysis was used in conjunction with the calculated standard deviations to determine the sensitivities of the QOIs to uncertainty in FSTI.

All CFD simulations in this study used the in-house flow solver OVERTURNS [34] with a $\gamma - Re_\theta -$SA transition model. Four airfoils were selected to be used in this study: 1) NACA 0012, 2) S809, 3) SC1095, and 4) RC(4)-10. These airfoils were selected due to their widespread usage in the field. For each airfoil, a parametric sweep of FSTI was conducted in order to generate the surrogate surface. Stochastic collocation was performed for a test case using both the surrogate surface and actual CFD runs in order to validate the surrogate surface. Once this was complete, stochastic collocation was applied to the surrogate surface to compute the expected means and standard deviations of the QOIs over a range of angles of attack. For the SC1095 and RC(4)-10, both of which often operate in transonic flows, the freestream Mach number was varied between 0.2 and 0.8 as well.

The contributions of the present work is to lay out the foundation and process for generating "uncertainty reference tables" for various airfoils. This data can be used to provide more accurate data when there is known uncertainty in the freestream conditions. These tables will also highlight operating conditions under which there is greater sensitivity to this uncertainty. Such information would be relevant for determining confidence in a CFD simulation, providing more accurate validation, and creating more robust designs.

1.5 Scope and Organization of Thesis

This thesis is concerned with the application of UQ techniques for airfoils undergoing transition with an uncertain FSTI value. This thesis details the motivation for this research, the UQ techniques used, the general approach, and the results of applying the UQ techniques to four airfoils. The rest of the thesis is organized as follows:

- Chapter 2 describes the computational methodology used for this study. The chapter reviews how the flow solver OVERTURNS solves the Reynolds Averaged Navier Stokes (RANS) equations. In addition, the discretizations methods, mesh descriptions, and boundary conditions used by the solver are described.
- Chapter 3 reviews the UQ methodology used by the present work. This includes descriptions of the parametric studies, the generation of the surrogate surfaces, and the details of the quadratures used for the stochastic collocation.

- Chapter 4 presents the results of the parametric studies and the generation of the surrogate surfaces for the NACA0012, S809, SC1095, and RC(4)-10. The FSTI is varied from 0.05% to 5% while the angle of attack is varied from -4 degrees to 12 degrees.

- Chapter 5 presents the results of the UQ analysis. These results include the expected mean values of the QOIs and the standard deviations for these QOIs. A comparison of these standard deviations over the range of angles of attack for specific mean FSTI values will be used to demonstrate the changes in sensitivity for the QOIs.

- Chapter 6 summarizes the key results presented in this study and provides recommendations for future work.

Chapter 2

Numerical Implementation

In this chapter, an overview of the CFD analysis used for this work is presented. The *Overset Transonic Unsteady Rotor Navier-Stokes* (OVERTURNS) flow solver [34] was used to run all simulations. This chapter will cover the partial differential equations (PDEs) which govern the flow and how OVERTURNS solves these PDEs to obtain the flow field solution. This includes the turbulence and transitioning modeling used by OVERTURNS to obtain the solution. The mesh generation process used for the present work is also discussed. Finally, sample results which validate the approach are presented.

2.1 Governing Equations

In order to determine flow characteristics, the governing equations, the Navier-Stokes equations, must be solved. The Navier-Stokes equations are coupled partial differential equations relating the velocity, density, pressure, and temperature. The equations are derived using conservation of mass, momentum, and energy and are dependent on both time t and the spatial coordinates x and y.

The equations can be written in "strong conservation form" in terms of the viscous and inviscid fluxes through the control volumes as follows:

$$\frac{\partial Q}{\partial t} + \frac{\partial F_i}{\partial x} + \frac{\partial G_i}{\partial y} = \frac{\partial F_v}{\partial x} + \frac{\partial G_v}{\partial y} \tag{2.1}$$

where Q is the conserved variables vector, F_i and G_i are the inviscid flux vectors, and F_v and G_v are the viscous flux vectors. Q is defined by Eq. 2.2:

$$Q = \left\{ \begin{array}{c} \rho \\ \rho u \\ \rho v \\ E \end{array} \right\} \tag{2.2}$$

where ρ is the fluid density, u and v are the components of the fluid velocity in the x and y directions. E is the total energy per unit volume and is calculated as follows:

$$E = \rho \left[e + \frac{1}{2}(u^2 + v^2) \right] \tag{2.3}$$

where e is the energy per unit mass.

The inviscid fluxes are defined by Eqs. 2.4 and 2.5, and the viscous fluxes are defined by Eqs. 2.6 and 2.7

$$F_i = \left\{ \begin{array}{c} \rho u \\ \rho u u + p \\ \rho u v \\ (E + p)u \end{array} \right\} \tag{2.4}$$

$$G_i = \left\{ \begin{array}{c} \rho v \\ \rho v u \\ \rho v v + p \\ (E + p)v \end{array} \right\} \tag{2.5}$$

$$F_v = \left\{ \begin{array}{c} 0 \\ \tau_{xx} \\ \tau_{yx} \\ u\tau_{xx} + v\tau_{yx} - q_x \end{array} \right\} \tag{2.6}$$

$$G_v = \left\{ \begin{array}{c} 0 \\ \tau_{xy} \\ \tau_{yy} \\ u\tau_{xy} + v\tau_{yy} - q_y \end{array} \right\} \tag{2.7}$$

In the above equations, q_x and q_y are the heat conduction terms. They are defined as:

$$q_j = k\frac{\partial T}{\partial x_j} \quad (j = x, y) \tag{2.8}$$

where k is the coefficient of thermal conductivity and T is the temperature of the fluid. τ_{ij} is the viscous stress tensor and is defined by Stokes' hypothesis [45]:

$$\tau_{ij} = \mu\left[\left(\frac{\partial u_i}{\partial x_j} + \frac{\partial u_j}{\partial x_i}\right) - \frac{2}{3}\frac{\partial u_k}{\partial x_k}\delta_{ij}\right], \quad \delta_{ij} = 1 \text{ if i=j; } \delta_{ij} = 0 \text{ if i} \neq \text{j} \tag{2.9}$$

μ is the coefficient of molecular viscosity and is given by Eq. 2.10:

$$\mu = C_1\frac{T^{\frac{3}{2}}}{T + C_2} \tag{2.10}$$

For air at standard temperature and pressure (STP), $C_1 = 1.4 \times 10^{-6}$ kg/(ms$\sqrt{K}$) and $C_2 = 110.4$ K. In order to solve this system, one more equation is needed:

$$p = \rho R T \tag{2.11}$$

Eq. 2.11 is the *equation of state* for ideal gases. R is the gas constant. The fluid in the present work is air at STP; it can therefore be assumed to be a calorically perfect gas, where the specific heats remain constant:

$$c_v = \frac{R}{\gamma - 1}; \quad c_p = \frac{\gamma R}{\gamma - 1} \tag{2.12}$$

where γ is the ratio of specific heats. For air at STP, $\gamma = 1.4$. In addition, the following equations are applicable to calorically perfect gases:

$$e = c_v T \tag{2.13}$$

$$p = (\gamma - 1)\rho e \tag{2.14}$$

$$e = c_v T \tag{2.15}$$

Using the above relations, Eq. 2.3 can be re-written as follows:

$$E = \frac{p}{\gamma - 1} + \frac{1}{2}\rho(u^2 + v^2) \tag{2.16}$$

2.2 Non-Dimensionalization

OVERTURNS solves the governing equations in their non-dimensionalized form. Non-dimensionalization results in all the flow variables to be of the same magnitude, thereby reducing numerical errors due to mathematical operations between numbers of very different values. In addition, non-dimensionalization allows for the parameter like Reynolds number and Mach number to be varied independently. Non-dimensionalized reference variables are denoted by the * superscript and are defined below:

$$x^* = \frac{x}{L}, \quad y^* = \frac{y}{L}, \quad t^* = \frac{t}{L/a_\infty} \tag{2.17}$$

$$u^* = \frac{u}{a_\infty}, \quad v^* = \frac{v}{a_\infty}, \quad \mu^* = \frac{\mu}{a_\infty} \tag{2.18}$$

$$\rho^* = \frac{\rho}{\rho_\infty}, \quad p^* = \frac{p}{p_\infty a_\infty^2}, \quad T^* = \frac{T}{T_\infty} \tag{2.19}$$

In the above equations, L represents the chord length of the airfoil and a_∞ is the freestream speed of sound. The governing equations in terms of the non-dimensionalized variables are obtained by substituting Eqs. 2.17 - 2.19 into Eq. 2.1. The dimensional governing equations are the same as the dimensionless ones, with the exception of the viscous stress tensor and thermal conduction terms. The modified terms are defined here:

$$\tau_{ij} = \frac{\mu M_\infty}{Re_\infty}\left[\frac{\partial u_i}{\partial x_j} + \frac{\partial u_j}{\partial x_i} - \frac{2}{3}\frac{\partial u_k}{\partial x_k}\delta_{ij}\right] \tag{2.20}$$

$$q_j = -\frac{\mu M_\infty}{Re_\infty Pr(\gamma - 1)}\frac{\partial T}{\partial x_j} \tag{2.21}$$

In the above equations, all the variables are non-dimensional, so the * superscript has been dropped for the sake of convenience. The above equations introduces three new dimensionless quantities:

$$\text{Reynolds number:} \quad Re_\infty = \frac{\rho_\infty V_\infty L}{\mu_\infty} \tag{2.22}$$

$$\text{Mach number:} \quad M_\infty = \frac{V_\infty}{a_\infty} \tag{2.23}$$

$$\text{Prandtl number:} \quad Pr = \frac{\mu c_p}{k} \tag{2.24}$$

where V_∞ is the freestream velocity magnitude ($\sqrt{u_\infty^2 + v_\infty^2}$). For air at STP, the Prandtl number, $Pr = 0.72$.

2.3 Reynolds-Averaged Navier-Stokes Equations

In order to model boundary layer transition, it is necessary to modify the governing equations into a form which is compatible with turbulence models. This can be achieved using the Reynolds-Averaged Navier Stokes (RANS) approach. Using this approach, the dependent variables are broken down into two components: the mean component and the fluctuating component, as shown in Eq. 2.25:

$$u = \overline{u} + u' \quad v = \overline{v} + v' \quad \rho = \overline{\rho} + \rho' \quad p = \overline{p} + p' \quad T = \overline{T} + T \tag{2.25}$$

The governing equations in terms of these components are then time-averaged. Eq. 2.26 is used to time average each quantity:

$$\overline{f} = \frac{1}{\Delta t} \int_{t_0}^{t_0 + \Delta t} f dt \tag{2.26}$$

where $\overline{f}$ is the time-averaged quantity and Δt is the time period. This time period must be small sufficiently small such that the mean flow variation is small, yet large when compared to the period of turbulent fluctuations. By definition, the mean of the fluctuating component (f') is equal to zero:

$$\overline{f'} = \frac{1}{\Delta t} \int_{t_0}^{t_0 + \Delta t} f' dt = 0 \tag{2.27}$$

The RANS equations are obtained by substituting Eq. 2.25 into the unsteady Navier-Stokes equations (Eq. 2.1). The RANS governing equations are identical to the Navier-Stokes equation with the addition of fluctuating terms. These terms can be grouped into a stress tensor, known as the Reynolds Stress Tensor (τ_{ij}):

$$(\tau_{ij})_{turb} = -\rho\overline{u_i'u_j'} \tag{2.28}$$

In order to solve the RANS equations, the Reynolds Stress tensor must be put in terms of the mean quantities. There are various turbulence models which are used to do so. The present work utilizes the Spalart-Allmaras turbulence model [35], which is discussed in detail in Sec. 2.6.3.

2.4 Coordinate Transformation

Eq. 2.1 is the Cartesian form of the Navier-Stokes equations. However, in order to apply these equations to the computational meshes used by OVERTURNS, it becomes necessary to apply a curvilinear coordinate transformation. This transformation maps the Cartersian coordinates x and y which may not be uniformly spaced, onto the computational domain (ξ and η) for an equally-spaced computational mesh (see Fig. 2.1). By applying chain rule differentiation to Eq. 2.1, one obtains the following:

$$\frac{\partial\tilde{Q}}{\partial t} + \frac{\partial\tilde{F}}{\partial\xi} + \frac{\partial\tilde{G}}{\partial\eta} = 0 \tag{2.29}$$

where,

$$
\begin{aligned}
\tilde{Q} &= \frac{1}{J}Q \\
\tilde{F} &= \frac{1}{J}[\xi_t Q + \xi_x(F_i - F_v) + \xi_y(G_i - G_v)] \\
\tilde{G} &= \frac{1}{J}[\eta_t Q + \eta_x(F_i - F_v) + \eta_y(G_i - G_v)] \\
\tilde{H} &= \frac{1}{J}[\zeta_t Q + \zeta_x(F_i - F_v) + \zeta_y(G_i - G_v)]
\end{aligned}
\tag{2.30}
$$

and J is the coordinate transformation Jacobian (i.e. the determinant of the 3×3 matrix $\dfrac{\partial(\xi,\eta)}{\partial(x,y)}$.

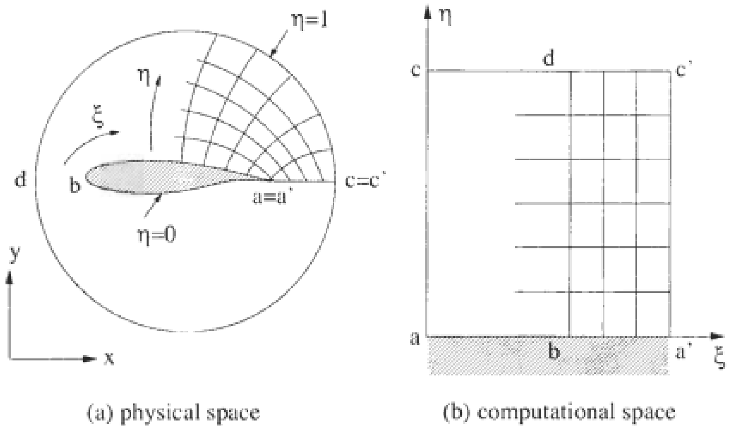

(a) physical space (b) computational space

Figure 2.1: Transformation from physical domain to computational domain (reproduced from Blazek 2006)

2.5 Grid Generation

The present work studies airflow over two-dimensional airfoils. It was therefore necessary to generate body-fitted meshes for these airfoils. The meshes used in this work were C-topology structured meshes, as pictured in Fig. 2.2. These meshes were created using hyperbolic grid generation. The mesh is made up of three types of boundaries: solid wall, farfield, and wake-cut.

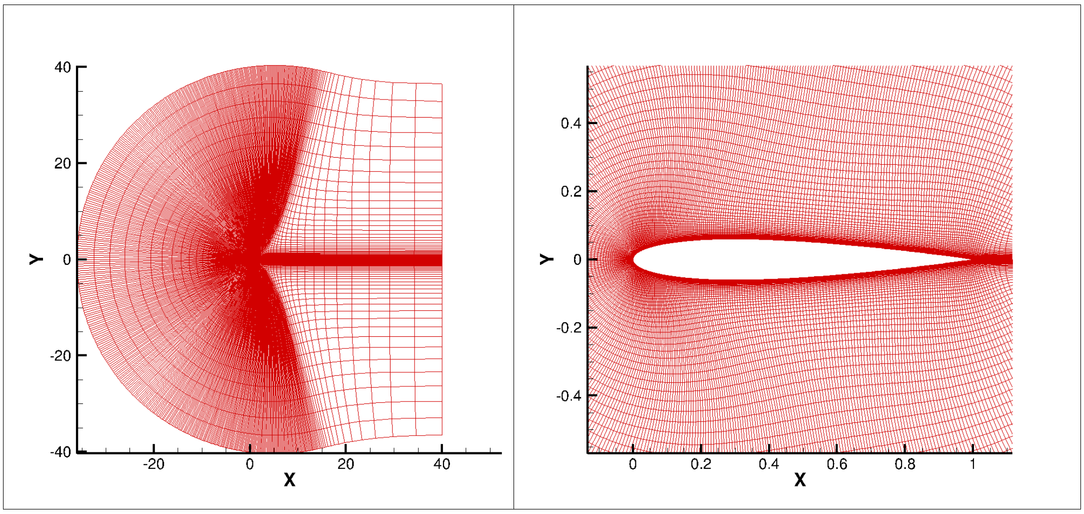

(a) C-mesh (b) Close-up of C-mesh

Figure 2.2: C-topology mesh around NACA 0012

2.6 Numerical Algorithms in OVERTURNS

This section describes the numerical algorithms used to discretize the governing equations, model turbulence and transition, and handle boundary conditions. OVERTURNS solves the curvilinear form of the RANS equations using a cell-averaged finite volume approach with a cell-vertex scheme. The flow variables are stored at each grid point, and the control volumes are computational cells which are centered around the grid points, as shown in Fig. 2.3. In order to determine the time rate of change in the conserved quantities at each timestep, the inviscid and viscous fluxes are calculated at the interfaces of the cell and integrated over the cell faces. Eq. 2.29 can therefore be converted into a semi-discrete form:

$$\frac{\partial \tilde{Q}}{\partial t} = -\frac{\tilde{F}_{j+\frac{1}{2}} - \tilde{F}_{j-\frac{1}{2}}}{\Delta \xi} - \frac{\tilde{G}_{k+\frac{1}{2}} - \tilde{G}_{k-\frac{1}{2}}}{\Delta \eta} \tag{2.31}$$

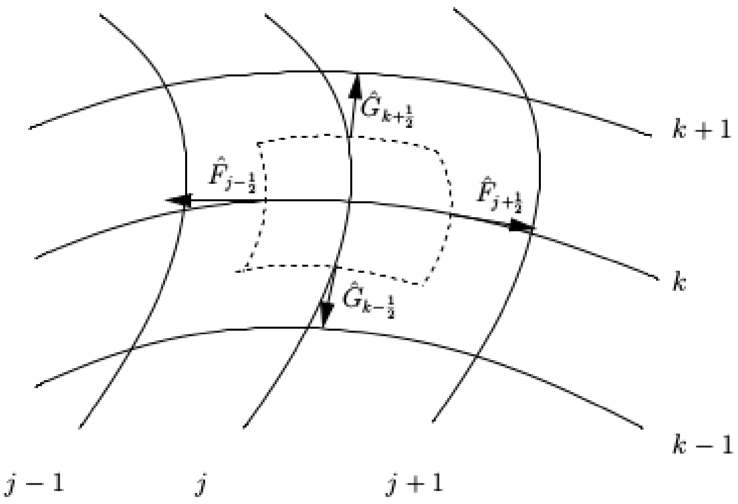

Figure 2.3: Computational Cell(reproduced from [36])

where j and k are the indices corresponding to the ξ and η directions respectively. The computational cell boundaries are therefore defined by $(j \pm \frac{1}{2}, k \pm \frac{1}{2})$. Note that this is the two-dimensional form of the equation. The next two sections describe the discretization techniques used to compute the inviscid and viscous fluxes.

2.6.1 Inviscid Fluxes

Evaluating the inviscid fluxes (Eqs. 2.4 and 2.5) in OVERTURNS is a two-step process. First, the primitive variables must be reconstructed at the cell faces. Once this has been achieved, the fluxes can be evaluated at the cell faces using the reconstructed primitive variables. All CFD solutions in this work were obtained using a Monotone Upstream-Centered Scheme for Conservation Laws (MUSCL) [37] to reconstruct the primitive variables for both the right and left sides of each face $(q^L_{i+\frac{1}{2}}, q^R_{i-\frac{1}{2}})$. MUSCL calculates the primitive variables at each face using the following equations:

$$q^L_{i+\frac{1}{2}} = \overline{q} + \phi_i \left[\frac{1}{3}(\overline{q}_{i+1} - \overline{q}_i) + \frac{1}{6}(\overline{q}_i - \overline{q}_{i-1})\right] \tag{2.32}$$

$$q^R_{i-\frac{1}{2}} = \overline{q} - \phi_i \left[\frac{1}{3}(\overline{q}_{i+1} - \overline{q}_i) + \frac{1}{6}(\overline{q}_i - \overline{q}_{i-1})\right] \tag{2.33}$$

where ϕ us Koren's differentiable limiter [38]:

$$\phi_i = \frac{3\Delta\overline{q}_i \nabla\overline{q}_i + \epsilon}{2(\Delta\overline{q}_i - \nabla\overline{q}_i)^2 + 3\Delta\overline{q}_i\nabla\overline{q}_i + \epsilon} \tag{2.34}$$

In the above equation, ϵ represents a small value used to avoid division by zero. Δ and ∇ are forward and backward operators: $\Delta\overline{q}_i = (\overline{q}_{i+1} - \overline{q}_i)$ and $\nabla\overline{q}_i = (\overline{q}_i - \overline{q}_{i-1})$.

Once the primitive variables are reconstructed, they are used to evaluate the inviscid fluxes using Roe's flux difference splitting scheme [39] with an entropy fix:

$$F(q^L, q^R) = \frac{F(q^L) + F(q^R)}{2} - |\tilde{A}(q^L, q^R)|\frac{q^R - q^L}{2} \tag{2.35}$$

In the above equation, F_L and F_R are the left and right state fluxes, and $\tilde{A}$ is the Roe-averaged Jacobian matrix. Numerical dissipation is taken into account by the second term on the right hand side of the above equation. In order to prevent entropy violations, Harten's entropy correction to the flux Jacobian eigenvalues is applied [40]:

$$|\lambda| = \begin{cases} |\lambda|, & \text{if } |\lambda| > \delta \\ \dfrac{\lambda^2 + \delta^2}{2\delta}, & \text{if } |\lambda| \leq \delta \end{cases} \tag{2.36}$$

where $\delta = \max\Big[0, (\overline{\lambda}_{i+\frac{1}{2}} - \lambda_i), (\overline{\lambda}_{i+1} - \lambda_{i+\frac{1}{2}})\Big]$. $\overline{\lambda}$ denotes Roe-averaged eigenvalues.

2.6.2 Viscous Fluxes

In order to evaluate the viscous fluxes (Eqs. 2.6 and 2.7), in the curvilinear form of the governing equations, the following must be evaluated:

$$\frac{\partial}{\partial \xi}\left(\alpha \frac{\partial \beta}{\partial \eta}\right) \tag{2.37}$$

OVERTURNS evaluates the above expression with a second order central differencing scheme:

$$\frac{1}{\Delta \xi}\left(\left[\alpha_{j+\frac{1}{2},k} \frac{\beta_{j+\frac{1}{2},k+1}-\beta_{j+\frac{1}{2},k}}{\Delta \eta}\right]-\left[\alpha_{j-\frac{1}{2},k} \frac{\beta_{j-\frac{1}{2},k}-\beta_{j-\frac{1}{2},k-1}}{\Delta \eta}\right]\right) \tag{2.38}$$

where $\delta_{j+\frac{1}{2},k} = \dfrac{\delta_{j,k}+\delta_{j+1,k}}{2}$ and $\delta = (\alpha, \beta)$.

2.6.3 Turbulence Modeling

OVERTURNS is able to incorporate turbulence into the CFD solutions by solving the RANS governing equations using turbulence models (see Sec. 2.3). The present work uses the one-equation Spalart-Allmaras turbulence model [35]. The model is based on the Boussinesq eddy viscosity hypothesis [41, 42], which proposes the following relationship between the Reynolds stress tensor and the mean strain rate:

$$(\overline{\tau}_{ij})_{turb} = -\overline{\rho}\overline{u_i' u_j'} = \frac{2}{3}\overline{\rho} k \delta_{ij} - \mu_t \left[\left(\frac{\partial \overline{u}_i}{\partial x_j} + \frac{\partial \overline{u}_j}{\partial x_i}\right) - \frac{2}{3}\frac{\partial \overline{u}_k}{\partial x_k}\delta_{ij}\right] \tag{2.39}$$

where μ_t is the turbulent/eddy viscosity and k is the turbulent kinetic energy:

$$k = \frac{1}{2}\left[\overline{(u')^2} + \overline{(v')^2} + \overline{(w')^2}\right] \tag{2.40}$$

Using Eq. 2.39, the total viscous stress tensor to be used in the RANS equations can be calculated:

$$(\overline{\tau}_{ij})_{total} = \frac{2}{3}\overline{\rho}k\delta_{ij} - (\mu + \mu_t)\left[\left(\frac{\partial \overline{u}_i}{\partial x_j} + \frac{\partial \overline{u}_j}{\partial x_i}\right) - \frac{2}{3}\frac{\partial \overline{u}_k}{\partial x_k}\delta_{ij}\right] \tag{2.41}$$

The Spalart-Allmaras model uses a transport equation for the eddy viscosity, evaluating the diffusion, production, and destruction terms for eddy viscosity:

$$\frac{D\tilde{\nu}}{Dt} = P_\nu - D_\nu + \frac{1}{\sigma}\left[\nabla((\nu + \tilde{\nu}) + c_{b2}(\nabla\tilde{\nu})^2\right] \tag{2.42}$$

$$P_\nu = c_{b1}\tilde{\Omega}\tilde{\nu} \text{ and } D_\nu = c_{w1}f_w[\frac{\tilde{\nu}}{d}]^2 \tag{2.43}$$

Ω is the vorticity magnitude. $\tilde{\Omega}$ is given by:

$$\tilde{\Omega} = \max\left(\Omega + \frac{\tilde{\nu}}{\kappa^2 d^2}f_{v2}, 0.3\Omega\right), f_{v2} = 1 - \frac{\chi}{1 + \chi f_{v1}} \tag{2.44}$$

The wall damping function, f_w, is given by:

$$f_w = g\left[\frac{1 + c_{w3}^6}{g^6 + c_{w3}^6}\right]^{\frac{1}{6}}, g = r + c_{w2}(r^6 - r), r = \frac{\tilde{\nu}}{\tilde{\Omega}\kappa^2 d^2} \tag{2.45}$$

The constants in the above equations are defined as follows: $c_{b1} = 0.1355, \sigma = 2/3, c_{b2} = 0.622, \kappa = 0.41, c_{w1} = c_{b1}/\kappa^2 + (1 + c_{b2})/\sigma, c_{w2} = 0.3, c_{w3} = 2.0, c_{v1} = 7.1.$

The eddy viscosity transport variable, $\tilde{\nu}$ is set equal to zero at smooth wall boundaries, equal to 0.1 at the inflow boundaries, and extrapolated from the interior at the outflow boundaries.

For the present work, convection terms were discretized using a first order upwind scheme, while diffusion terms were discretized using a second order central scheme. The algebraic system of equations was solved using the Diagonalized Alternating Direction Implicit (DADI) approximate factorization method [43].

2.6.4 Transition Modeling

The present work utilizes the $\gamma - Re_\theta$−SA transition model, as developed by Medida [6]. The transition model solves two transport equations in order to generate an intermittency and transition momentum thickness flow field around the airfoil. The model is coupled with the Spalart-Allmaras one equation turbulence model (see Sec. 2.6.3) by multiplying the eddy viscosity production term from the SA model with the intermittency factor, γ. Therefore, the effects of turbulence only appear as the intermittency factor approaches one.

The transition model defines the intermittency factor transport equation as follows:

$$\frac{D(\rho\gamma)}{Dt} = P_\gamma - D_\gamma + \frac{\partial}{\partial x_j}\left[(\mu + \mu_t)\frac{\partial \gamma}{\partial x_j}\right] \tag{2.46}$$

The source term is given by:

$$P_\gamma = \rho\, F_{\text{onset}}\, G_{\text{onset}}\, \max\left[\frac{\Omega}{F_{\text{length}}}, \frac{1.0}{F_{\text{length, min}}}\right] \tag{2.47}$$

$$\text{If } \gamma > 1.0,\ P_\gamma = (1.0-\gamma)P_\gamma \tag{2.48}$$

$$F_{\text{length}} = 40.0, F_{\text{length, min}} = 2.5 \tag{2.49}$$

The destruction term is given by:

$$D_\gamma = \rho\ \Omega\ \gamma(1.0 - G_{\text{onset}}) \tag{2.50}$$

$$F_{\text{onset}} = \max(F_{\text{onset2}} - F_{\text{onset3}}, 0) \tag{2.51}$$

$$F_{\text{onset1}} = \frac{Re_v}{2.193 Re_{\theta c}} \tag{2.52}$$

$$F_{\text{onset2}} = \min(\max(F_{\text{onset1}}, F_{\text{onset1}}^4), 4.0) \tag{2.53}$$

$$F_{\text{onset3}} = \max(2 - (0.25 R_T)^3, 0) \tag{2.54}$$

$$Re_v = \frac{\rho d^2 S}{\mu}, R_T = \frac{\mu_t}{\mu} \tag{2.55}$$

The critical Reynolds number can be calculated using the following numerical correlation:

$$Re_{\theta c} = 0.62\overline{Re_{\theta t}} \tag{2.56}$$

The transport equation for the transition momentum thickness Reynolds number, $\overline{Re_{\theta t}}$ is given by:

$$\frac{D(\rho\overline{Re_{\theta t}})}{Dt} = P_{\theta t} + \frac{\partial}{\partial x_j}\left[2.0(\mu+\mu_t)\frac{\partial\overline{Re_{\theta t}}}{\partial x_j}\right] \tag{2.57}$$

FSTI%	$Re_{\theta t,new}$
0.01	1800.0
0.03	1135.0
0.51	894.0
1.33	392.0
2.00	252.0
5.25	165.0
6.5	100.0

Table 2.1: Piecewise Linear Correlations between $Re_{\theta t}$ and FSTI

The production term is given by:

$$P_{\theta t} = 0.03\frac{\rho}{t}(Re_{\theta t} - \overline{Re_{\theta t}})(1.0 - F_{\theta t}) \tag{2.58}$$

$$F_{\theta t} = \min\left(e^{-\left(\frac{d}{\delta}\right)^4}, 1.0\right) \tag{2.59}$$

$$\theta_{BL} = \frac{\overline{Re_{\theta t}}\mu}{\rho U}; \quad \delta_{BL} = 7.5\theta_{BL}; \quad \delta = \frac{50\Omega d}{U}\delta_{BL} \tag{2.60}$$

Piecewise linear correlations, as defined by Table 2.1, are multiplied by the F(λ_θ) equations to calculate $Re_{\theta t}$ values outside of the boundary layer. This takes the FSTI and streamwise pressure gradient effects. The F(λ_θ) equations are given below:

$$F(\lambda_\theta) = \begin{cases} 1 - [-12.986\lambda_\theta - 123.66\lambda_\theta^2 - 405.689\lambda_\theta^3]e^{-\left[\frac{Tu}{1.5}\right]^{1.5}}, & \lambda_\theta \leq 0 \\ 1 + 0.275[1 - e^{[-35.0\lambda_\theta]}]e^{-\left[\frac{Tu}{0.5}\right]}, & \lambda_\theta > 0 \end{cases} \tag{2.61}$$

where the pressure gradient parameter, λ_θ, is defined by:

$$\lambda_\theta = \frac{\rho\theta^2}{\mu}\frac{dU}{ds} \tag{2.62}$$

$\frac{dU}{ds}$ is the streamwise acceleration:

$$\frac{dU}{ds} = \frac{u}{U}\frac{dU}{dx} + \frac{v}{U}\frac{dU}{dy} \tag{2.63}$$

$$\frac{dU}{dx} = \frac{1}{2U}\left[2u\frac{du}{dx} + 2v\frac{dv}{dx}\right] \tag{2.64}$$

$$\frac{dU}{dy} = \frac{1}{2U}\left[2u\frac{du}{dy} + 2v\frac{dv}{dy}\right] \tag{2.65}$$

$$U = \sqrt{u^2 + v^2} \tag{2.66}$$

In order to evaluate F(λ_θ), an iterative process is used with the initial value of $\lambda_\theta = 0.0$. The freestream $\overline{Re_{\theta t}}$ value is set equal to $Re_{\theta t\,\mathrm{inf}}$. $Re_{\theta t\,\mathrm{inf}}$ can be computed using the above equations with λ_θ equal to zero.

The intermittency transport equation is solved for the intermittency factor γ, which can then be multiplied by production term of the eddy viscosity in the SA model. Eq. 2.42 therefore is rewritten to include the intermittency term:

$$\frac{D\tilde{\nu}}{Dt} = \gamma P_\nu - D_\nu + \frac{1}{\sigma}\left[\nabla((\nu + \tilde{\nu}) + c_{b2}(\nabla\tilde{\nu})^2\right] \tag{2.67}$$

Transition Model Validation

In order to verify the transition model's accuracy in OVERTURNS, a test case was run using the S809 airfoil. The case was run with an FSTI of 0.05%, an angle of attack of 1 degree, and a Reynolds number of 2 million. The case was compared against both experimental results as well as the results obtained by

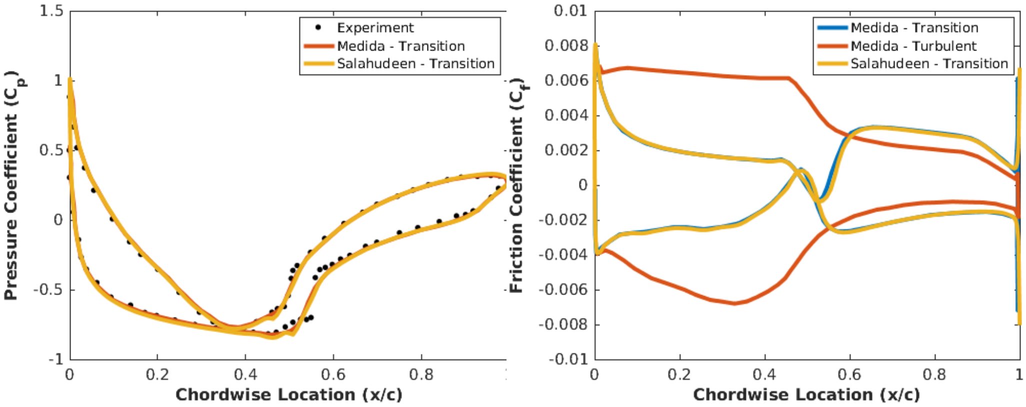

(a) Coefficient of Pressure (b) Coefficient of Skin Friction

Figure 2.4: Transition Model Validation for S809 Airfoil

Medida [6]. Fig. 2.4 shows the coefficient of pressure and skin friction. As can be seen from the figure, there is good agreement between the results of the present work, the results from Medida's work, and experimental results.

2.6.5 Time Integration

Although the present work only deals with steady cases, for the sake of completeness, a short overview of time integration is provided here. OVERTURNS utilizes BDF2 [44], a second order implicit backwards-in-time method as its time-marching scheme to integrate the semi-discrete form of the governing equations (Eq. 2.31). Backwards-in-time implicit methods converge well and are usually more stable, making these methods a logical choice when dealing with boundary layer flows. The BDF2 scheme is implemented using Eq. 2.68:

$$\frac{\partial \tilde{Q}^{n+1}}{\partial t} = -\frac{\tilde{F}^{n+1}_{j+\frac{1}{2}} - \tilde{F}^{n+1}_{j-\frac{1}{2}}}{\Delta\xi} - \frac{\tilde{G}^{n+1}_{k+\frac{1}{2}} - \tilde{G}^{n+1}_{k-\frac{1}{2}}}{\Delta\eta} + \tilde{S}^{n+1}_{j,k} \qquad (2.68)$$

where the LHS can be discretized using Eq. 2.69 :

$$\frac{\partial \tilde{Q}^{n+1}}{\partial t} = \frac{3\tilde{Q}^{n+1} - 4\tilde{Q}^{n} + \tilde{Q}^{n-1}}{2\Delta t} \tag{2.69}$$

Eq. 2.68 is a non-linear equation; a Taylor series expansion about $\tilde{Q}^n$ can be applied to the fluxes to linearize the equation:

$$\tilde{F}^{n+1} = \tilde{F}^{n} + \tilde{A}\Delta\tilde{Q} + O(\Delta t^2) \tag{2.70}$$

$$\tilde{G}^{n+1} = \tilde{G}^{n} + \tilde{B}\Delta\tilde{Q} + O(\Delta t^2) \tag{2.71}$$

where the solution update $\Delta\tilde{Q} = \tilde{Q}^{n+1} - \tilde{Q}^{n}$, and A and B are the flux Jacobians, defined as $\frac{\partial \tilde{F}}{\partial \tilde{Q}}$ and $\frac{\partial \tilde{G}}{\partial \tilde{Q}}$ respectively. The source term S can also be in linearized using the same method. The linearization does not decrease the time-accuracy of the scheme since the linearized terms are second-order accurate. The linearizations are then applied to Eq. 2.68, resulting in the following equation:

$$[I + \Delta t(\delta_\xi \tilde{A}^n + \delta_\eta \tilde{B}^n)]\Delta\tilde{Q} = -\Delta t[\delta_\xi \tilde{F}^n + \delta_\eta \tilde{G}^n] \tag{2.72}$$

In the above equation, the left-hand side controls the convergence and stability of the equation, while the right-hand side represents the physics of the problem.

Eq. 2.72 can be written as a banded matrix of algebraic equations. OVERTURNS solves this system using an approximate factorization method. In order to invert the system, the Lower-Upper Symmetric Gauss-Seidel (LUSGS) method is utilized. Using this method, Eq. 2.72 can be rewritten as:

$$[L+D+U]\Delta\tilde{Q}^n \approx [D+L]D^{-1}[D+U]\Delta\tilde{Q}^n = -\Delta t[RHS]^n \tag{2.73}$$

In the above equation, L, U, and D represent the lower, upper, and main diagonal of the left-hand side of the equations, respectively and are defined as follows:

$$L = \Delta t(-\tilde{A}^+_{j-1,k} - \tilde{B}^+_{j,k-1}) \tag{2.74}$$

$$U = \Delta t(\tilde{A}^-_{j+1,k} + \tilde{B}^-_{j,k+1}) \tag{2.75}$$

$$D = I + \Delta t(\tilde{A}^+_{j,k} - \tilde{A}^-_{j,k} + \tilde{B}^+_{j,k} - \tilde{B}^-_{j,k}) \tag{2.76}$$

A two step process is used to obtain the solution update $\Delta\tilde{Q}$:

$$[D+L]\Delta\overline{\overline{Q}} = -\Delta t[RHS]^n \tag{2.77}$$

$$[D+U]\Delta\tilde{Q} = D\overline{\overline{Q}} \tag{2.78}$$

Chapter 3

Uncertainty Quantification Methodology

This chapter details the uncertainty quantification methodology used in the present work. The following steps were taken for each airfoil studied:

1. **Run Parametric Sweep:** Parametric studies were run varying FSTI and the angle of attack. For some airfoils, Reynolds number or Mach number was also varied. Details of the specific parameters being varied are provided in Table 3.1.

2. **Generate Surrogate Surface:** Once the parametric studies were run, a piecewise cubic Hermite interpolating polynomial (PCHIP) was used to interpolate between the points in the parametric sweeps and generate the surrogate surface.

Airfoil	**Mach Number**	**Reynolds Number** ($\times 10^6$)
S809	0.2	2.0
NACA 0012	0.2	0.5, 1.0, 2.0, 4.0
SC1095	0.2, 0.4, 0.6, 0.7, 0.8	2.0
RC(4)-10	0.2, 0.4, 0.6, 0.7, 0.8	2.0

Table 3.1: Freestream Conditions for Parametric Sweeps

3. **Perform UQ Analysis - Monte Carlo Simulation:** The Monte Carlo method was used in conjunction with the surrogate surface in order to compute the expected means and standard deviations of the aerodynamic coefficients, given an input FSTI and standard deviation. These computations were repeated over a range of angles of attack. For some of the airfoils, the Mach or Reynolds number was also varied. The standard deviations of the aerodynamic coefficients indicate the sensitivity of each parameter to uncertainty in the FSTI. By computing the standard deviations for different freestream conditions, it is possible to see how the freestream parameters affect this sensitivity.

3.1 Parametric Sweeps

Based off of preliminary sweeps, the FSTI range of 0.05% to 5% was identified as the area of interest for this study. An initial increment of 0.5% was used for the first sweep. Three angles of attack were initially chosen: 0 degrees, 4 degrees, and 8 degrees. Each case was then run in OVERTURNS until convergence. The results of this initial sweep are shown in Fig. 3.1 for the S809 airfoil. This initial sweep showed that the QOIs experienced rapid change between 0.5% and 2%

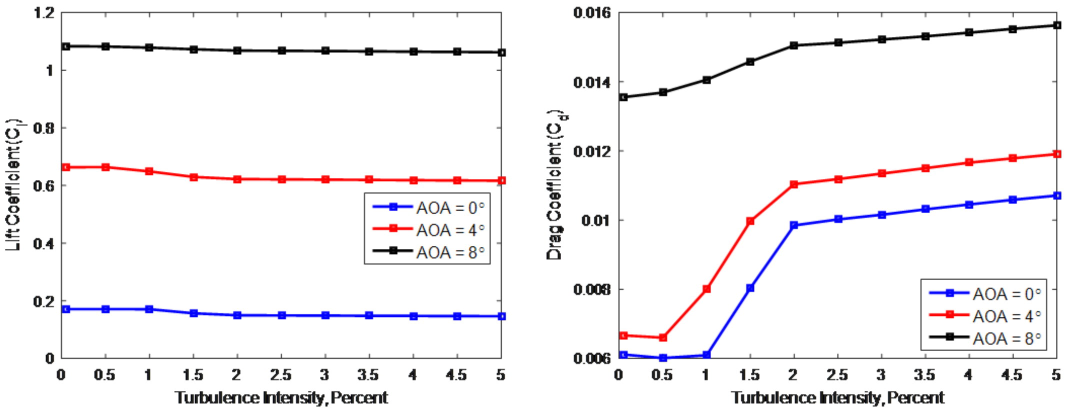

(a) Lift coefficient (b) Drag coefficient

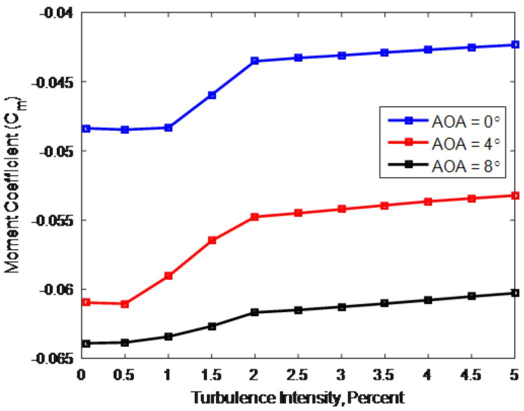

(c) Moment coefficient

Figure 3.1: Initial Turbulence Sweep for S809 Airfoil at Mach = 0.2, Re = 2×10^6

FSTI. Additional points were therefore added to the sweep in this region until the parametric sweep was well resolved. In addition, the angle of attack range was expanded, from -4 degrees to 12 degrees, using 1 degree increments. The final parametric sweep is shown in Fig. 3.2 for the S809 airfoil.

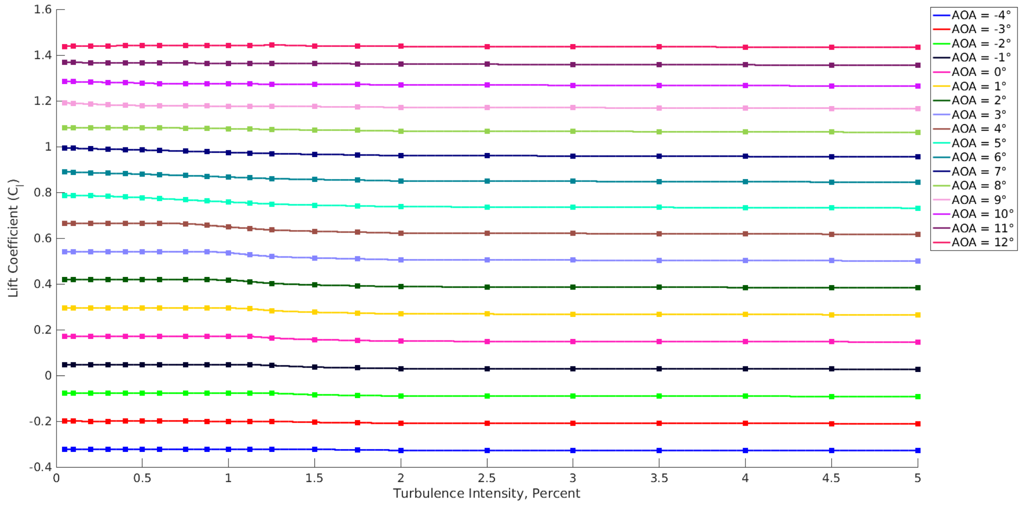

(a) Lift coefficient

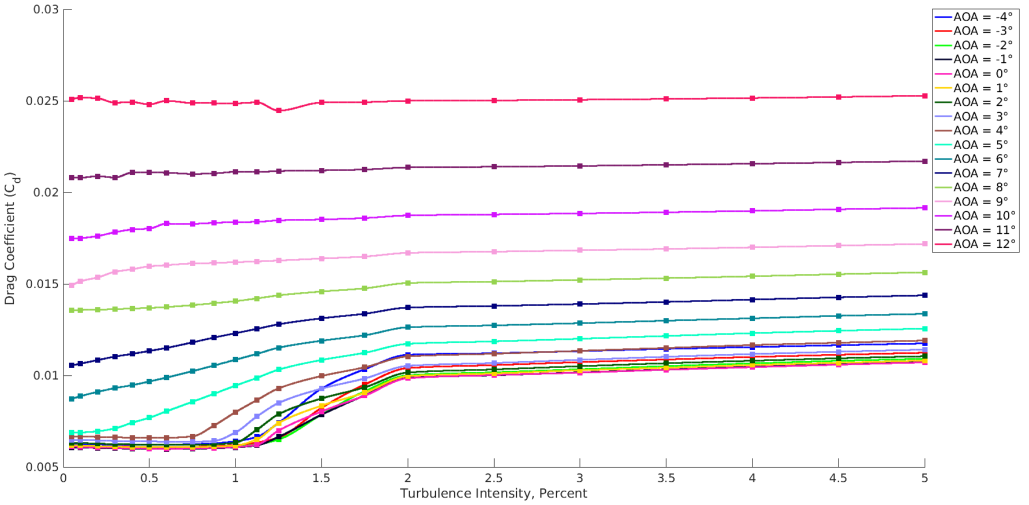

(b) Drag coefficient

Figure 3.2: Final Parametric Sweep for S809 Airfoil at Mach = 0.2, Re = 2×10^6

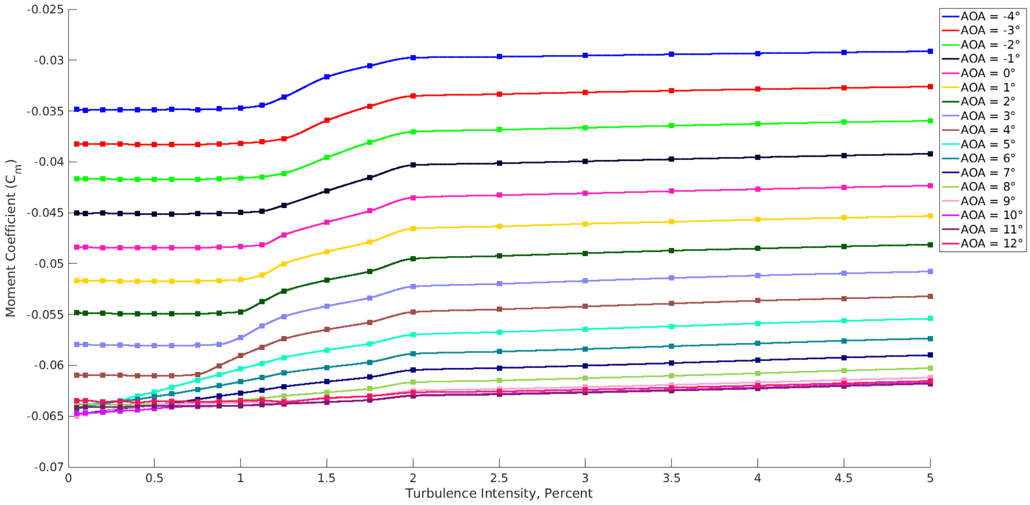

(c) Moment coefficient

Figure 3.2: Final Parametric Sweep for S809 Airfoil at Mach = 0.2, Re = 2×10^6 (cont.)

3.2 Surrogate Surface Generation

Once the parametric turbulence sweep was complete, a surrogate surface was generated using the “PCHIP” function in MATLAB [46]. PCHIP stands for Piecewise Cubic Hermite Interpolating Polynomial. This function uses a Hermite polynomial $P(x)$ to interpolate points from a given data set, resulting in a monotonic cubic interpolation. The polynomial generated has a continuous first derivative $\frac{dP}{dx}$. The PCHIP function selects the slopes at each data point such that the interpolating polynomial preserves the shape of the data and respects monotonicity. Therefore the extrema of the data are also the extrema of $P(x)$.

In this work, the PCHIP function was invoked using the range of 0% to 5.0%

FSTI, with intervals of 0.001% as the input interpolation points for the PCHIP function. The CFD results from the parametric sweep were used as the data to be interpolated. The solid lines in Fig. 3.2 represent the generated surrogate surface. It can be seen that PCHIP smoothly fills in the data between the CFD outputs.

3.3 UQ Analysis

Once the surrogate surface has been generated, the next step is to compute the expected means and standard deviations. This can be achieved through either a Monte Carlo approach or stochastic collocation. The Monte Carlo method was deemed better suited for the current work since the use of the surrogate surface allowed for a large number of runs to be conducted without a large computational penalty. While stochastic collocation would have been more efficient, it was not possible to use more than 5 nodes for quadrature with the desired mean input FSTI (1%) and standard deviation (0.3333%). Increasing the number of nodes with these inputs would have required CFD simulations to be run with negative FSTI values, which was not possible (see Table 3.2). Therefore, a Monte Carlo approach was taken. As shown by Fig. 3.3, using the Monte Carlo approach results in the means and standard deviations to converge to the correct values. Since the stochastic collocation method is limited to 5 nodes, it is not as accurate. Note that the present work assumes that the uncertainty in FSTI results in a normal distribution of freestream FSTI values.

Node	5 Nodes - FSTI (percent)	6 Nodes - FSTI (percent)
1	$4.777 * 10^{-2}$	-0.1080
2	0.548	0.3703
3	1.0	0.7945
4	1.452	1.2055
5	1.952	1.6297
6	-	2.1080

Table 3.2: FSTI values for the quadrature for mean FSTI = 1%, $\sigma = 0.3333$

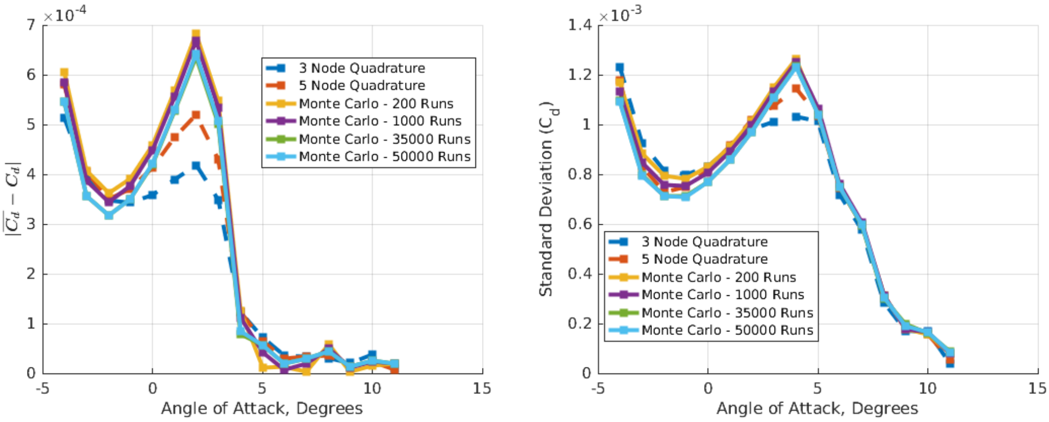

Figure 3.3: UQ Analysis for Drag - S809 Airfoil, Mach = 0.2, Re = 2×10^6, Mean FSTI = 1.0%, Std Dev = 0.3333%

Airfoil	**No. of Inputs**
S809	800,000
NACA 0012	350,000
SC1095	550,000
RC(4)-10	650,000

Table 3.3: Number of FSTI Input Values Required for Consistency

3.3.1 Monte Carlo Method

This section details how the Monte Carlo method was applied to determine the expected mean and standard deviations for the aerodynamic coefficients. First a vector of normally distributed FSTI input values was generated using the MATLAB normal random number generation function 'normrnd'. The number of input values was experimentally determined such that the results were consistent. This number differed per airfoil; the number of input values are listed in Table 3.3. Once this vector of inputs was generated, the aerodynamic coefficients were calculated at these input values using the surrogate surface. The results were then averaged and the standard deviation was calculated.

3.4 Validation

In order to be confident of the results of the process detailed above, it was necessary to validate the method. This process included validating the surrogate surface and verifying that the results were reasonable when compared to discrete FSTI.

3.4.1 Surrogate Surface Validation

In order to avoid the high costs of thousands of CFD simulations, surrogate surfaces were used in place of actual CFD results. The surrogate surfaces were generated using actual CFD results from parametric sweeps, as detailed in Sec. 3.1 - 3.2. In order to verify that the surrogate surfaces could be relied upon to provide accurate results, both stochastic collocation and Monte Carlo simulations were performed using both the surrogate surface. This was compared against stochastic collocation using actual CFD simulations for a test case for the S809 airfoil. Note that the Monte Carlo method was not used with actual CFD results due to its excessively high computational cost. A five node Gauss-Hermite quadrature was performed using a mean FSTI value of 1% and a standard deviation of 0.3333. The 5 node quadrature therefore required 5 CFD simulations at the FSTI values specified in Table 3.2. The results of the 5 CFD simulations are compared to the results generated from the surrogate surface in Fig. 3.4. The figure shows that the surrogate surface agrees well with the actual CFD results.

Once the aerodynamic coefficients were obtained from the surrogate surface results, the expected mean and standard deviations could be calculated for the test case (AOA = 8 degrees, mean FSTI = 1%, $\sigma = 0.3333$). The results of this quadrature are presented in Table 3.4 using the actual CFD results and the surrogate surface. The table shows that the final output of stochastic collocation using the surrogate surface is comparable to the results of stochastic collocation using actual CFD results. A Monte Carlo simulation using 10,000 runs was also performed using the surrogate surface. The results of this Monte Carlo simulation

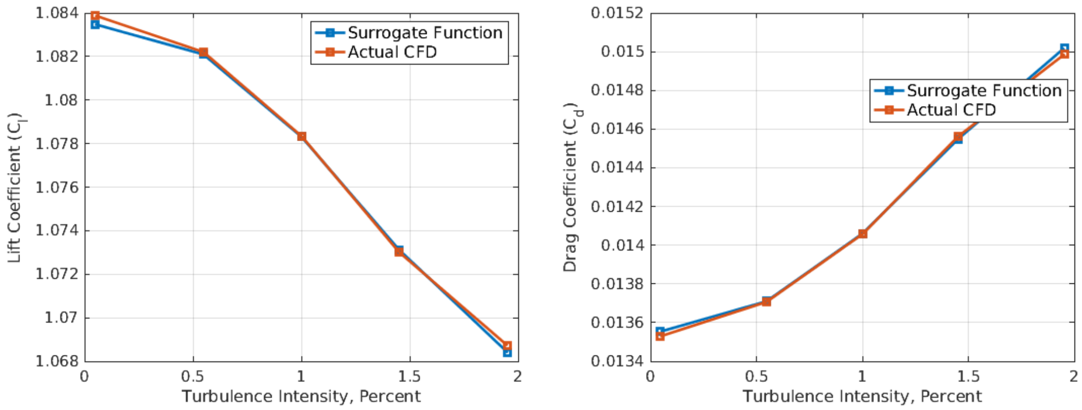

(a) Lift coefficient (b) Drag coefficient

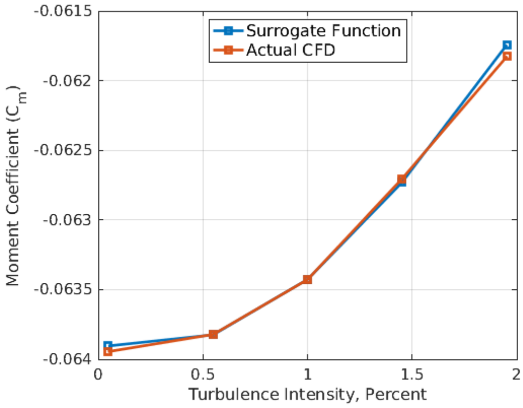

(c) Moment coefficient

Figure 3.4: Comparison of Surrogate Results and CFD Results for S809 Airfoil at Mach = 0.2, Re = 2×10^6, AOA = 8 degrees

	Stochastic Collocation - CFD - 5 Nodes		**Stochastic Collocation - Surrogate - 5 Nodes**		**Monte Carlo - Surrogate - 10,000 Runs**	
Coefficient	Expected Value	Standard Deviation	Expected Value	Standard Deviation	Expected Value	Standard Deviation
Lift	1.077963	0.003297	1.077950	0.003234	1.077877	0.003214
Drag	0.0140970	3.082e-04	0.0140959	3.035e-04	0.0141036	3.005e-04
Moment	-0.0633449	4.180e-04	-0.0633469	4.138e-04	-0.0633367	4.073e-04

Table 3.4: Comparison of Expected QOIs and Standard Deviations for for S809 Airfoil at Mach = 0.2, Re = 2×10^6, AOA = 8 degrees

are also included in Table 3.4. The table shows that the results are all in general agreement. Thus it was deemed that Monte Carlo with a surrogate surface could be used for the uncertainty quantification of FSTI on airfoil aerodynamics.

Chapter 4

Parametric Sweep Results

While the main purpose of the parametric sweeps was to generate the surrogate surfaces for the UQ analysis, many cases of interest were identified and investigated. This chapter presents selected results which featured behavior worth noting and exploring. Note that the complete parametric sweep results can be found in Appendix A. Four airfoils were used: 1) S809, 2) NACA 0012, 3) SC1095, and 4) RC(4)-10. FSTI was varied from 0.05% to 5%. However, this section focuses on the results up to 3% FSTI. The angle of attack was varied from -4° to 12° for the S809, SC1095, and RC(4)-10 airfoil, with the exception of certain cases where the convergence of the CFD cases became problematic due to the high angles of attack, as discussed later. For the NACA 0012, the angle of attack was varied from 0° to 12°. The negative angles of attack were omitted since the NACA 0012 is a symmetric airfoil. Mach number was also varied for the SC1095 and RC(4)-10 airfoils. In order to explore the effect of varying Reynolds number, four Reynolds

Airfoil	**Mach Number**	**Reynolds Number** ($\times 10^6$)
S809	0.2	2.0
NACA 0012	0.2	0.5, 1.0, 2.0, 4.0
SC1095	0.2, 0.4, 0.6, 0.7, 0.8	2.0
RC(4)-10	0.2, 0.4, 0.6, 0.7, 0.8	2.0

Table 4.1: Freestream Conditions for Parametric Sweeps

numbers were used for the NACA 0012. Table 3.1 provides the freestream Mach numbers and Reynolds numbers for each parametric sweep.

4.1 Computational Meshes

All the meshes used for this study are two-dimensional with C-topology grids. 491 points are used in the wrap-around direction on the airfoil surface, while 131 points are used in the wall-normal direction. These dimensions were chosen to ensure sufficient discretization for result accuracy while minimizing the computational time required to run CFD simulations. The outer boundary was placed 40 chord lengths away from the airfoil to ensure that the outer domain did not interfere with the CFD solution. The meshes for each airfoil are presented in Fig. 4.1.

4.2 S809 Airfoil

The S809 airfoil is a thick airfoil (maximum thickness of 21% of chord) used specifically in horizontal axis wind turbines. The NREL Phase VI model wind

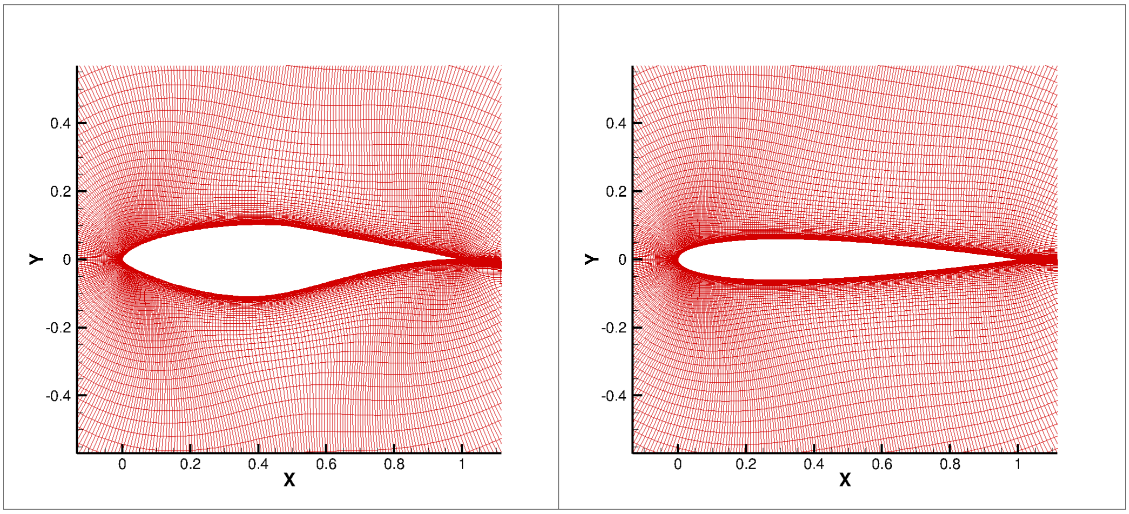

(a) S809

(b) NACA 0012

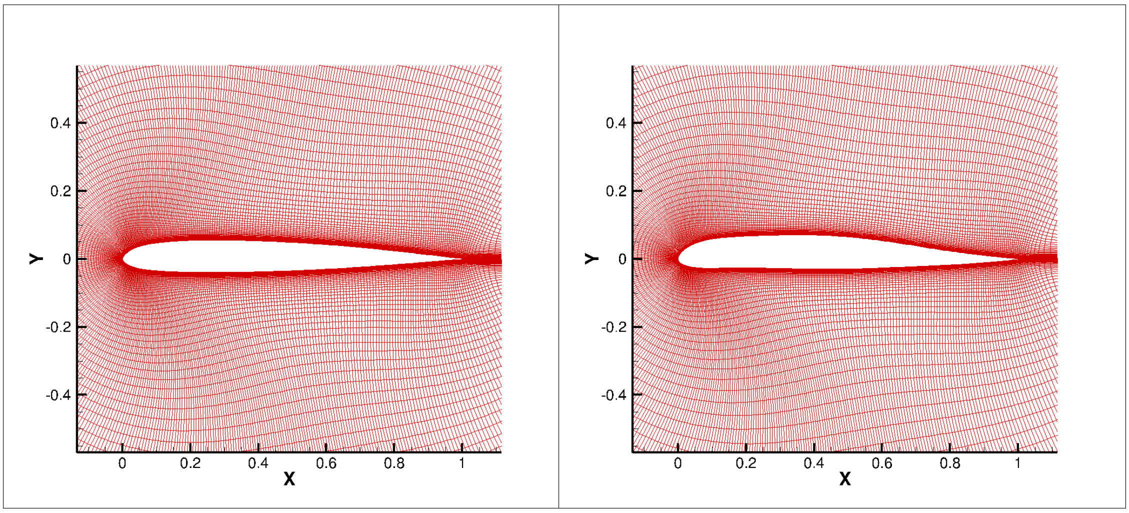

(c) SC1095

(d) RC(4)-10

Figure 4.1: Computational Meshes for Airfoil Parameter Sweeps

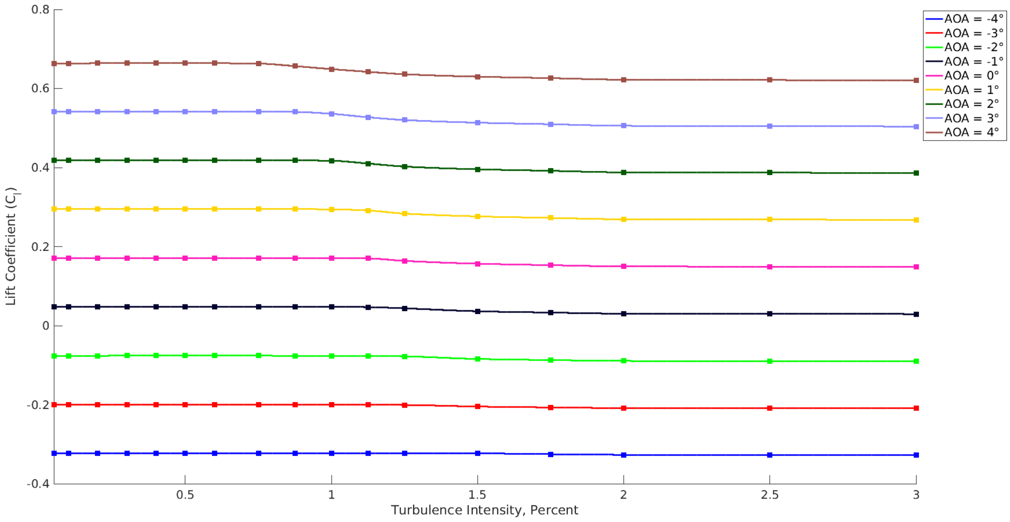

(a) Lift coefficient

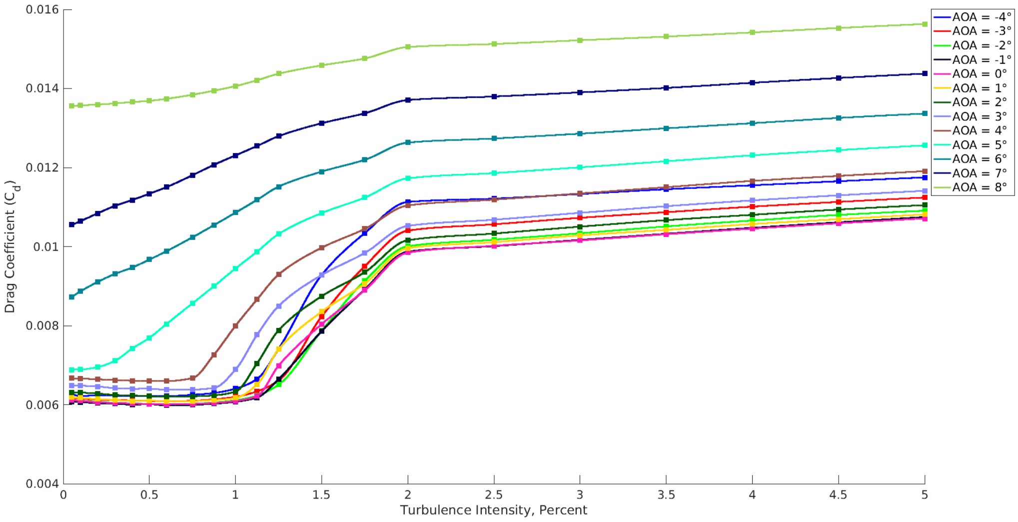

(b) Drag coefficient

Figure 4.2: Parametric Sweep for S809 Airfoil at Mach = 0.2, Re = 2×10^6

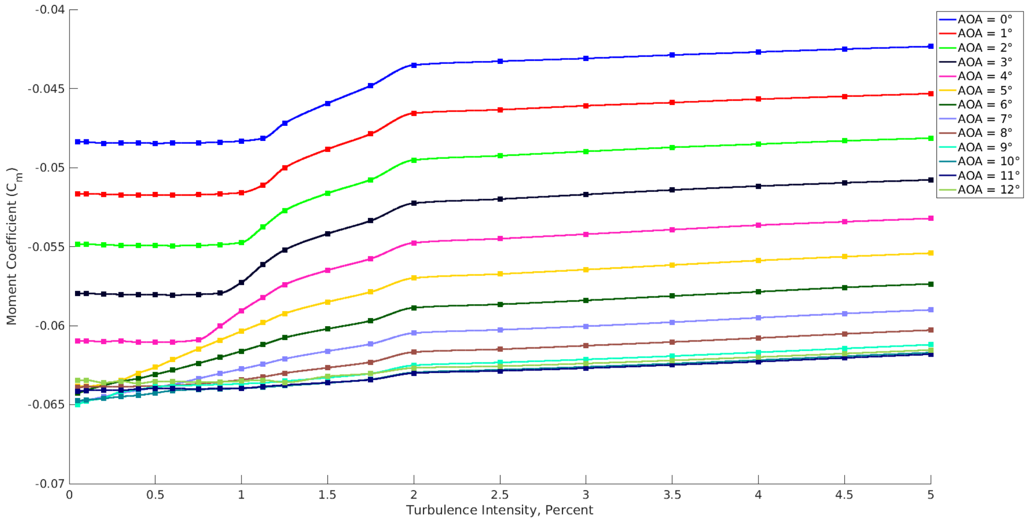

(c) Moment coefficient

Figure 4.2: Parametric Sweep for S809 Airfoil at Mach = 0.2, Re = 2×10^6 (cont.)

turbine primarily uses this airfoil for its turbine blades [47]. The airfoil is designed to promote laminar flow over the airfoil for over 50% of the airfoil at low angles of attack. This design makes the S809 airfoil popular for transition studies. The parameter sweep for the S809 airfoil was run at a freestream Mach number of 0.2 and a Reynolds number of 2 million.

Fig. 4.2 presents the parametric sweep for the S809 airfoil. Observe that lift remains relatively constant as FSTI is varied, although there is a slight decrease in lift as FSTI increases for the high AOA. Drag increases as FSTI increases for all AOA, with the maximum amount of change occurring near 0° AOA. The pitch moment also increases as FSTI increases for all AOA.

Fig. 4.3a depicts the coefficient of drag versus the angle of attack for various

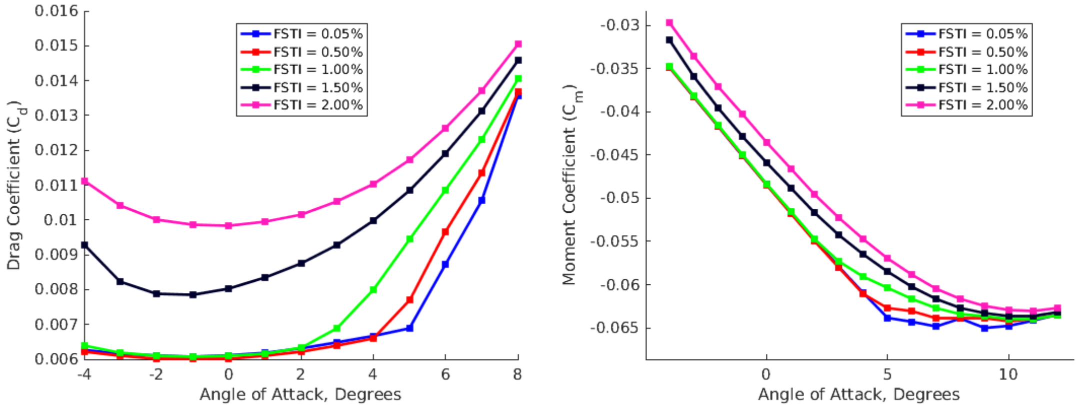

(a) Coefficient of Drag

(b) Coefficient of Moment

Figure 4.3: S809 Airfoil at Mach = 0.2, Re = 2.0×10^6 - Aerodynamic Coefficients vs. AOA

FSTI values up to 2%. The graph allows one to clearly visualize the “drag bucket.” This drag bucket phenomenon is caused by the transition from laminar to turbulent flow. When the flow is laminar, the drag does not change substantially, even as angle of attack increases, creating the bottom of the bucket. When the flow transitions to turbulent flow, the drag increases sharply and continues to increase as angle of attack increases, creating the sides of the bucket. One can note that for low FSTI values (0.05% - 1.0%), the laminar portion of the graph is much larger. At higher FSTI values (1.5% and 2%), the laminar region is much shorter and steeper. One can also note that at low angles of attack, there is a significant difference between the values of drag between FSTI values of 1% and 2%. However, as AOA increases, the curves for all the FSTI values approach the same drag coefficient value. A similar trend can be seen for the coefficient of moment, as illustrated in Fig. 4.3b, where the 0.05%, 0.5%, and 1.0% FSTI curves fall on top of each other at the plotted moderate AOA.

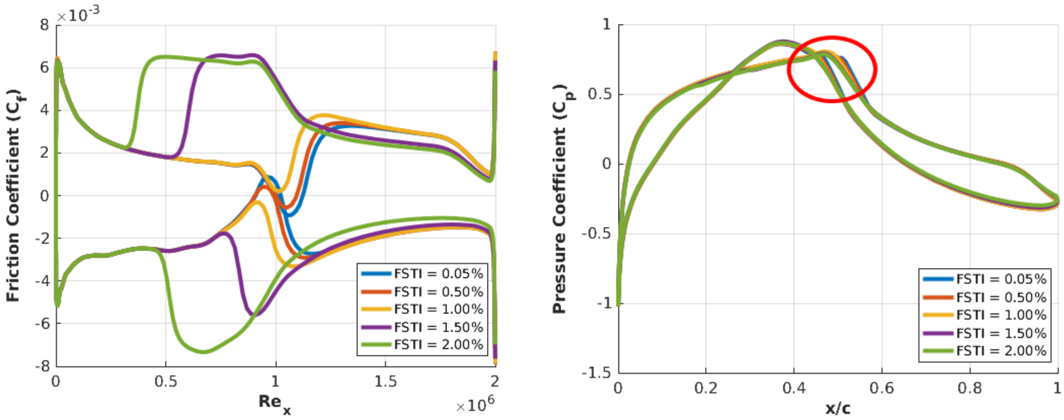

(a) Skin Friction - AOA = 0°   (b) Pressure - AOA = 0°

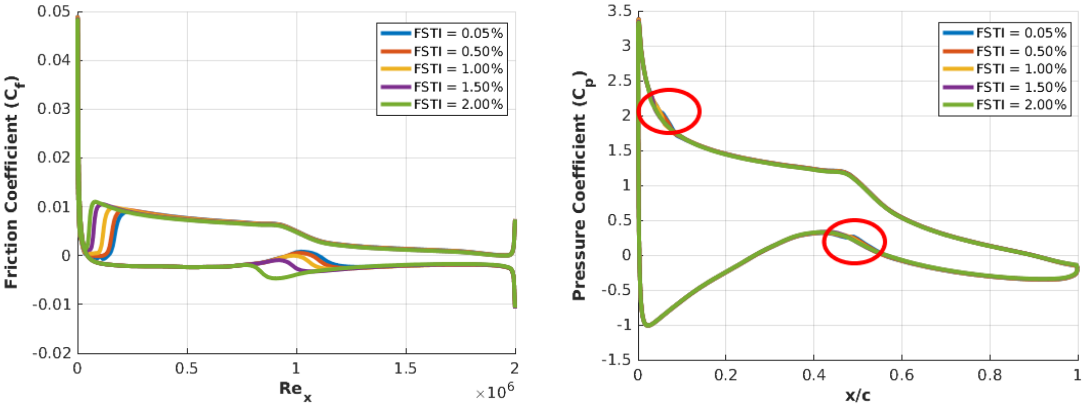

(c) Skin Friction - AOA = 8°   (d) Pressure - AOA = 8°

Figure 4.4: S809 Airfoil at Mach = 0.2, Re = 2.0×10^6 - Skin Friction and Pressure Plots - Separation Bubble

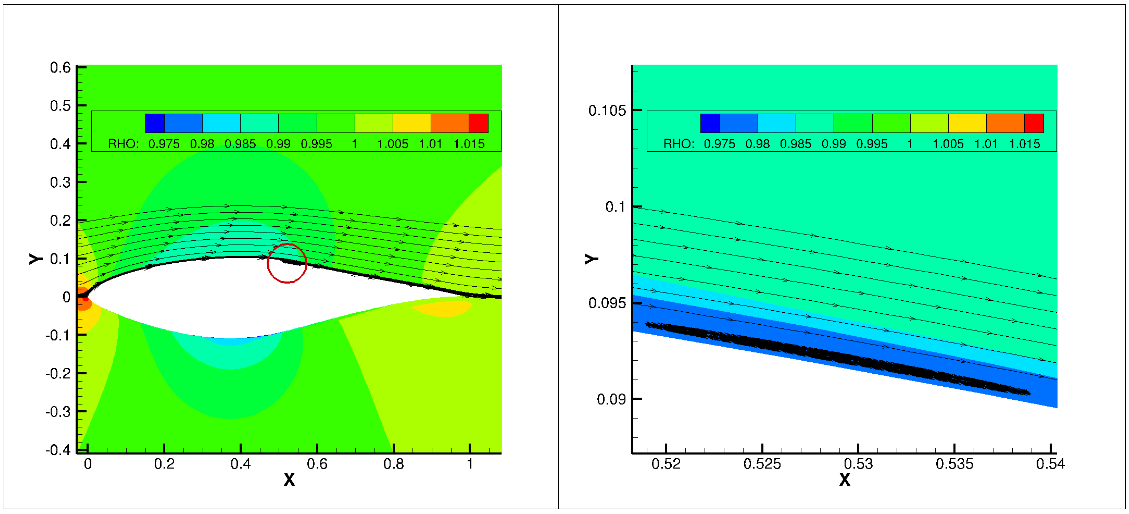

Figure 4.5: Separation Bubble for S809 Airfoil for AOA = 0°, FSTI = 1.0%, Mach = 0.2, Re = 2.0×10^6

Fig. 4.4 shows the coefficients of pressure and skin friction along the airfoil for an angle of attack of 0° and 8° AOA. Note that the curve at the top portion of the graph represents the upper surface of the airfoil, while the curve at the bottom of the graph represents the lower surface. Also note the sign convention for skin friction plots: airflow moving from left-to-right over the airfoil results in positive skin friction on the upper surface and negative skin friction on the lower surface. The transition from laminar to turbulent flow can be determined from the skin friction coefficient plots. The steep increase in the magnitude of the skin friction coefficient indicates the transition location. As can be seen from the plots, as the FSTI value increases, the transition location moves toward the leading edge of the airfoil.

In addition, the skin friction plots can be used to determine the type of transition. Observe the skin friction coefficient plot for AOA of 0°. For the lower values of FSTI (0.05% and 0.5%), it can be seen that the friction becomes negative on the upper surface right before transition. The opposite occurs on the bottom surface. This indicates that the air flow has reversed direction in this region. This indicates a separation bubble has formed, and the air is circulating in this bubble, as pictured in Fig. 4.5. The laminar separation bubble results in separation-induced transition (see sec. 1.2.6). Once the flow transitions, the turbulent boundary layer then reattaches to the airfoil.

The separation bubbles can also be seen on the pressure plots, albeit more subtly. There is a small pressure drop at the bubble, since suction pressure decreases due to the adverse pressure gradient. Since the location of the bubble varies slightly for each FSTI case, the pressure plot varies slightly at the location of the separation bubble. The separation bubbles have been circled on the figure. One can notice that the transition location does not move as much between 0.05% and 1.0%, when compared to the change in transition location between 1.5% and 2.0%. On the other hand, at 0° AOA for 1.5% and 2.0% FSTI, there is no negative skin friction for the upper surface and no positive skin friction for the lower surface. Rather, the skin friction just increases steeply. This indicates natural transition has occurred. The flow remains attached in this case as well.

At 8° AOA, all five cases undergo separation-induced transition, with a very small separation bubble near the leading edge at the top of the airfoil. At the bottom surface, another separation bubble is present near mid-chord, except for the 2.0% FSTI case, which undergoes natural transition here. Again, there is only a small change in transition location as FSTI varies. The lack of change in the transition location at 8° AOA explains why, in Fig. 4.3a, there is only a small difference in drag at the high angles of attack, but greater difference at lower angles of attack. At low angles of attack, the type of transition changes from separation-induced to natural transition. At high angles of attack, separation-induced transition occurs predominantly.

It can be noted that there is a significant difference between the 0° and 8° AOA plots. The transition location moves from mid-chord to the leading edge of the airfoil and a much larger pressure gradient is present for the 8° AOA case on the upper surface. On the lower surface, the transition location only moves slightly aft from 0° to 8° AOA because of the separation induced transition near midchord at lower FSTI.

4.3 NACA 0012 Airfoil

The NACA 0012 airfoil is a symmetrical airfoil with a maximum thickness of 12% of the chord. This airfoil was used for helicopter rotors for a number of years. The large amount of experimental data available for the NACA 0012 makes it an ideal "yardstick" to compare other airfoils against. In this study, the NACA 0012 airfoil was used for the Reynolds number sweep using a constant Mach number of 0.2. The results of the parametric studies for the four Reynolds numbers selected are presented in Figs. 4.6 - 4.17.

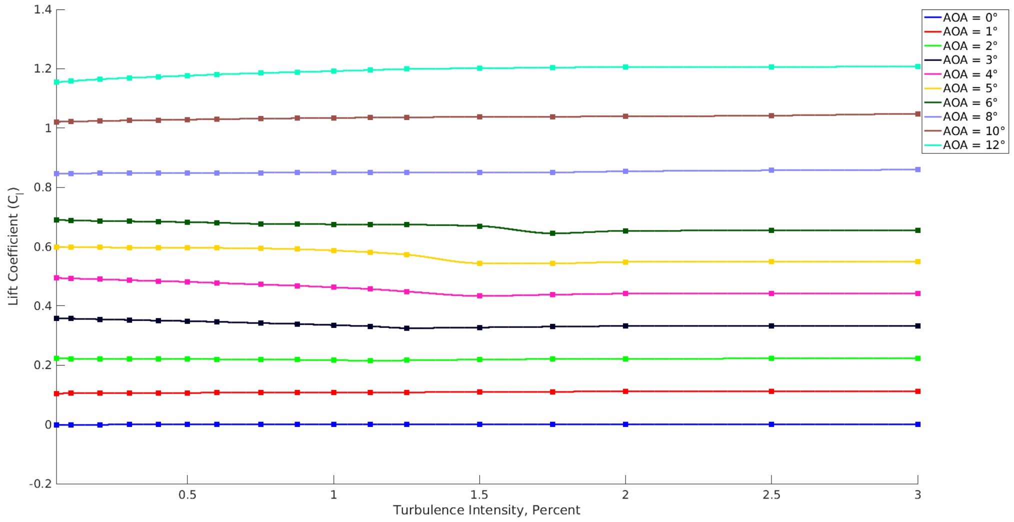

(a) Lift coefficient

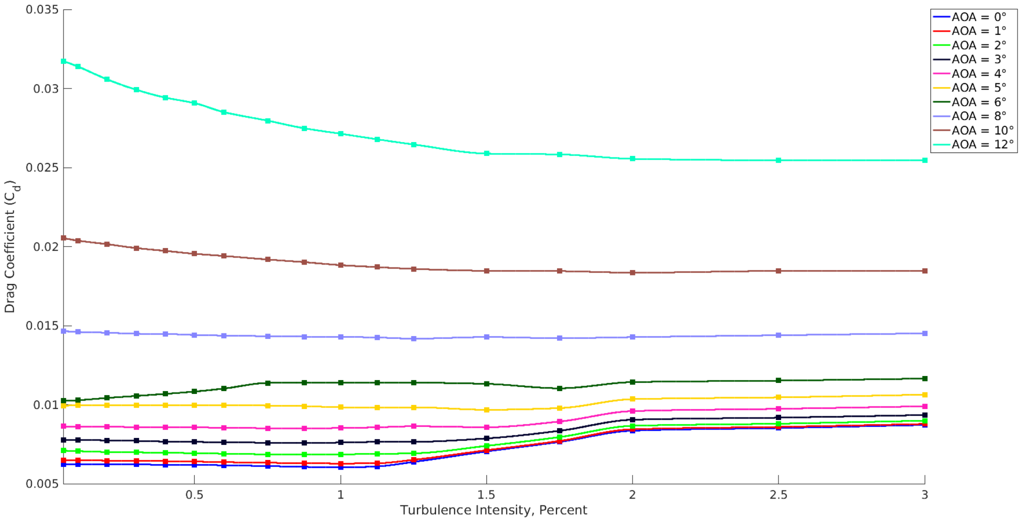

(b) Drag coefficient

Figure 4.6: Parametric Sweep for NACA 0012 Airfoil at Mach = 0.2, Re = 0.5×10^6

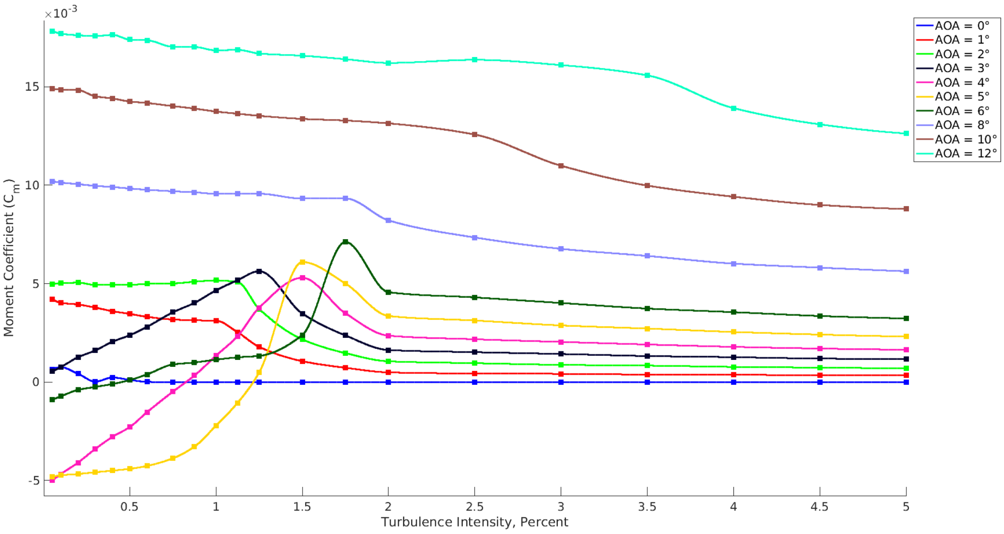

(c) Moment coefficient

Figure 4.6: Parametric Sweep for NACA 0012 Airfoil at Mach = 0.2, Re = 0.5×10^6 (cont.)

Re = 500,000

Fig. 4.6 shows the results of the parametric sweep for the NACA 0012 airfoil at a Reynolds number of 500,000. Most of the variations are relatively smooth. Similar to the S809, the lift curves remain relatively constant as FSTI varies. At low AOA, drag also does not change much at low values of FSTI up to 1.0%. From 1.0% to 2.0%, drag increases noticeably with FSTI. At high AOA, the drag increases as FSTI increases. Moment decreases as FSTI increases, with the exception of AOA 3° to 6°. At these AOA, moment first increases to a peak between FSTI values of 1.25% and 1.75% before decreasing again as FSTI increases.

Fig. 4.7 presents the pressure and friction plots for 5°, 6°, and 12° AOA. As

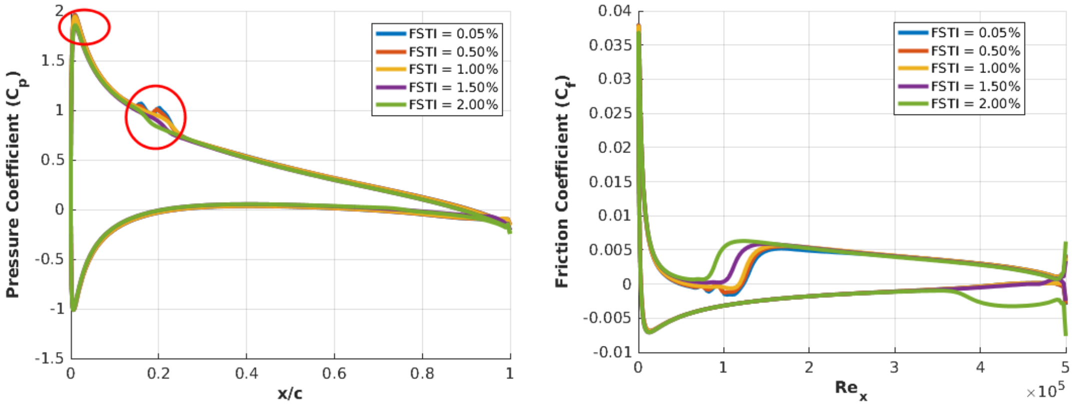

(a) Pressure - AOA = 5°

(b) Skin Friction - AOA = 5°

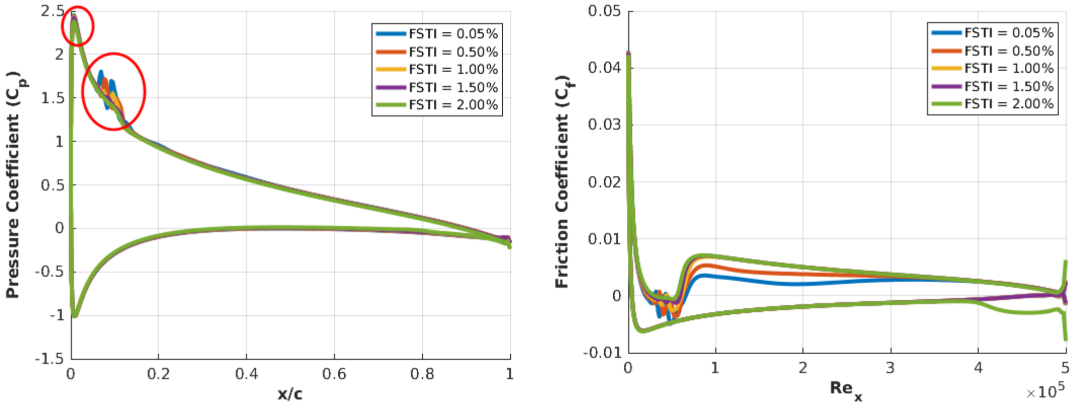

(c) Pressure - AOA = 6°

(d) Skin Friction - AOA = 6°

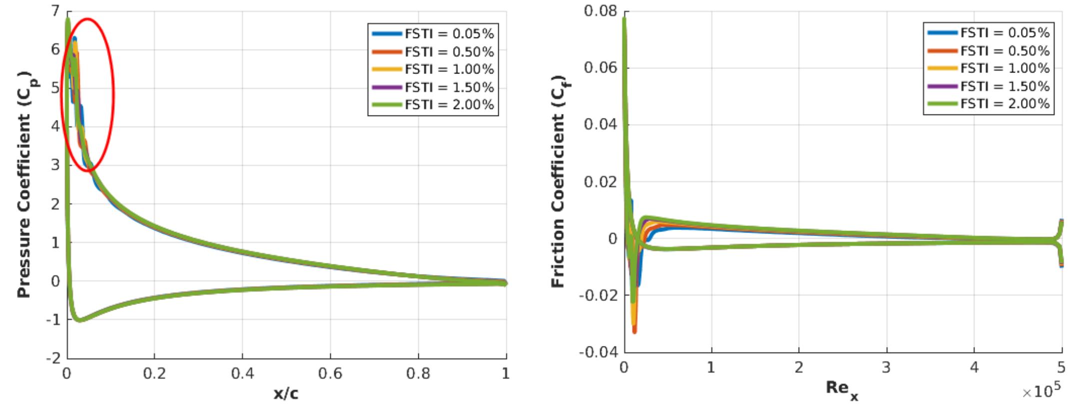

(e) Pressure - AOA = 12°

(f) Skin Friction - AOA = 12°

Figure 4.7: Pressure and Friction Plots for NACA 0012 Airfoil, Re $= 0.5 \times 10^6$, Mach $= 0.2$

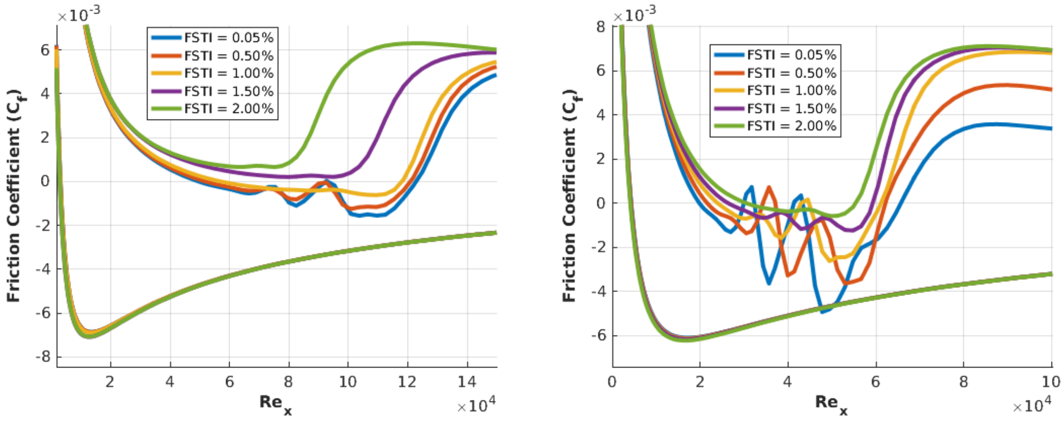

(a) AOA = 5°

(b) AOA = 6°

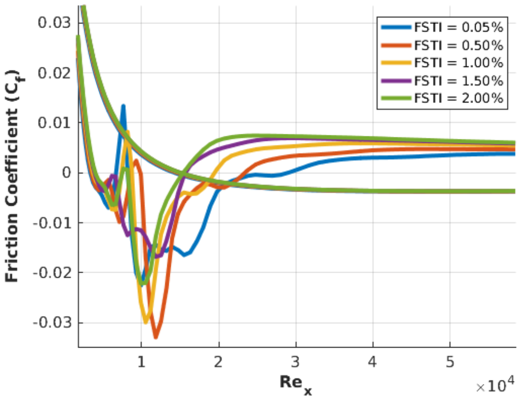

(c) AOA = 12°

Figure 4.8: Zoomed in Skin Friction Plots for NACA 0012 Airfoil, Re = 0.5×10^6, Mach = 0.2

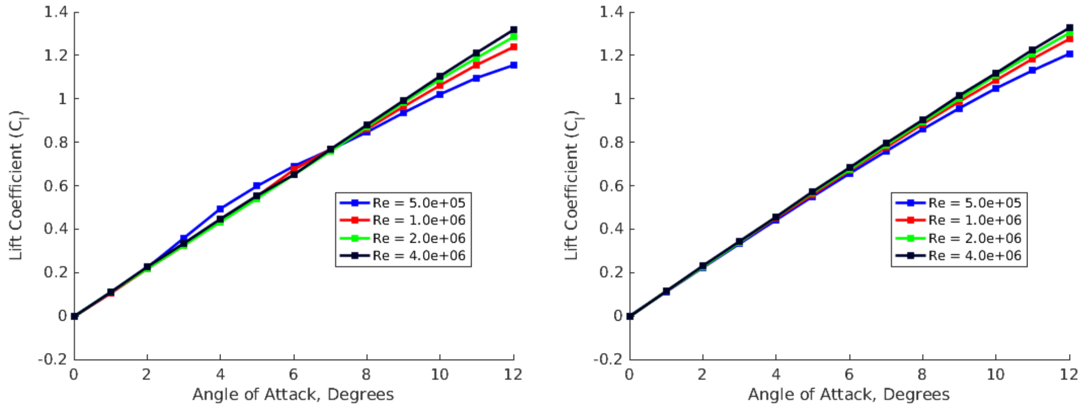

(a) FSTI = 0.05%

(b) FSTI = 3.0%

Figure 4.9: NACA 0012 - Coefficient of Lift, Mach = 0.2

can be seen from the skin friction graphs, the flow remains laminar on the bottom surface, with the exception of the 2% FSTI case for 5° and 6° AOA. Fig. 4.8 zooms in on the separation bubble region. At this Reynolds number, at the lower FSTI values, two separation bubbles form. After the first bubble, the flow reattaches without becoming fully turbulent, before forming a second separation bubble. The flow finally transitions fully after this second bubble. At 5° AOA, only the 0.05% and 0.5% FSTI cases exhibit this double separation bubble, while at 6° AOA, the phenomenon occurs for all the FSTI values besides 2.0%. At 12° AOA, all five FSTI values have the double separation bubble. This double separation bubble does not occur at Reynolds numbers of 2 million and higher, as will be shown in later sections.

Since the two separation bubbles are near the leading edge of the airfoil on the upper surface, they effectively add positive camber to the airfoil. This results in an increase in suction pressure at the leading edge, which in turn increases the lift. This is why the suction peak in the pressure graphs is slightly higher for the cases which have multiple separation bubbles. This also accounts for the increase in lift for the Re = 500,000 case at the moderate angles of attack, as shown in Fig. 4.9. As FSTI varies, the bubble locations move, which is why there is a steep increase in pitching moment at the moderate angles of attack for low FSTI values in Fig. 4.6c. The steep increase is limited to the region with the separation bubbles. At the higher FSTI values, the flow undergoes natural transition and the moment begins to decrease as FSTI increases.

$\mathbf{Re = 1 \times 10^6}$

The results of the sweep for a Reynolds number of 1 million are presented in Fig. 4.10. For this sweep, certain cases did not converge smoothly to a single value, but rather resulted in repeating oscillations, as can be seen in Fig. 4.11. In order to obtain the final aerodynamic coefficients, the results were averaged from peak to peak for the last three to five oscillations. Table 4.2 lists the cases where this method was applied. The different methods used to obtain the quantities of interest resulted in a noticeable jump in values in the moment coefficient graph in Fig. 4.10.

Fig. 4.12 shows the skin friction plots for 5°, 6°, and 12° AOA cases. Similar trends to the Reynold number of 500,000 cases can be seen. Fig 4.13 shows the portion of the skin friction plots where the separation bubbles are present. The double separation bubble phenomenon is present for an FSTI value of 0.05% at 5° AOA, for FSTI values of 0.05% - 1.0% at 6° AOA, and for all of the FSTI values at 12° AOA except for FSTI of 1.5%. One noticeable difference between Reynolds

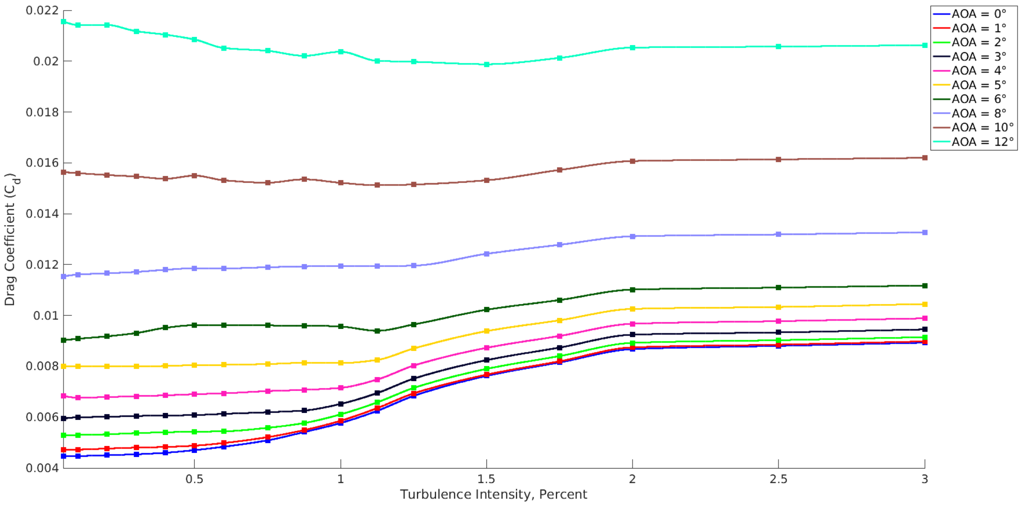

(a) Drag coefficient

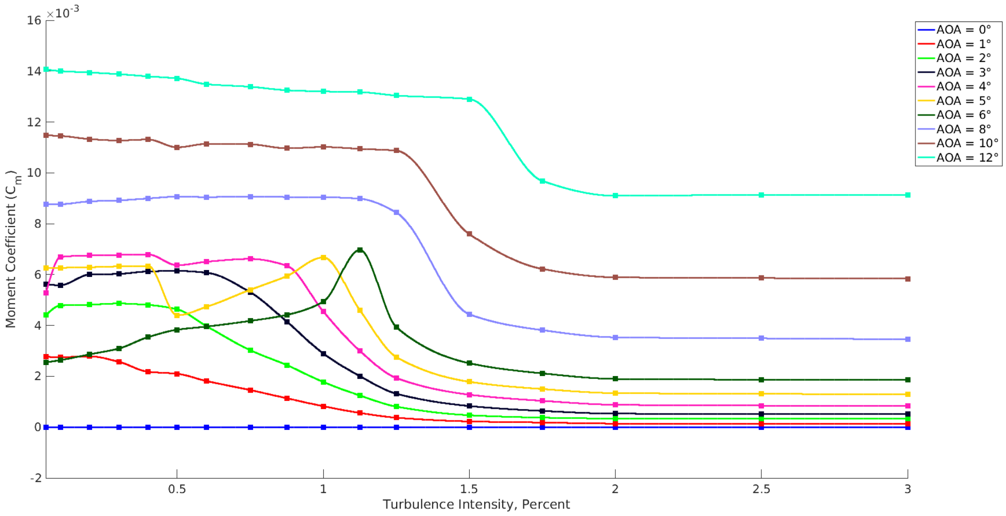

(b) Moment coefficient

Figure 4.10: Parametric Sweep for NACA 0012 Airfoil at Mach = 0.2, Re = 1×10^6, Mach = 0.2

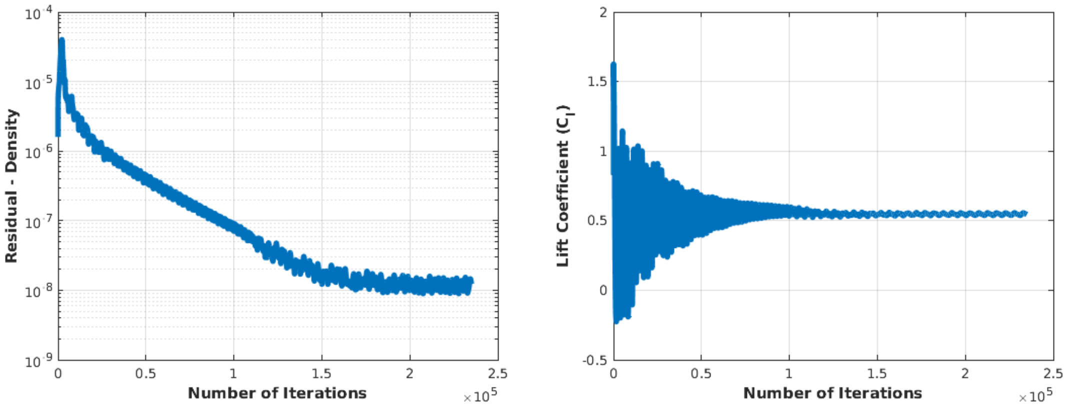

(a) Density Residual (b) Coefficient of Lift

Figure 4.11: Convergence Oscillations - NACA 0012 - Mach = 0.2, Re = 1×10^6, AOA = 5°, FSTI = 0.1%

numbers 500,000 and 1 million is that the bottom surface is no longer laminar for the Reynolds number of 1 million and instead undergoes natural transition for all of the AOA. It can also be noted that as angle of attack increases, the transition location moves closer to the leading edge on the upper surface and closer to the trailing edge on the bottom surface. One can also see that, as FSTI varies for the 5° AOA case, there is a greater change in transition location, but for 6° and 12° AOA, there is only a small amount of change in transition location.

Re = 2×10^6

Fig. 4.14 shows the sweep results for a Reynolds number of 2 million. When compared to the lower Reynolds number, one can observe that there is more change in drag as FSTI increases, especially at the higher angles of attack. At low Reynolds number, the drag is relatively constant at these higher angles. This can be explained by examining the skin friction plots in Fig. 4.15. As can be seen

Angle of Attack (degrees)	**FSTI (percent)**
4	0.1 - 0.4
5	0.05 - 0.4

Table 4.2: NACA 0012 - Mach = 0.2, Re = 1×10^6, Mach = 0.2 - Peak-to-Peak Averaged Cases

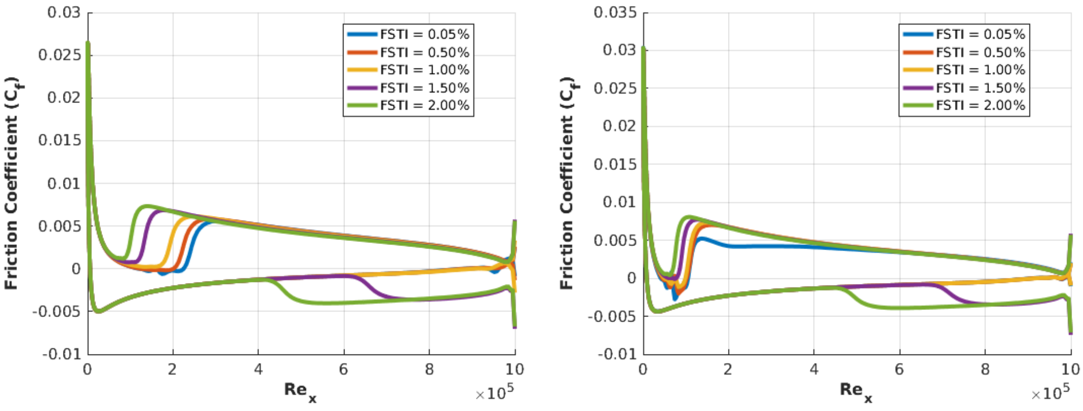

(a) AOA = 5°

(b) AOA = 6°

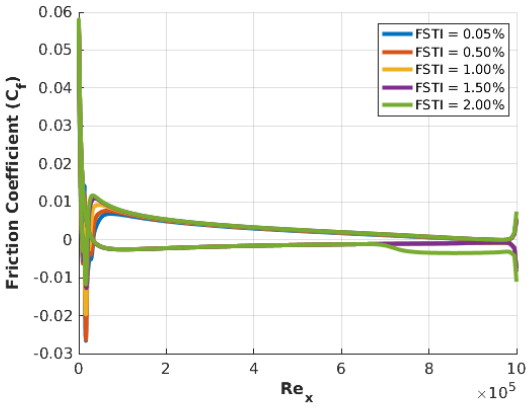

(c) AOA = 12°

Figure 4.12: Skin Friction Plots for NACA 0012 Airfoil, Re = 1.0×10^6, Mach = 0.2

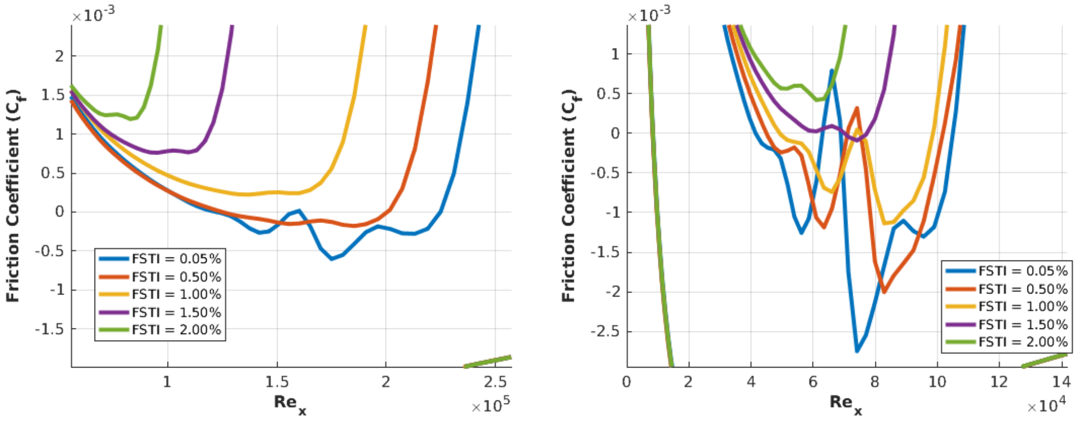

(a) AOA = 5°

(b) AOA = 6°

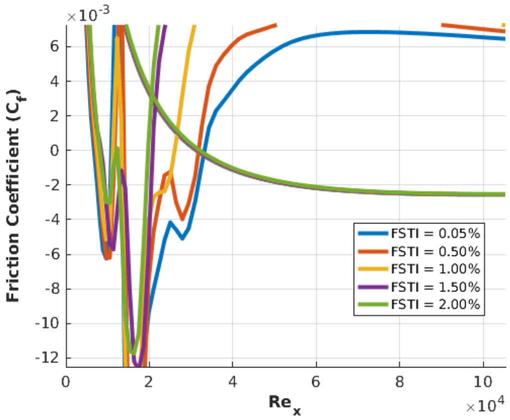

(c) AOA = 12°

Figure 4.13: Zoomed in Skin Friction Plots for NACA 0012 Airfoil, Re $= 1.0 \times 10^6$, Mach = 0.2

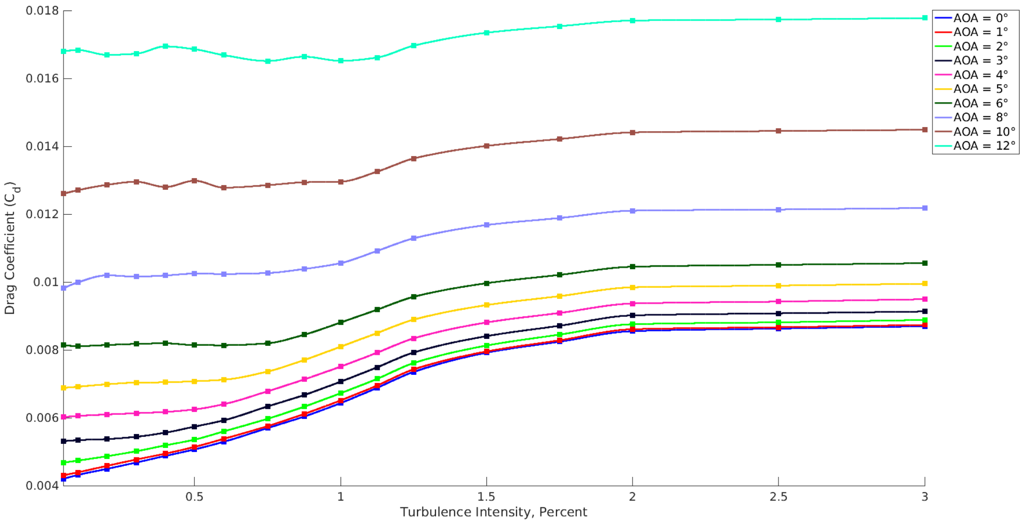

(a) Drag coefficient

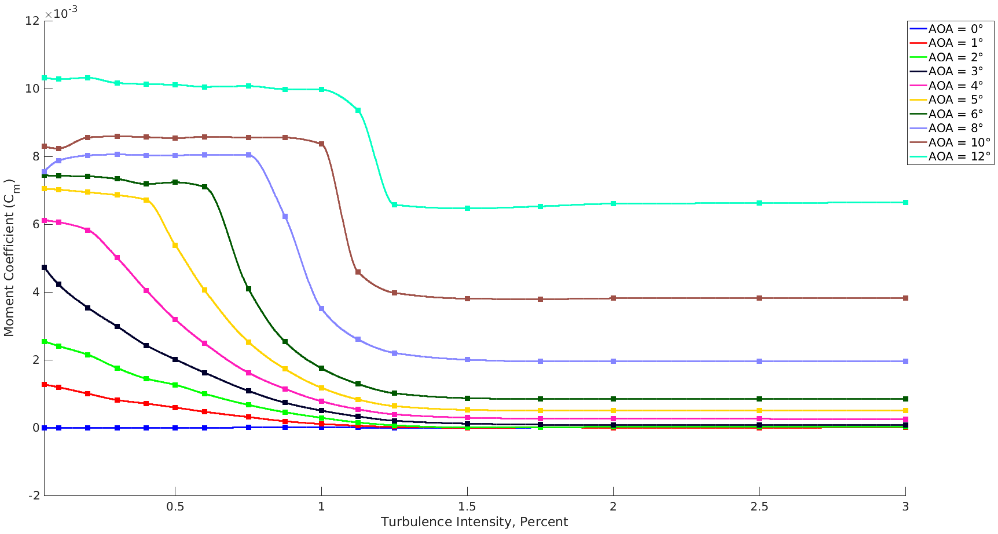

(b) Moment coefficient

Figure 4.14: Parametric Sweep for NACA 0012 Airfoil at Mach = 0.2, Re = 2×10^6, Mach = 0.2

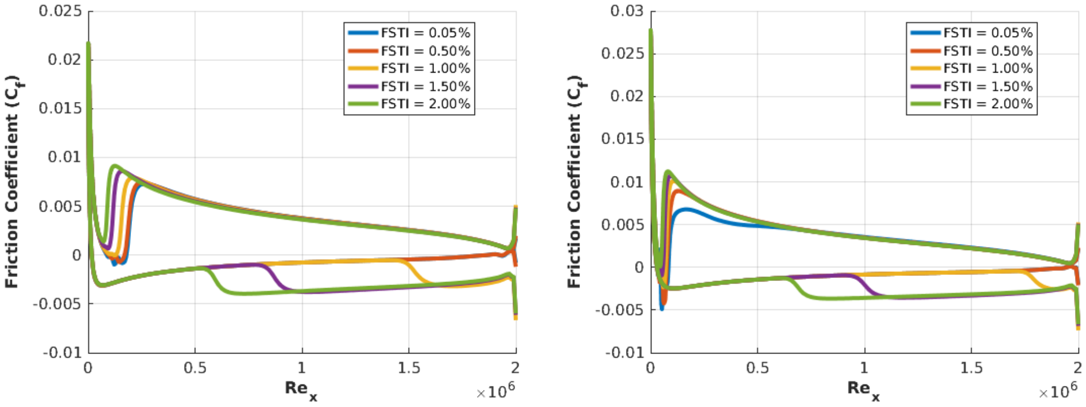

(a) AOA = 6°

(b) AOA = 8°

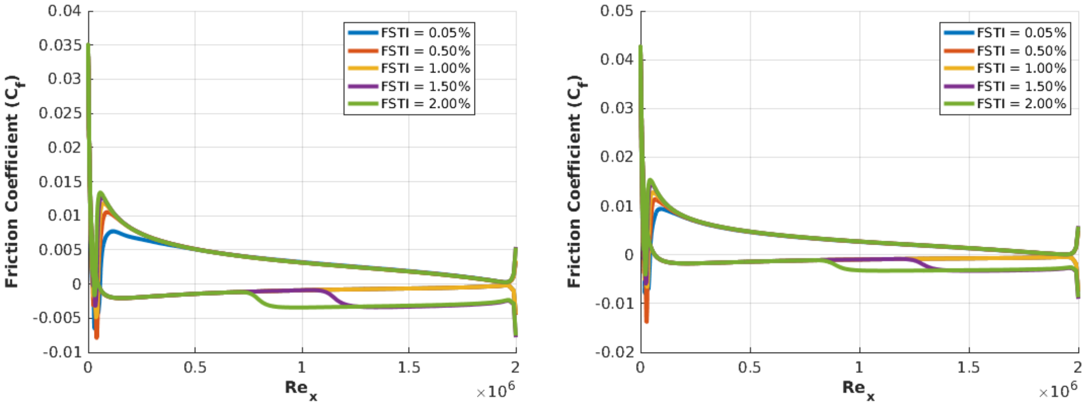

(c) AOA = 10°

(d) AOA = 12°

Figure 4.15: Skin Friction Plots for NACA 0012 Airfoil, Re = 2.0×10^6, Mach = 0.2

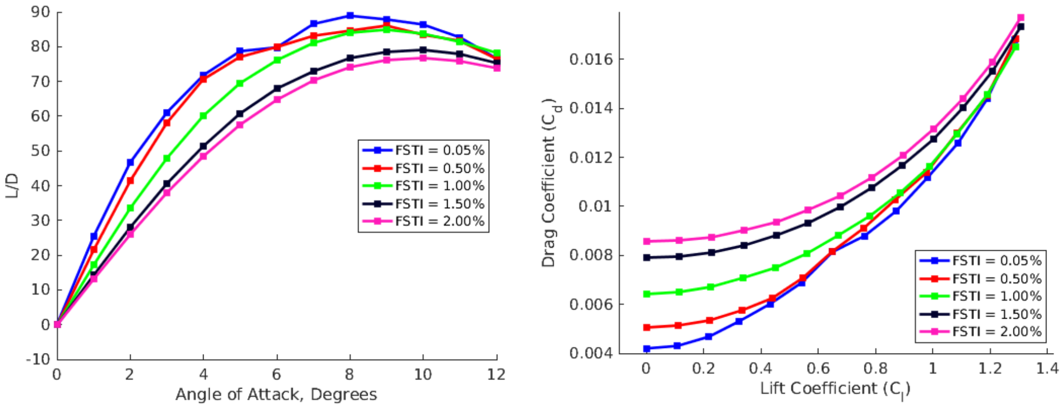

(a) L/D vs Angle of Attack (b) C_d vs C_l

Figure 4.16: NACA 0012 Airfoil at Mach = 0.2, Re = 2×10^6, Mach = 0.2

from these plots, transition on the upper surface occurs at the leading edge at these angles. Since transition occurs so close to the leading edge, the flow is able to stay attached after transition. The turbulent flow therefore has a greater effect on the skin friction, and therefore the drag. On the other hand, at low Reynolds numbers, some separation occurs, allowing the drag to remain constant.

It can also be noted that the sharp increases in moment are no longer present for a Reynolds number of 2 million. Instead, as angle of attack increases, there is a sudden decrease in moment which becomes steeper and occurs at higher FSTI values as angle of attack increases. When examining the skin friction plots, it becomes apparent that this sudden drop in moment is correlated to transition on the bottom surface. At the lower FSTI values, the flow has a small separation bubble near the trailing edge of the bottom surface; for the higher FSTI values, natural transition occurs near mid-chord. The separation bubble results in a virtual increase in reverse camber, which in turn affects the moment coefficient. Therefore, there is sharp drop in moment when comparing the low FSTI cases which have this trailing edge separation bubble and the higher FSTI values which have natural transition.

Compare the pitching moment for the S809 airfoil (Fig. 4.2) and the pitching moment for the NACA 0012 at a Reynolds number of 2 million (Fig. 4.14). Note that even though the freestream Mach and Reynolds numbers are identical, the trends are significantly different. The NACA 0012 airfoil pitching moment decreases as FSTI increases, including the region of sharp decreasing pitching moment. On the other hand, the pitching moment increases as FSTI increases for the S809 airfoil.

Fig. 4.16 shows the L/D curve and drag polar for various values of FSTI. At the lower FSTI values, there is a larger peak in the L/D curve but a faster drop off. The higher FSTI values stay flatter. All of the FSTI curves approach a similar value at the high angles of attack.

$\mathbf{Re = 4 \times 10^6}$

The results for the Reynolds number of 4 million sweep are shown in Fig. 4.17. This case is very similar to the case for a Reynolds number of 2 million case. There is a large change in drag at the higher angles of attack due to the large region of attached flow. However, there is a noticeable difference in the moment coefficient plot. The sharp decrease in moment has shifted left (i.e. at lower FSTI values). Fig. 4.18 shows the skin friction for an angle of attack of 12 degrees. When comparing this case against lower Reynolds numbers, one can see that the

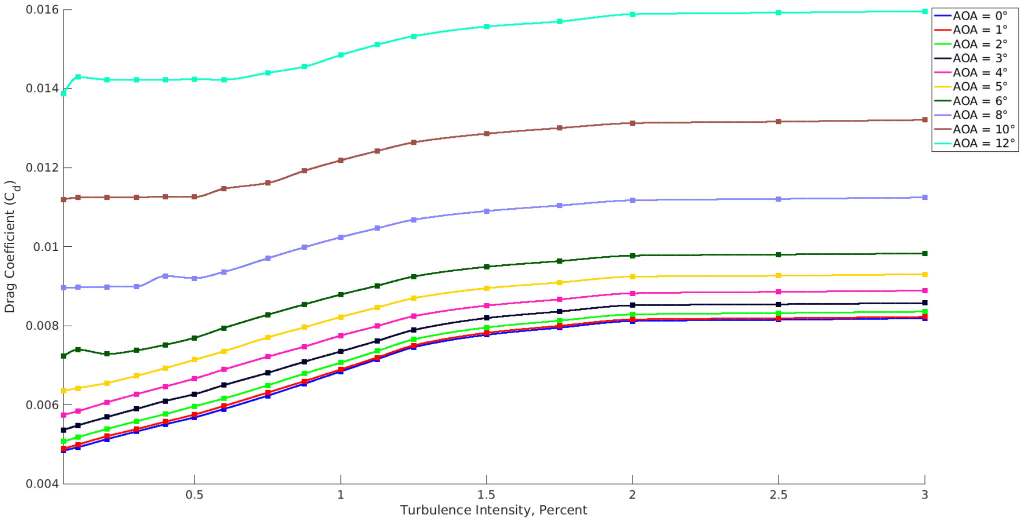

(a) Drag coefficient

Figure 4.17: Parametric Sweep for NACA 0012 Airfoil at Mach = 0.2, Re = 4×10^6

transition location on the bottom surface has moved forward. Also, the 1% FSTI case also naturally transitions at this Reynolds number.

4.4 SC1095 Airfoil

The SC1095 airfoil was designed by Sikorsky Aircraft for use on the Black Hawk UH-60A helicopter. It is a cambered airfoil witha maximum thickness of 9.5%. The airfoil can be considered to be representative of modern airfoil design [48]. In this study, the Mach number was varied for this airfoil from 0.2 to 0.8. The results of the parametric study are presented in Figs. 4.19 - 4.30. Note that for the sweeps with a Mach number of 0.6 or greater, the results have been omitted for high angles of attack (i.e. over 6 degrees). These cases did not result in stable

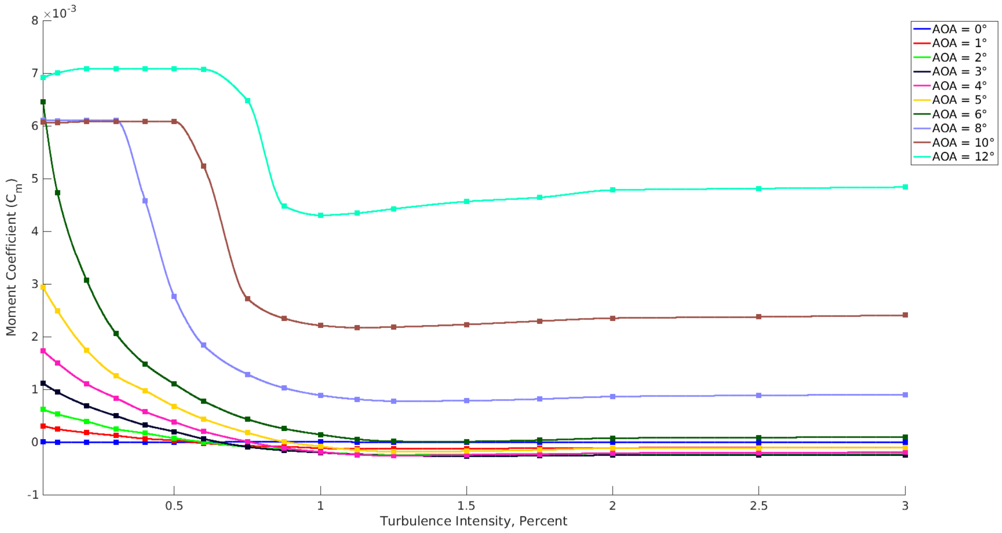

(b) Moment coefficient

Figure 4.17: Parametric Sweep for NACA 0012 Airfoil at Mach = 0.2, Re = 4×10^6 (cont.)

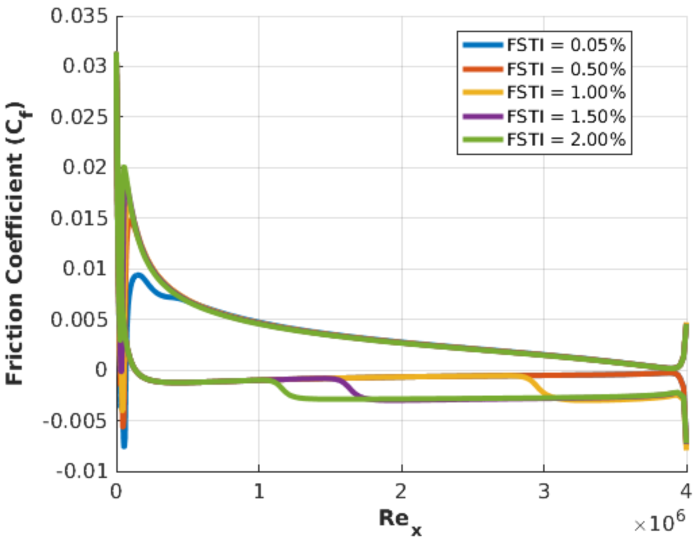

Figure 4.18: Skin Friction Plot for NACA 0012 Airfoil, Re = 4.0×10^6, Mach = 0.2, AOA = 12 degrees

steady solutions. This is due to unsteady transonic effects due to shock induced separation, which are beyond the scope of this work.

Mach 0.2

Fig. 4.19 shows the results for a Mach number of 0.2 and a Reynolds number of 2 million. The plots show trends similar to the NACA 0012 at the same conditions. Comparing the results of both the NACA 0012 and SC1095 against the S809 airfoil, one can see that minimum drag for the NACA 0012 and SC1095 airfoils is lower than the S809 airfoil. This makes sense, since the NACA 0012 and SC1095 airfoils are used for helicopter rotors and therefore drag minimization was a significant design consideration. On the other hand, the S809 airfoil's primary design objective was promoting laminar flow.

Fig. 4.20 shows the L/D plot and drag polar for various FSTI values. From the L/D plot, it can be seen that the low FSTI curves (0.05% and 0.5%) are close to each other, indicating there is not much variance. This is attributed to the smaller drag bucket (shown in the drag polar graph) when compared to NACA 0012. This smaller drag bucket is due to the camber of the SC1095 airfoil.

Fig. 4.21 shows the skin friction plots for the cases at Mach 0.2. Once again, the graphs show similar trends to the NACA 0012 results (see Fig. 4.15). However, for the SC1095 airfoil, at the high angles of attack and lower values of FSTI, the separation bubble does not occur right at the leading edge, but rather slightly later.

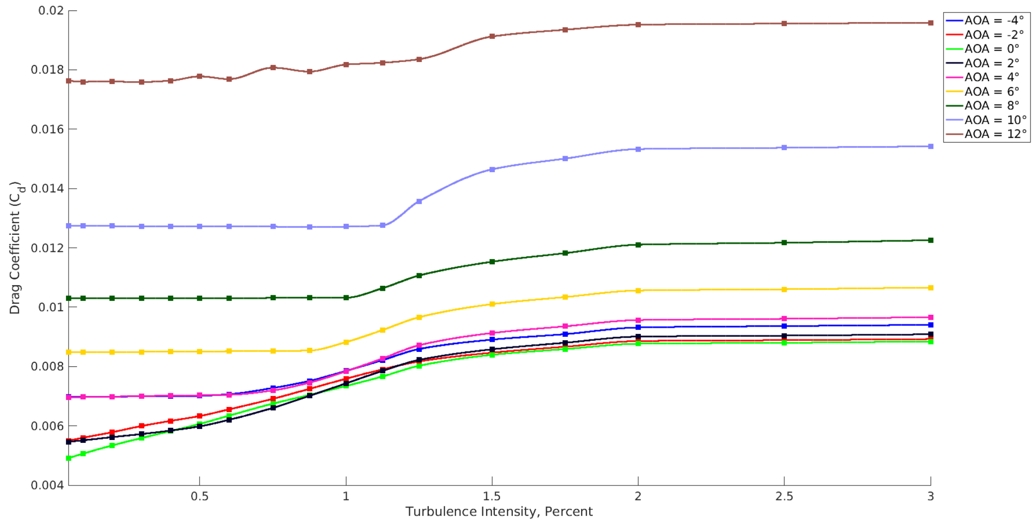

(a) Drag coefficient

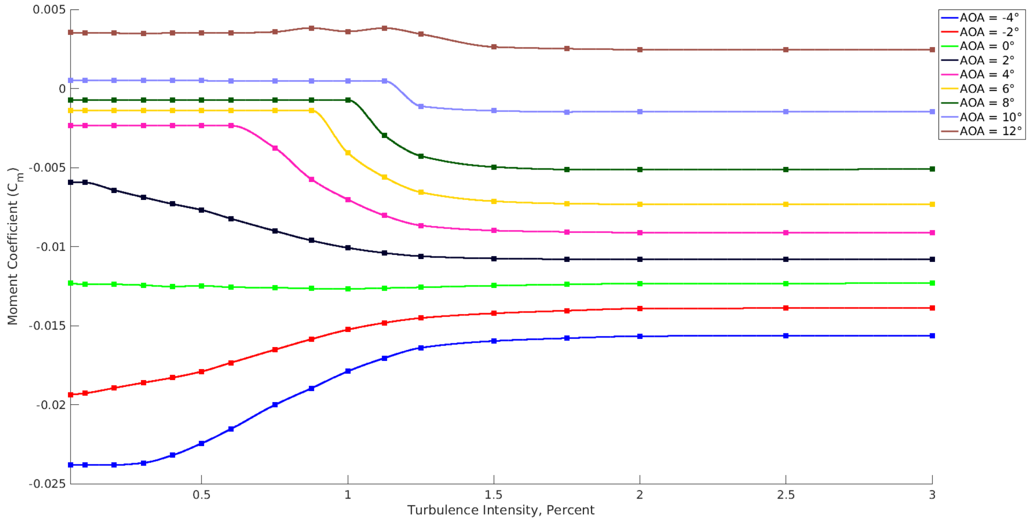

(b) Moment coefficient

Figure 4.19: Parametric Sweep for SC1095 Airfoil at Mach = 0.2, Re = 2×10^6

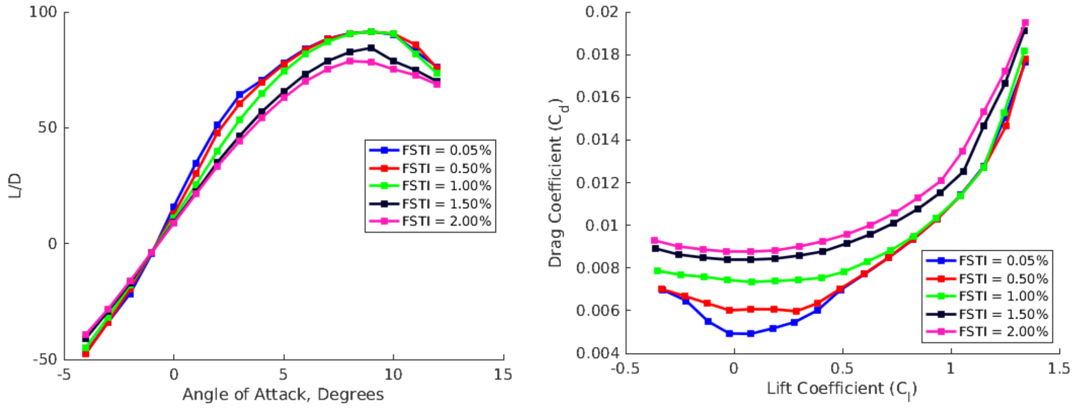

(a) L/D vs Angle of Attack (b) C_d vs C_l

Figure 4.20: SC1095 Airfoil at Mach = 0.2, Re = 2×10^6

Mach 0.4

Fig. 4.22 shows the drag coefficient for the Mach 0.4 sweep. Note the large increase in drag between AOA of 10° and 12°. Fig. 4.23 shows the Mach contours at these angles of attacks for FSTI values of 0.5% and 2.0%. From these plots, it can be seen that there is not much difference between the 0.5% and 2.0% cases. However, when comparing the 10° and 12° AOA cases, the Mach number is observed to be higher for the 12 degree case near the leading edge of the airfoil. The boundary layer is also observed to be much thicker for the 12° AOA case. This thicker boundary layer negatively affects the effective camber at the trailing edge. This results in a small drop off in lift and a large jump in drag.

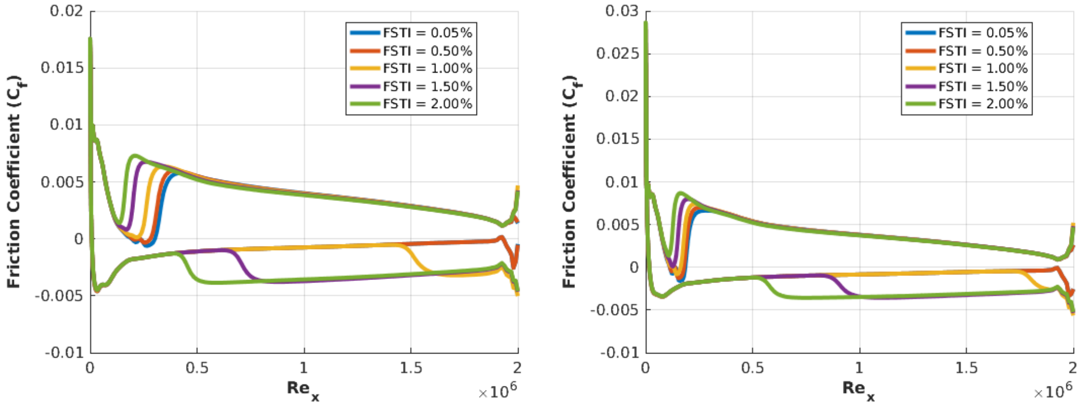

(a) AOA = 4°

(b) AOA = 6°

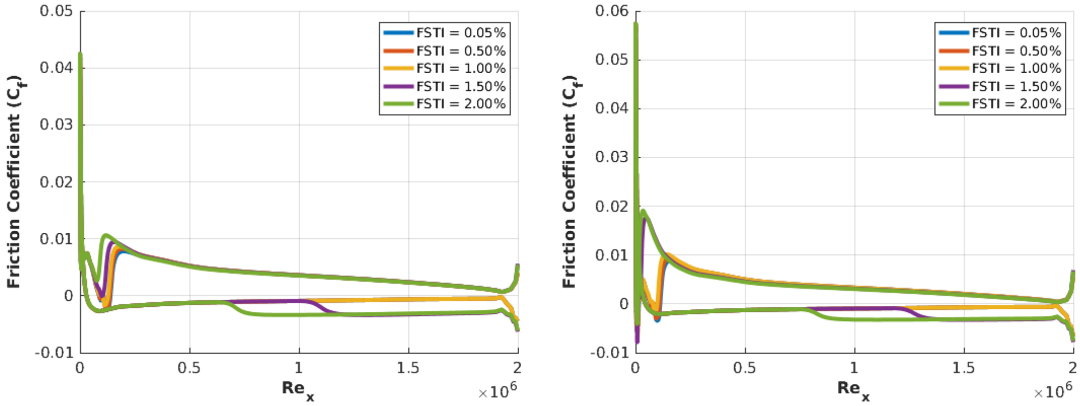

(c) AOA = 8°

(d) AOA = 10°

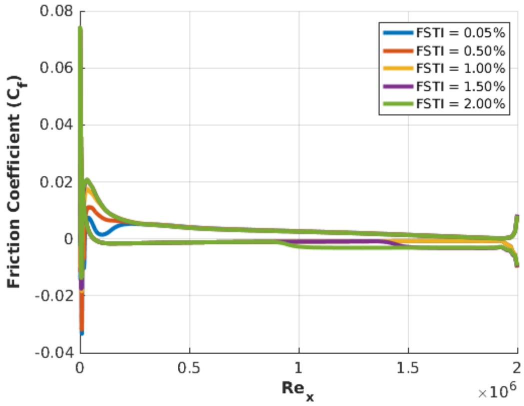

(e) AOA = 12°

Figure 4.21: Skin Friction Plots for SC1095 - Mach = 0.2

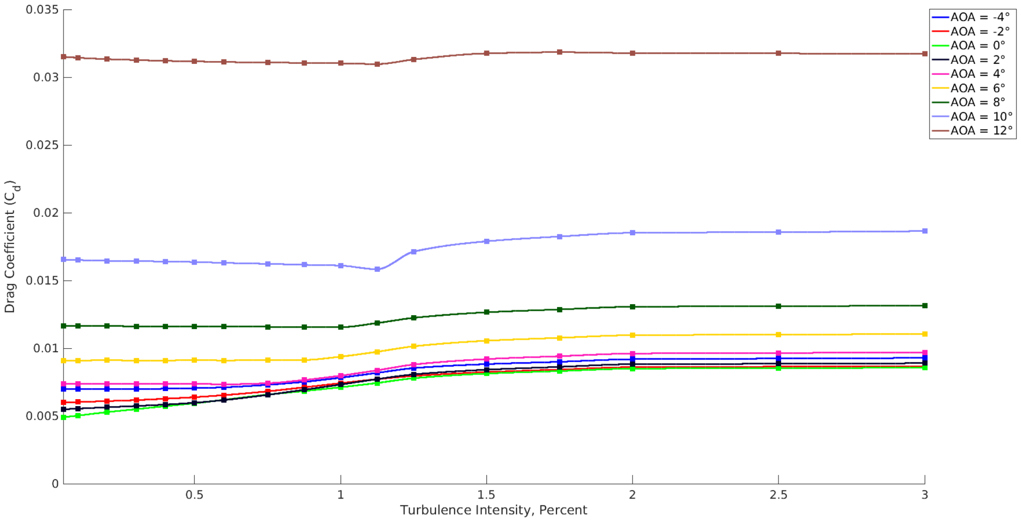

Figure 4.22: Parametric Sweep for Drag Coefficient - SC1095 Airfoil at Mach = 0.4, Re = 2×10^6

Mach 0.6

Fig. 4.24 shows the coefficient of drag for the Mach 0.6 sweep. The graph resembles the graphs for the Mach 0.4 cases. However, the jumps in drag have increased between each angle of attack. The magnitude of the jump between 5° and 6° AOA for Mach 0.6 is of the same magnitude as the jump between 10° and 12° AOA for Mach 0.4. It can also be noted that for each curve, drag remains fairly constant before a noticeable jump as FSTI increases. After this jump, drag remains constant. Fig. 4.25 compares the Mach contours for FSTI values of 0.5% and 2.0% for the 6° AOA case. The spike in Mach along the airfoil indicates that a shock has occurred there. However, similar to the Mach 0.4 case, there is not much change between FSTI values of 0.5% and 2.0%.

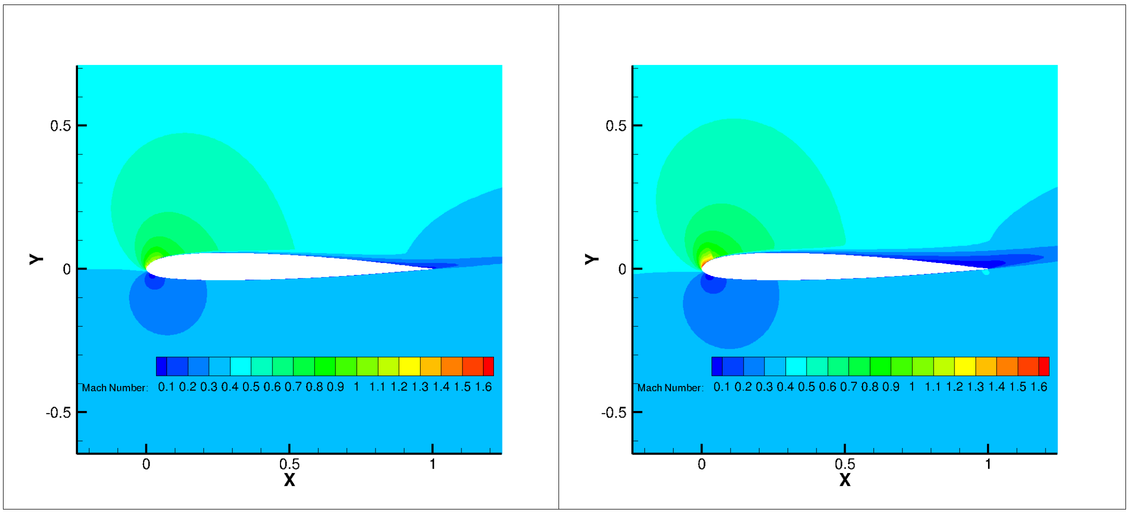

(a) AOA = 10°, FSTI = 0.5%

(b) AOA = 12°, FSTI = 0.5%

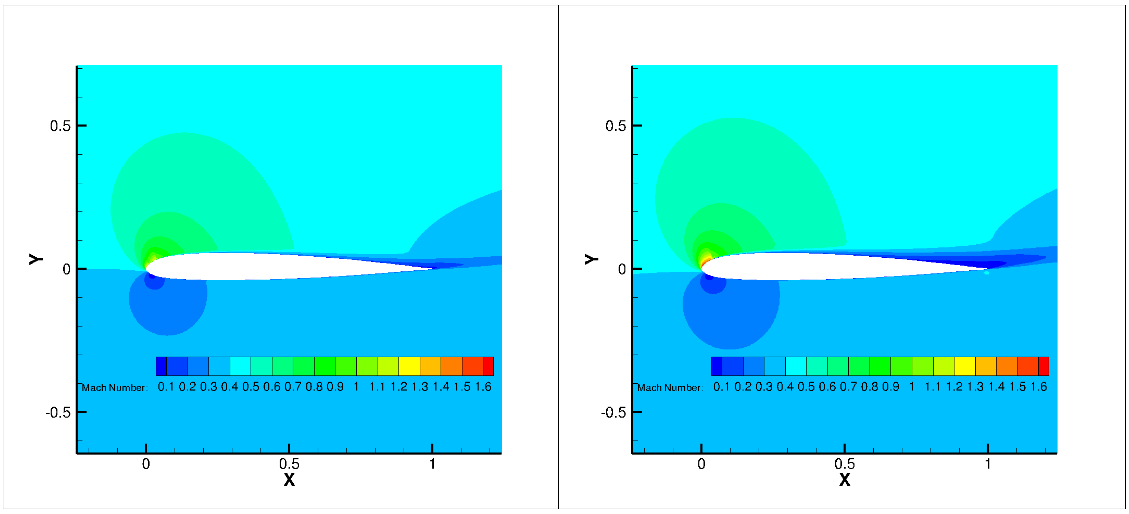

(c) AOA = 10°, FSTI = 2.0%

(d) AOA = 12°, FSTI = 2.0%

Figure 4.23: Mach Contours for SC1095 Airfoil at Mach = 0.4, Re = 2×10^6

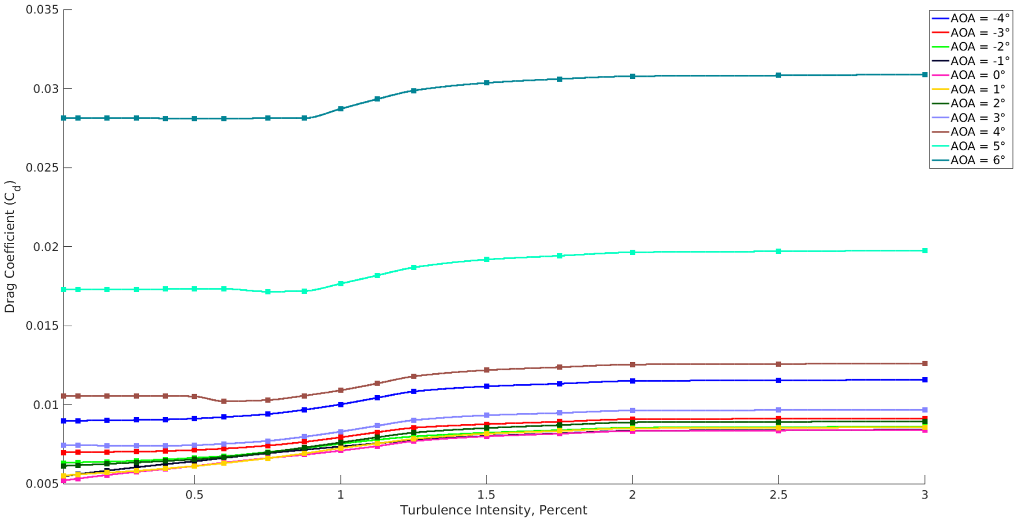

Figure 4.24: Parametric Sweep for Drag Coefficient - SC1095 Airfoil at Mach = 0.6, Re = 2×10^6

Fig. 4.26 shows the pressure and skin friction plots. Observe that the upper surface is virtually unaffected as FSTI increases. However, the transition location moves forward as the FSTI increases. For this case, there is a large jump in the transition location between 1% and 1.5%. This corresponds to the increase in drag that was noted earlier in Fig 4.24.

Mach 0.7

Fig. 4.27 presents the results of the Mach 0.7 sweep. Note that the lift actually decreases between 4° and 6° AOA. There is also a very large increase in drag and a large decrease in moment between 4° and 6° AOA. Fig. 4.28 shows the Mach contours for the 6° case for FSTI = 0.5% and 2.0%. Unlike the previous Mach numbers, there is a noticeable, albeit still small, difference between the two

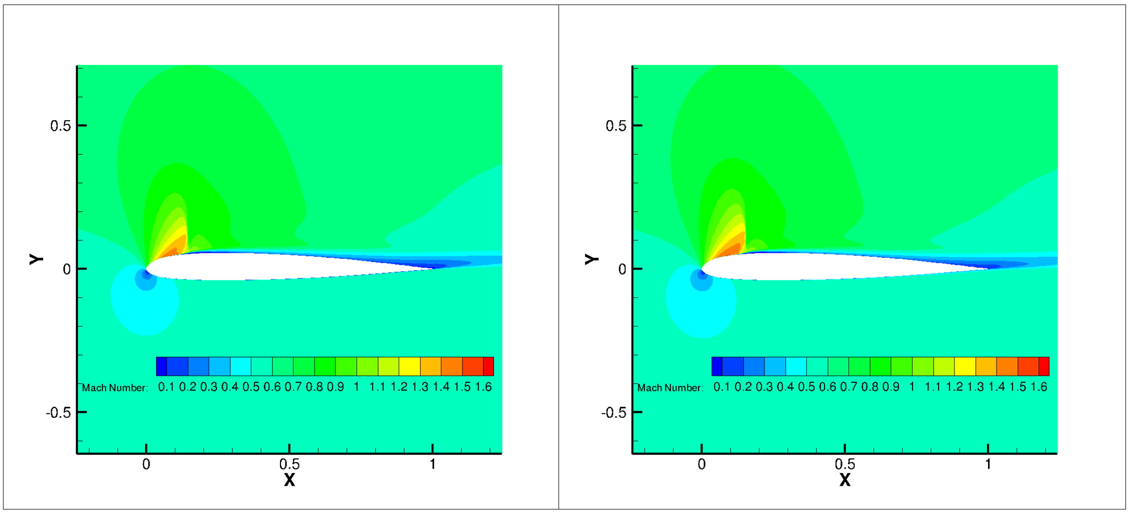

(a) FSTI = 0.5%

(b) FSTI = 2.0%

Figure 4.25: Mach Contours for SC1095 Airfoil at Mach = 0.6, Re = 2×10^6, AOA = 6 degrees

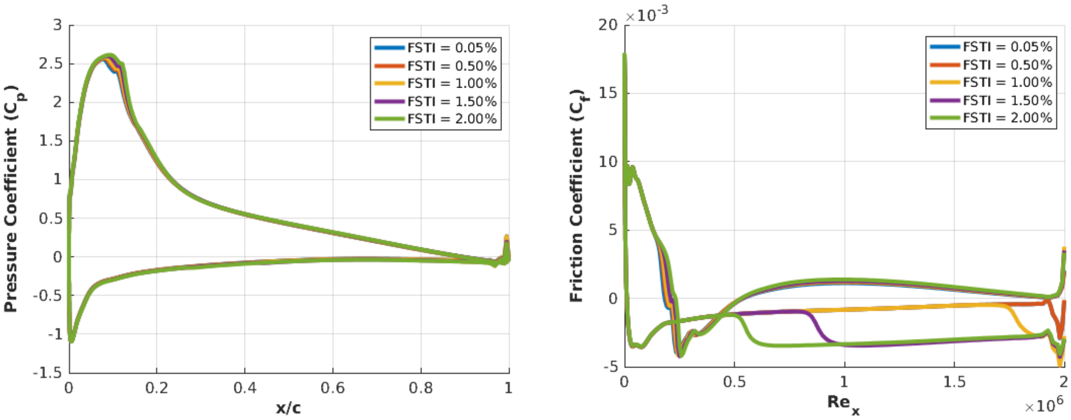

(a) Coefficient of Pressure C_P

(b) Skin Friction C_f

Figure 4.26: Pressure and Friction Plots for SC1095 Airfoil, Mach = 0.6, AOA = 6 degrees

FSTI values. The shock is stronger for the 2.0% FSTI case. The pressure and skin friction plots are shown in Fig. 4.29. Observe that the low FSTI values result in a small reduction in the suction peak on the upper surface.

Mach 0.8

The lift and moment curves for the Mach 0.8 sweep are presented in Fig. 4.30. There are large jumps in lift between -2°, 0°, and 2° AOA. On the other hand, the lift for 2°, 4°, and 6° AOA are all bunched together. The 2° AOA case is of particular interest, especially between 1.0% and 1.25%. At this point, the lift increases before decreasing again, unlike any of the other angles of attack. The moment also decreases before increasing in this range. The pressure and skin friction plots are provided for this case in Fig. 4.31. The plots reveal why such rapid change in the aerodynamic coefficients occurs between FSTI values of 1.0% and 1.25%. The plots show that the shock has moved downstream. For the 1.0% case, it is evident that the flow becomes turbulent after the shock. The drop in skin friction on the upper surface of the 1.0% FSTI case indicates the shock has occurred, and then the increase in skin friction marks the transition to turbulent flow. The FSTI value of 1.25% leads to flow transition at the shock. The 1.25% FSTI case undergoes transition before the shock. This results in very different skin friction profiles for each case (and lift and moment curves), even though FSTI is only varying by a small amount.

Figs. 4.32 and 4.33 show the Mach contours, pressure, and skin friction plots for the 6° AOA cases. The Mach contours show that at an FSTI of 0.5%, there is a

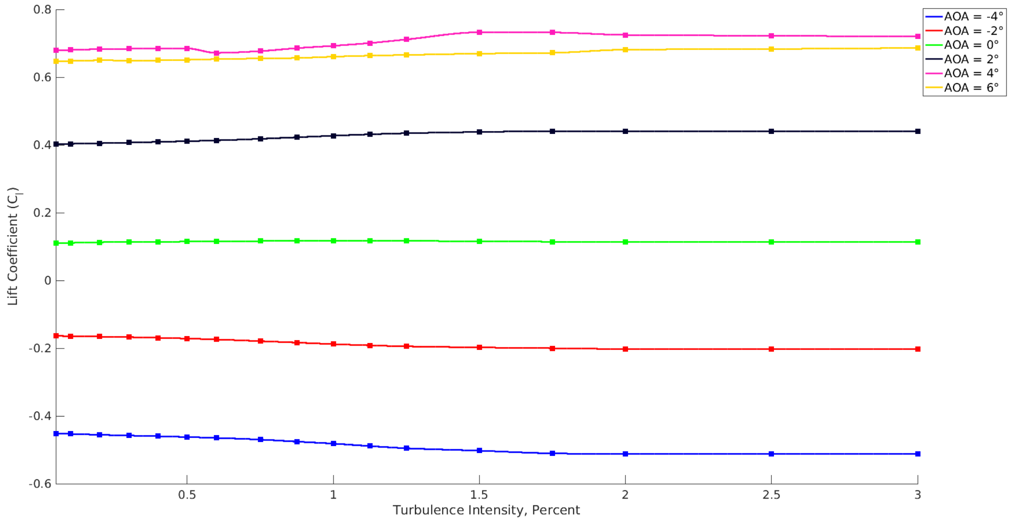

(a) Lift coefficient

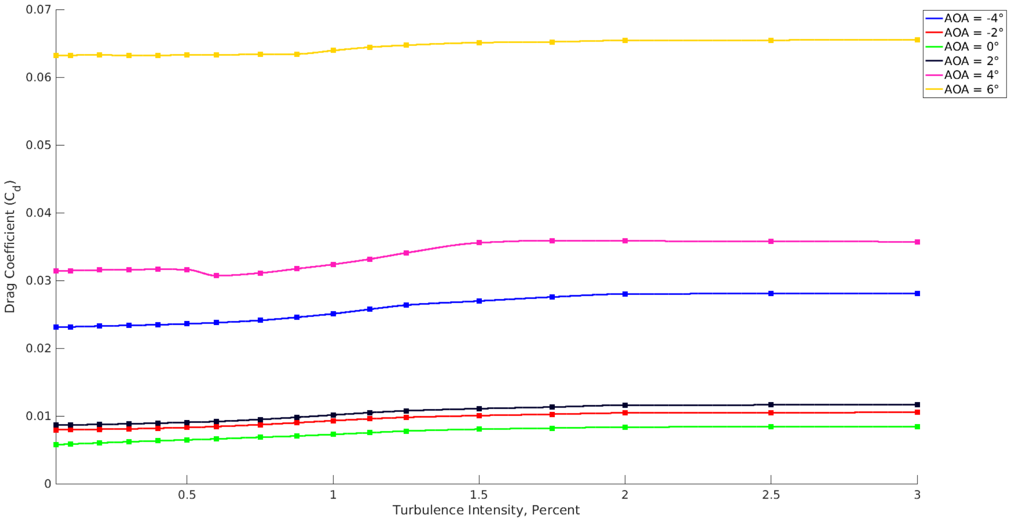

(b) Drag coefficient

Figure 4.27: Parametric Sweep for SC1095 Airfoil at Mach = 0.7, Re = 2×10^6

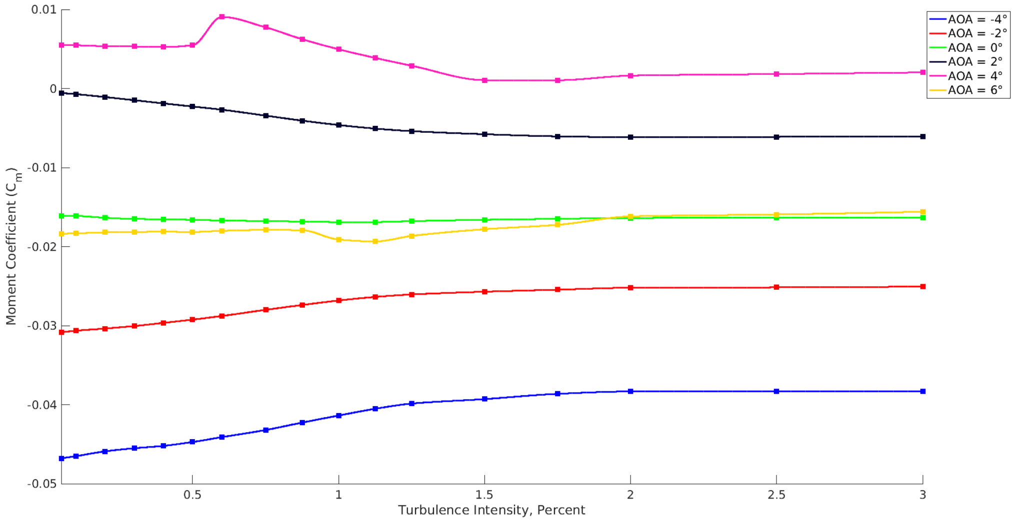

(c) Moment coefficient

Figure 4.27: Parametric Sweep for SC1095 Airfoil at Mach = 0.7, Re = 2×10^6 (cont.)

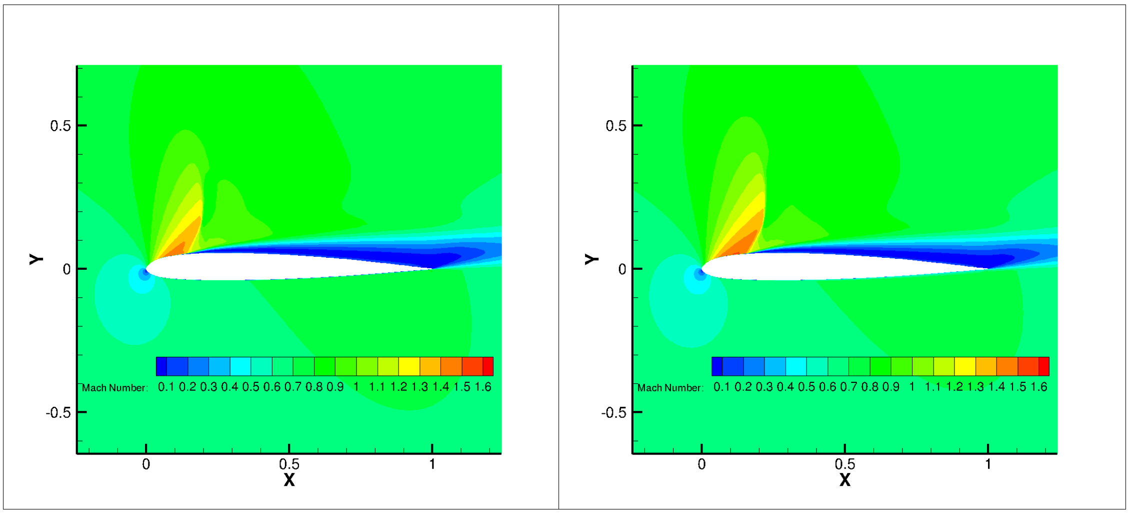

(a) FSTI = 0.5%

(b) FSTI = 2.0%

Figure 4.28: Mach Contours for SC1095 Airfoil at Mach = 0.7, Re = 2×10^6, AOA = 6 degrees

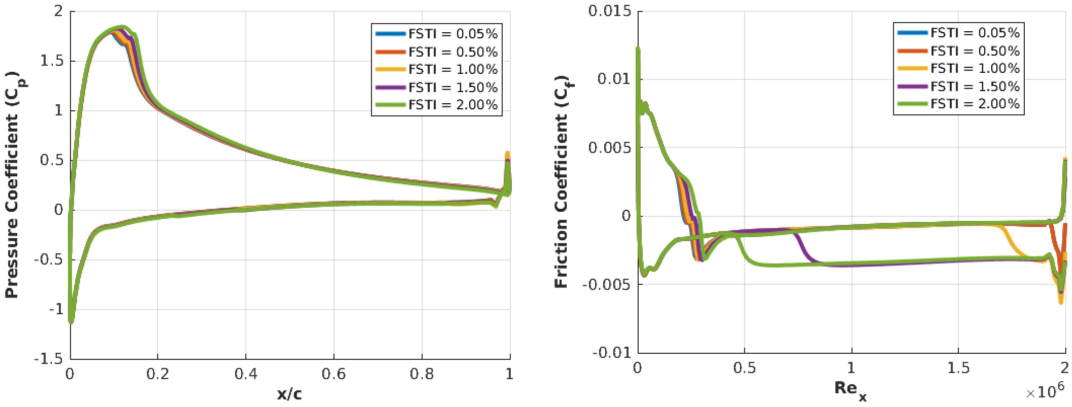

(a) Coefficient of Pressure C_P (b) Skin Friction C_f

Figure 4.29: Pressure and Friction Plots for SC1095 Airfoil, Mach = 0.7, AOA = 6 degrees

weaker shock that occurs closer to the leading edge, which results in a longer separation bubble. The skin friction plot shows that the 2.0% case transitions before the shock, the 1.5% case transitions at the shock, and the low FSTI cases undergo separation-induced transition, as evidenced by the separation bubble. Once again, these differences are responsible for the change in moment in Fig. 4.30.

4.5 RC(4)-10 Airfoil

The RC(4)-10 airfoil was designed by NASA for the inboard section of helicopter rotors [49]. The airfoil was designed to optimize the maximum lift coefficient in order to increase the lift load capacity of the retreating rotor blade. In the present work, the Mach number was varied for this airfoil from 0.2 to 0.8. The results of the parametric studies are presented in Figs. 4.34 - 4.45. Note that, like the SC1095 airfoil, the results have been omitted for high angles of attack (i.e.

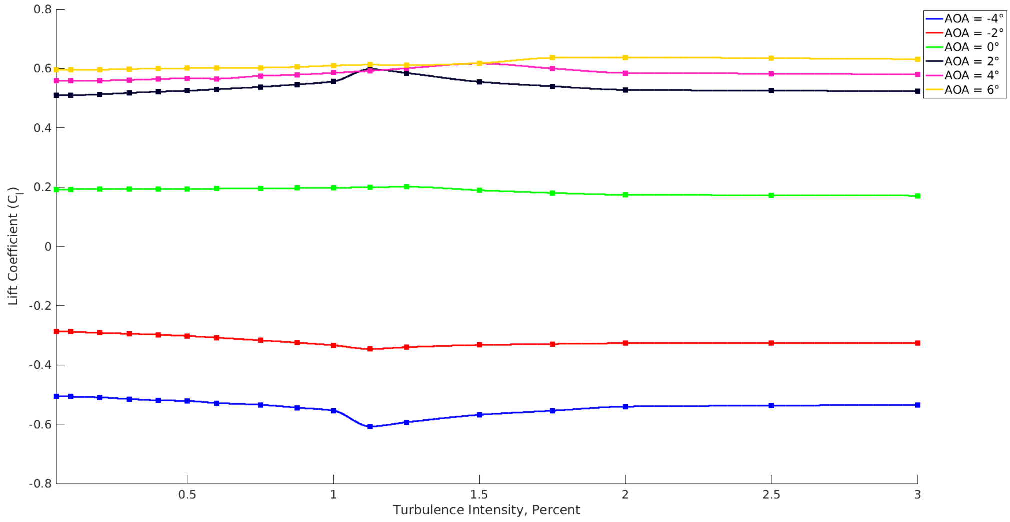

(a) Lift coefficient

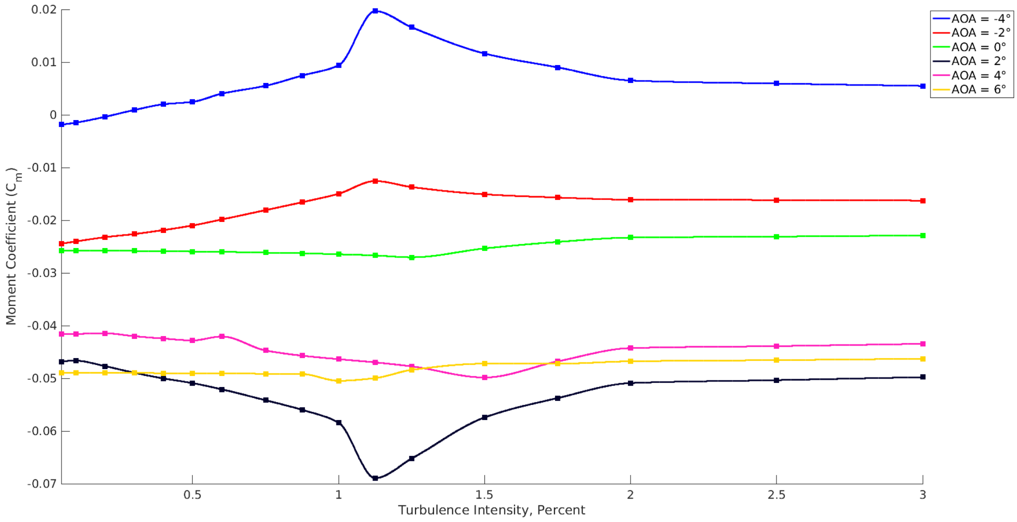

(b) Moment coefficient

Figure 4.30: Parametric Sweep for SC1095 Airfoil at Mach = 0.8, Re = 2×10^6

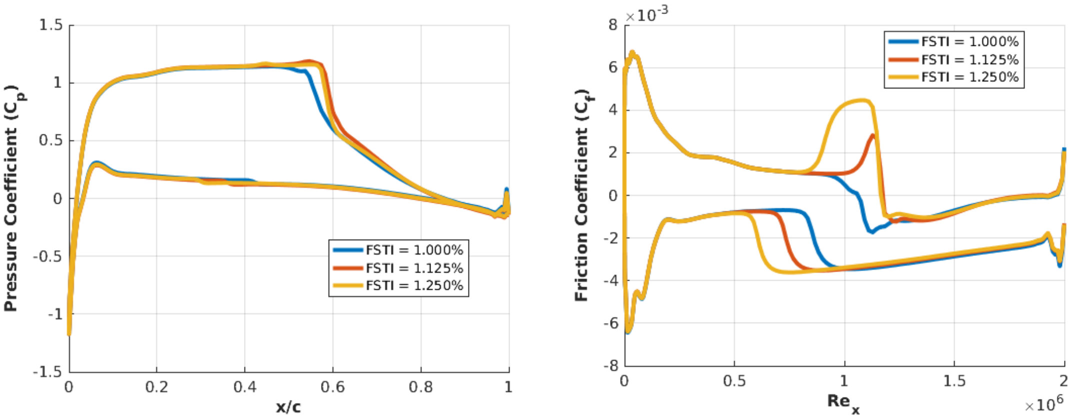

(a) Coefficient of Pressure C_P

(b) Skin Friction C_f

Figure 4.31: Pressure and Friction Plots for SC1095 Airfoil, Mach = 0.8, AOA = 2 degrees

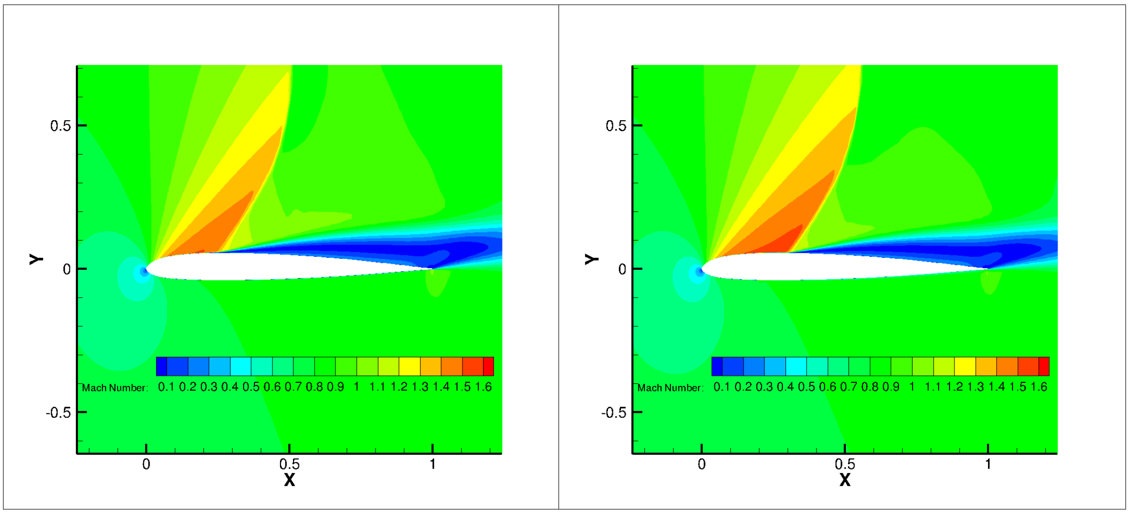

(a) FSTI = 0.5%

(b) FSTI = 2.0%

Figure 4.32: Mach Contours for SC1095 Airfoil at Mach = 0.8, Re = 2×10^6, AOA = 6 degrees

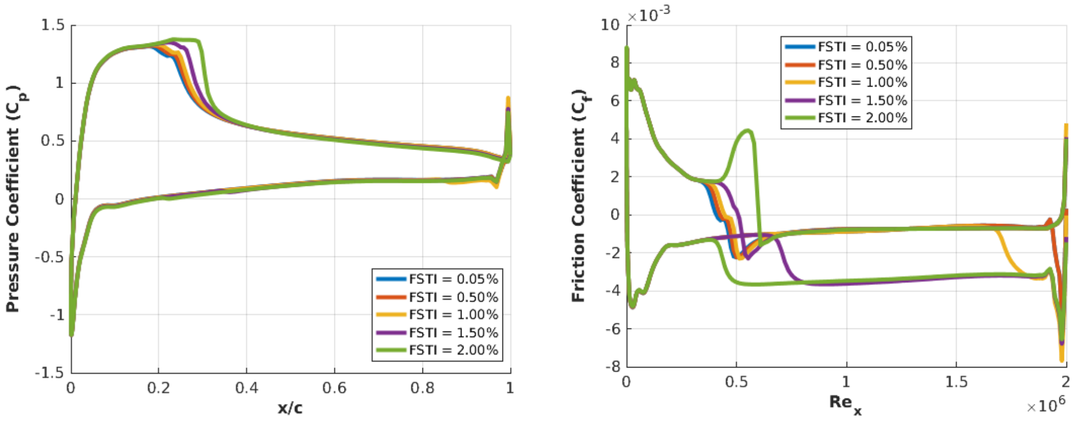

(a) Coefficient of Pressure C_P (b) Coefficient of Skin Friction C_f

Figure 4.33: Pressure and Friction Plots for SC1095 Airfoil, Mach = 0.8, AOA = 6 degrees

over 7 degrees) at high Mach numbers. Also note that, similar to the NACA 0012, certain cases did not converge to a single value, but rather resulted in repeating oscillations (see Fig. 4.11). The values were averaged peak-to-peak for the last three to five oscillations. The cases which were averaged are listed in Table 4.3.

Mach 0.2

Fig. 4.34 shows the results for Mach 0.2 sweep for the RC(4)-10. The drag coefficient plot looks fairly similar to the SC1095 sweep at the same conditions (Fig. 4.19), with the exception of the 2° AOA case, which has a sharp increase in drag around 0.5% FSTI. The 2° and 4° AOA cases also exhibit an increase in moment before decreasing, which was not present in the SC1095 case.

Fig. 4.35 shows the L/D and drag polar plots for this sweep at various FSTI values. Comparing against the SC1095 results (Fig. 4.20), one notes that the

RC(4)-10 is able to achieve higher L/D values as a more modern airfoil. However, besides this, the trends are fairly similar between the two airfoils, although the drag bucket is much sharper for the RC(4)-10 at low FSTI values.

Fig. 4.36 presents the skin friction plots for the Mach 0.2 sweep. One thing to note is the large change in transition location for the 2° AOA case. As the angle of attack increases, the change in the transition location becomes smaller.

Mach 0.4

The results for the Mach 0.4 sweep are presented in Fig. 4.37. Note in Fig. 4.37, that there is a noticeable jump in drag between 0.6% and 0.75% FSTI for the 2° AOA case. However, it is possible that this is due to the fact that the values obtained for the FSTI values from 0.3% to 0.6% at this angle of attack were obtained using peak-to-peak averaging. However, one thing to note when examining the moment graph is that even the lower FSTI values for the 2° AOA case (which were not averaged) are greater than the 4° AOA case. Also, the 4° and 6° AOA cases show the trend of an increasing and then decreasing moment coefficient, which was seen previously.

Fig. 4.38 presents the skin friction plots for the Mach 0.4 sweep. Once again, it can be seen that as angle of attack increases, the change in transition location decreases. One interesting case is the 0.5% FSTI case at 2° AOA. This case behaves very differently to the other cases, and starts undergoing transition before relaminarizing on the bottom surface. On the other hand, the flow at the FSTI value of

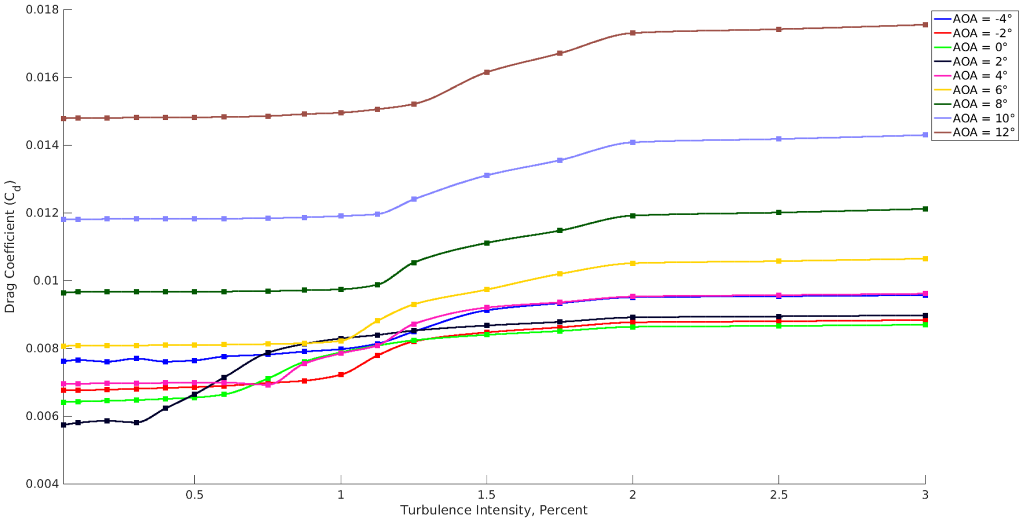

(a) Drag coefficient

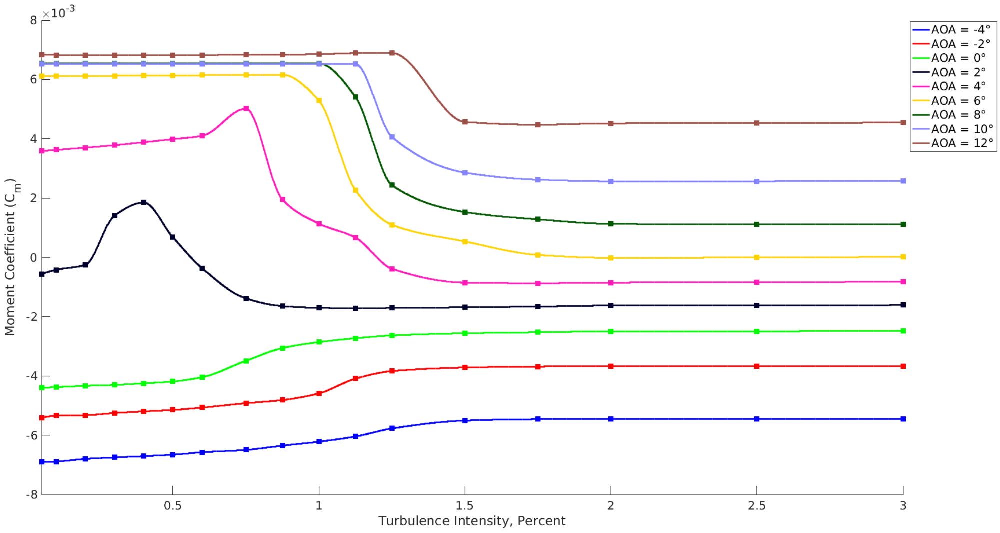

(b) Moment coefficient

Figure 4.34: Parametric Sweep for RC(4)-10 Airfoil at Mach = 0.2, Re = 2×10^6

Mach Number	**Angle of Attack (degrees)**	**FSTI (percent)**
0.2	1	0.5
0.4	1	0.1-0.4
	2	0.3-0.6
0.6	2	0.05

Table 4.3: RC(4)-10 - Peak-to-Peak Averaged Cases

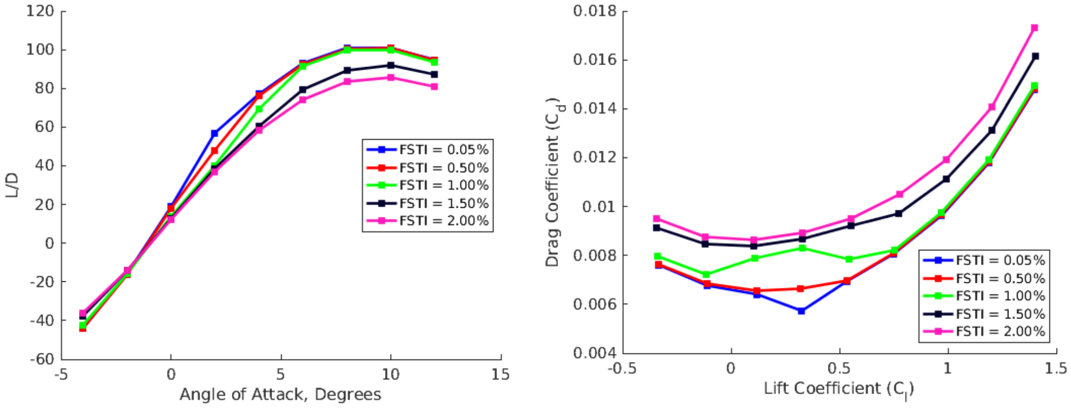

(a) L/D vs Angle of Attack

(b) C_d vs C_l

Figure 4.35: RC(4)-10 Airfoil at Mach = 0.2, Re = 2×10^6

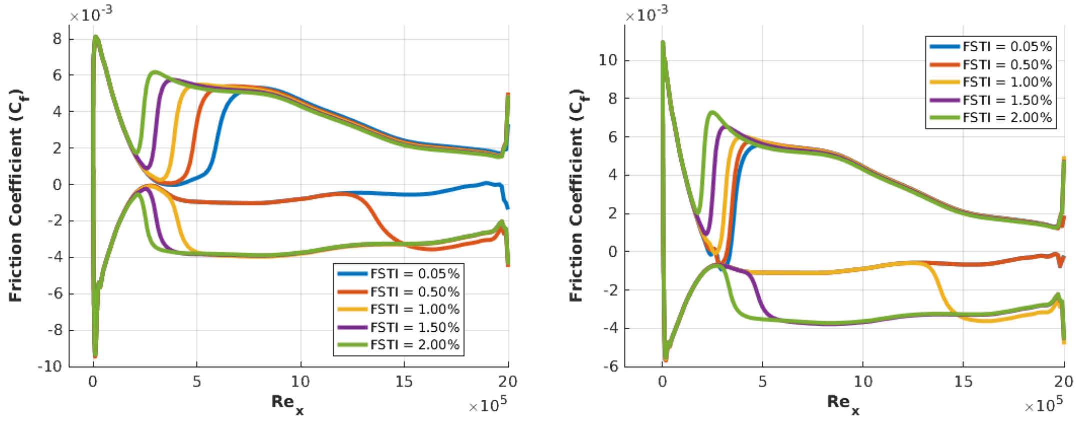

(a) AOA = 2° (b) AOA = 4°

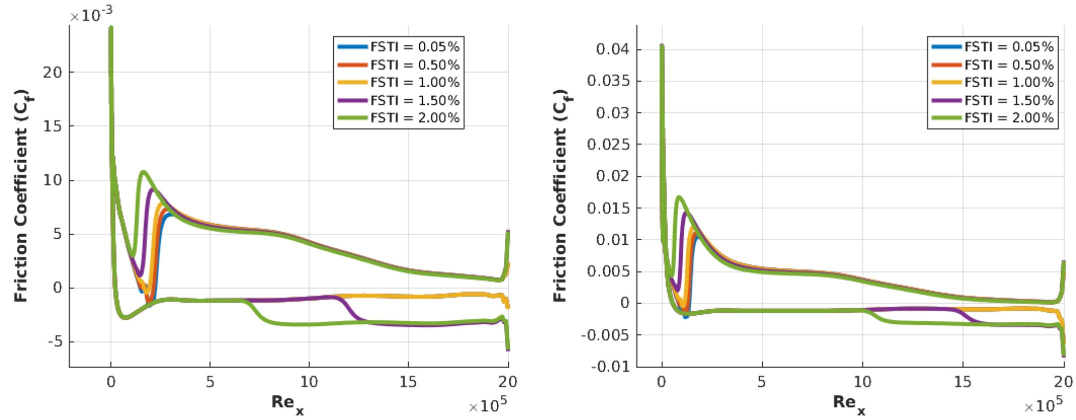

(c) AOA = 8° (d) AOA = 12°

Figure 4.36: Skin Friction Plots for RC(4)-10 - Mach = 0.2, Re = 2×10^6

0.05% remains laminar for the entire bottom surface while the cases with higher values of FSTI undergo transition as usual. This relaminarization phenomenon was not observed for the same conditions for the SC1095 airfoil.

In order to investigate further, the pressure, skin friction, and intermittency were compared, as shown in Fig. 4.39. A plot of the airfoils' geometries is also provided in the figure. The intermittency plot confirms that the bottom surface of the RC(4)-10 relaminarizes in the midst of transition, whereas the SC1095 undergoes full transition. A comparison of the pressure plots reveals that the RC(4)-10 does not have as favorable of a pressure gradient. When comparing the two airfoil profiles, it can be seen that the RC(4)-10 is slightly flatter on the bottom surface when compared to the SC1095. In addition, Fig. 4.1 shows that the RC(4)-10 has extra camber at the leading edge compared to the SC10095. These geometrical features lead to the relaminarization at these freestream conditions.

Mach 0.6

The results for the Mach 0.6 are presented in Fig. 4.40. The results appear to be fairly similar to the previous results. Fluctuations are again present for the moment coefficient at 4° AOA. However, there is no cross-over between 2° and 4° AOA. Fig. 4.41 shows the skin friction plots at 2° and 4° AOA. Both the 0.05% and 0.5% FSTI cases at 2° AOA relaminarize after beginning transition. At 4°, the large change in moment can be explained by the small separation bubble near the bottom of the trailing edge for the 0.5% and 0.05% cases, which is not present at the higher FSTI cases.

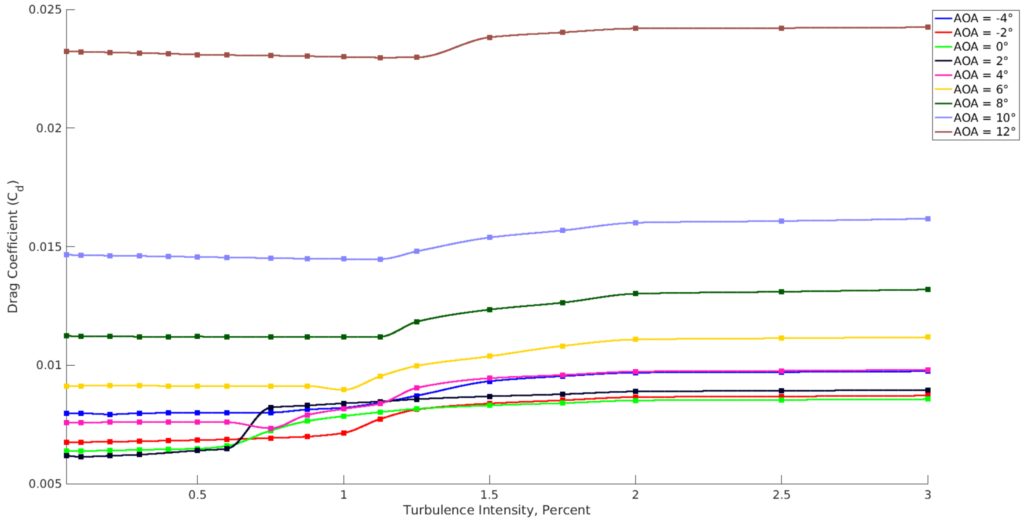

(a) Drag coefficient

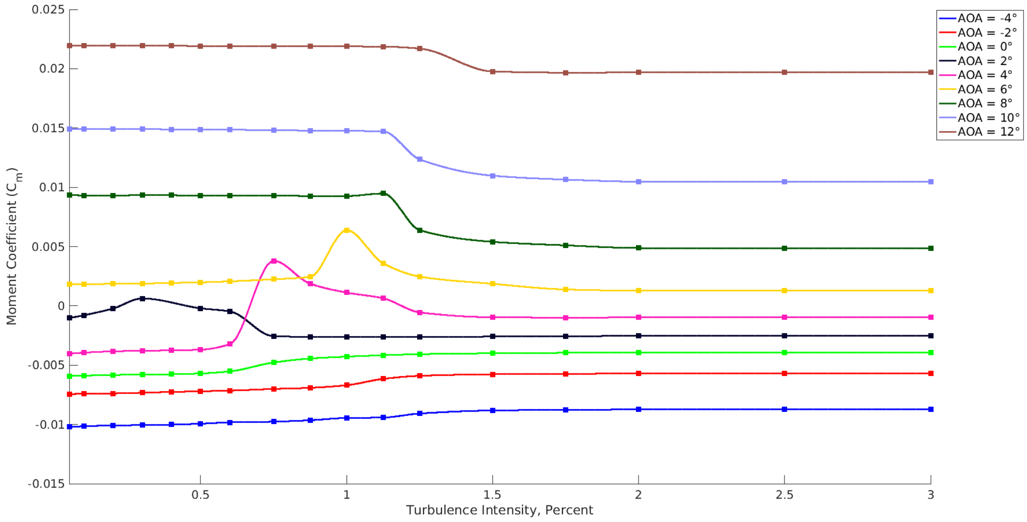

(b) Moment coefficient

Figure 4.37: Parametric Sweep for RC(4)-10 Airfoil at Mach = 0.4, Re = 2×10^6

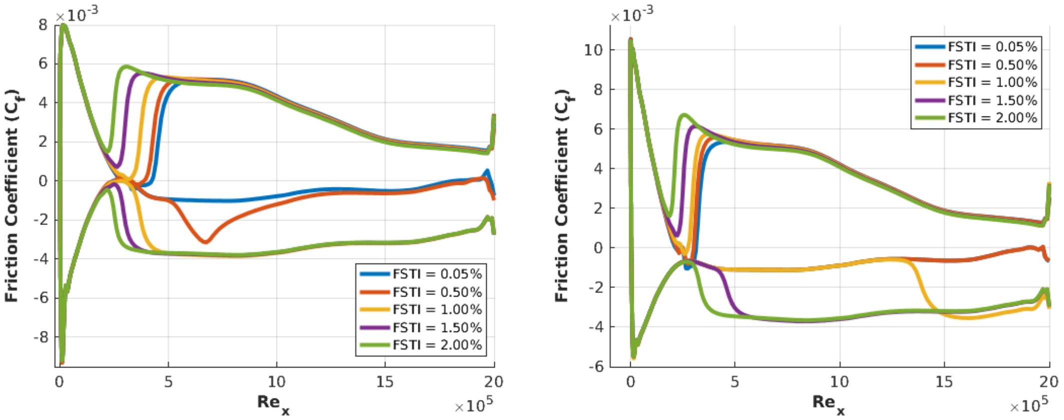

(a) AOA = 2°   (b) AOA = 4°

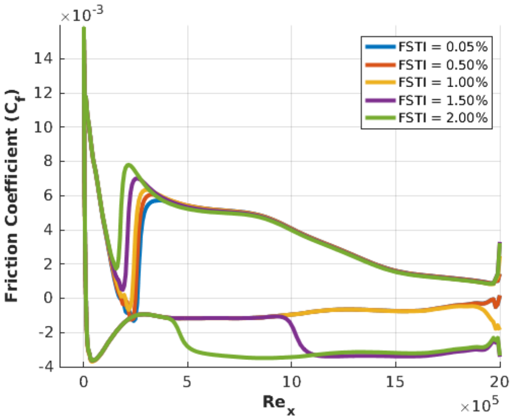

(c) AOA = 6°

Figure 4.38: Skin Friction Plots for RC(4)-10 - Mach = 0.4

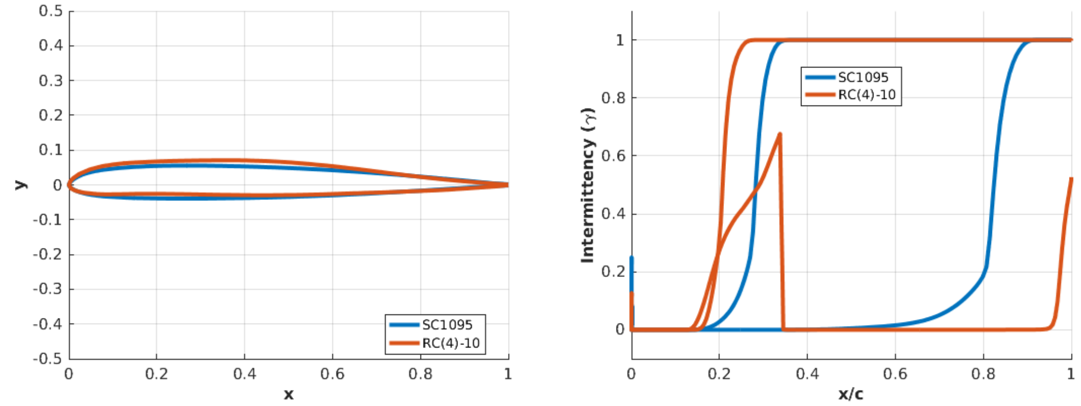

(a) Airfoil Geometry

(b) Intermittency

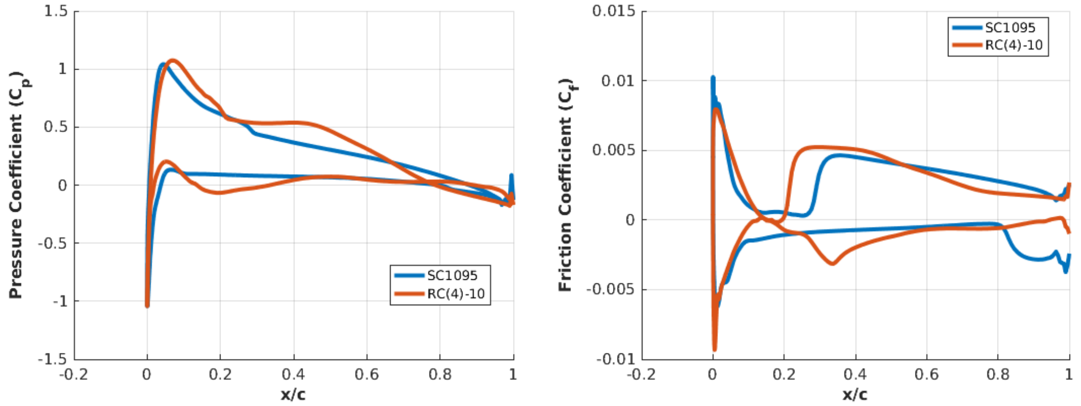

(c) Coefficient of Pressure C_P

(d) Coefficient of Skin Friction C_f

Figure 4.39: Comparison of Plots for SC1095 Airfoil and RC(4)-10, Mach = 0.4, AOA = 2 degrees, FSTI = 0.5%

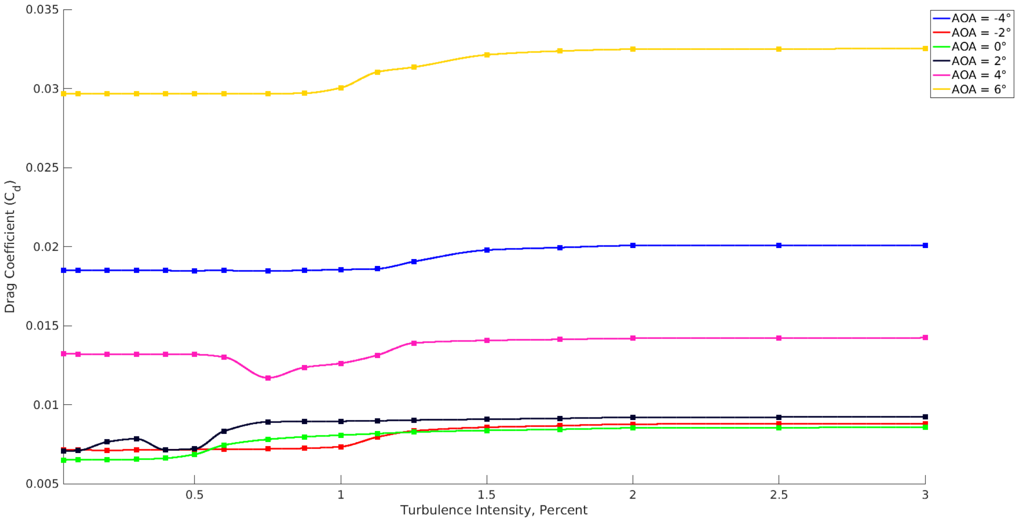

(a) Drag coefficient

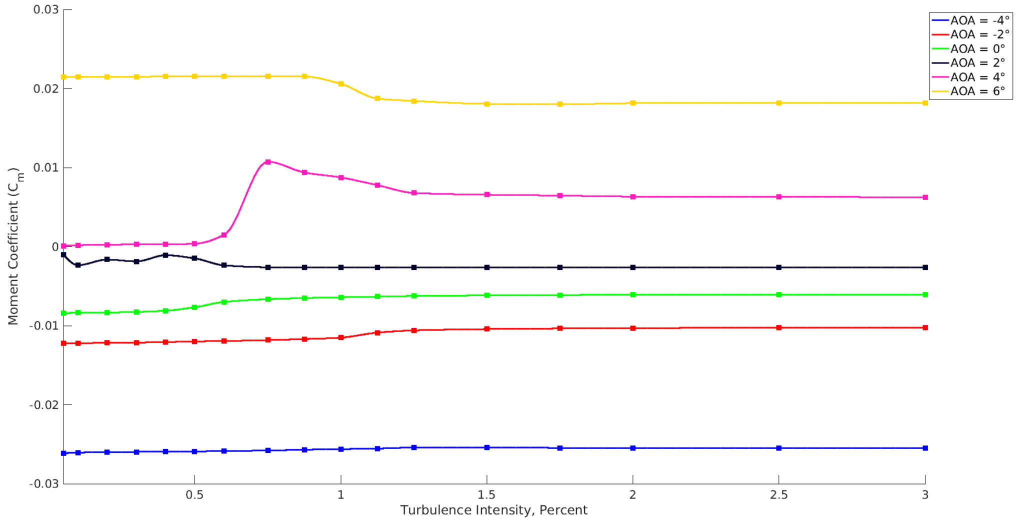

(b) Moment coefficient

Figure 4.40: Parametric Sweep for RC(4)-10 Airfoil at Mach = 0.6, Re = 2×10^6

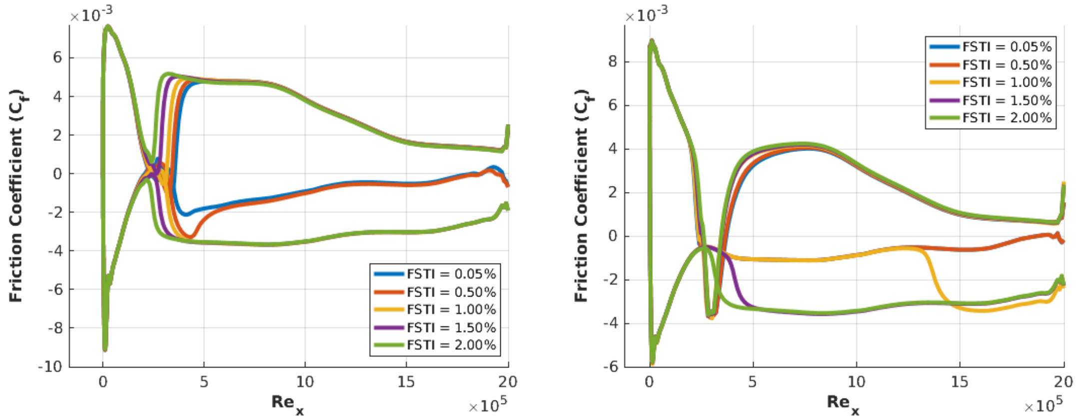

(a) AOA = 2°　　(b) AOA = 4°

Figure 4.41: Skin Friction Plots for RC(4)-10 - Mach = 0.6

Mach 0.7

Fig. 4.42 shows the results of the Mach 0.7 sweep. It is fairly similar to the Mach 0.6 sweep. However, there is one prominent difference. At 6° AOA, the moment is significantly lower, dropping below the 0° AOA case at some points. Fig. 4.43 shows the skin friction plot for the 6° AOA case. One notices that after the shock, the friction remains negative, indicating that the flow never reattaches after the shock. The Mach contour of the 0.5% case, as shown in Fig. 4.44 confirms this.

Mach 0.8

Fig. 4.45 presents the results of the Mach 0.8 sweep. One thing to note is that the -4° AOA case has a very large moment coefficient compared to the other angles of attack. Also, the 6° AOA case has similar behavior to the Mach 0.7 case.

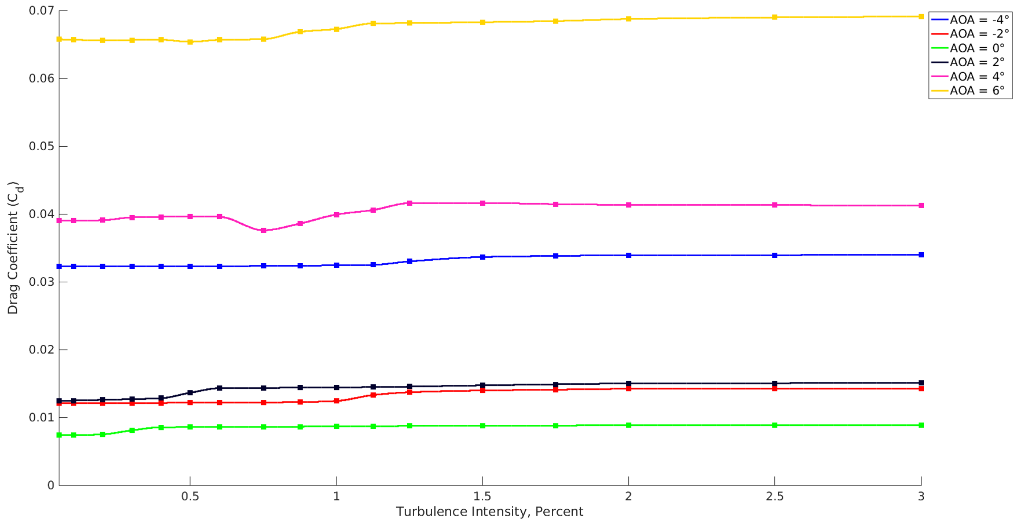

(a) Drag coefficient

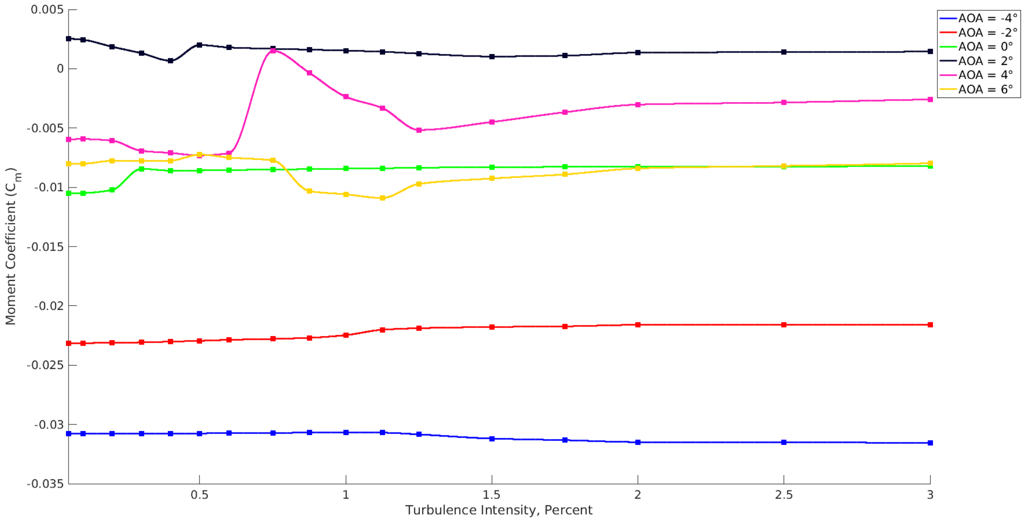

(b) Moment coefficient

Figure 4.42: Parametric Sweep for RC(4)-10 Airfoil at Mach = 0.7, Re = 2×10^6

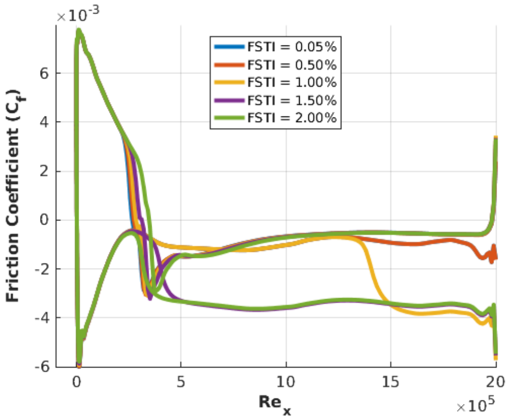

Figure 4.43: Skin Friction Plot for RC(4)-10 - Mach = 0.7 - AOA = 6 degrees

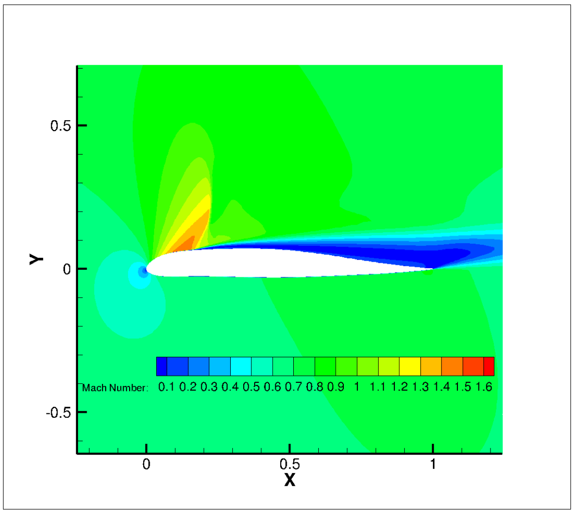

Figure 4.44: Mach Plot for RC(4)-10 - Mach 0.7 - AOA = 6° - FSTI = 0.5%

The pressure, skin friction, and Mach contours are shown for both angles of attack in Fig. 4.46.

The skin friction plot for the -4° AOA case shows that there is separation induced transition on the upper surface for the lower FSTI values. This results in a small increase in suction pressure at the separation bubble, whereas the high FSTI values undergo natural transition and therefore do not have this increase in pressure. The -4° AOA case also shows a strong shock on the bottom surface followed by a region with a thin layer of separation.

For the 6° AOA case, the skin friction plot shows that the flow remains laminar on the bottom surface, even after the shock. This behavior differs greatly from the SC1095 at the same conditions (see Fig. 4.33). Once again, this is due to the difference in the geometries of the airfoils, which were noted earlier.

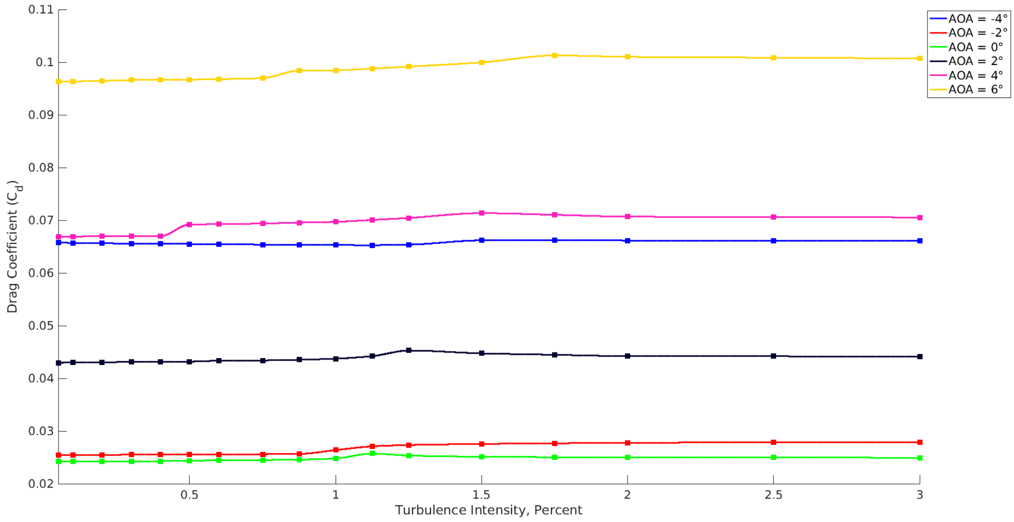

(a) Drag coefficient

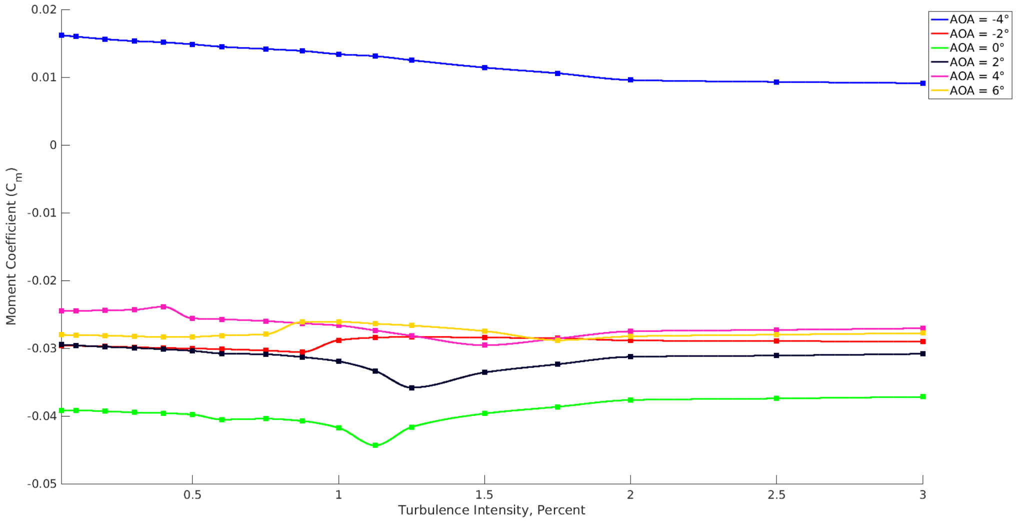

(b) Moment coefficient

Figure 4.45: Parametric Sweep for RC(4)-10 Airfoil at Mach = 0.8, Re = 2×10^6

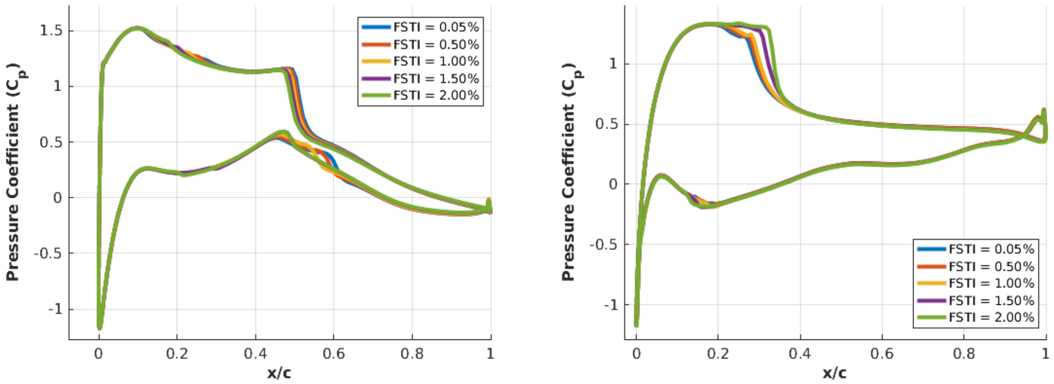

(a) C_P - AOA = -4° (b) C_P - AOA = 6°

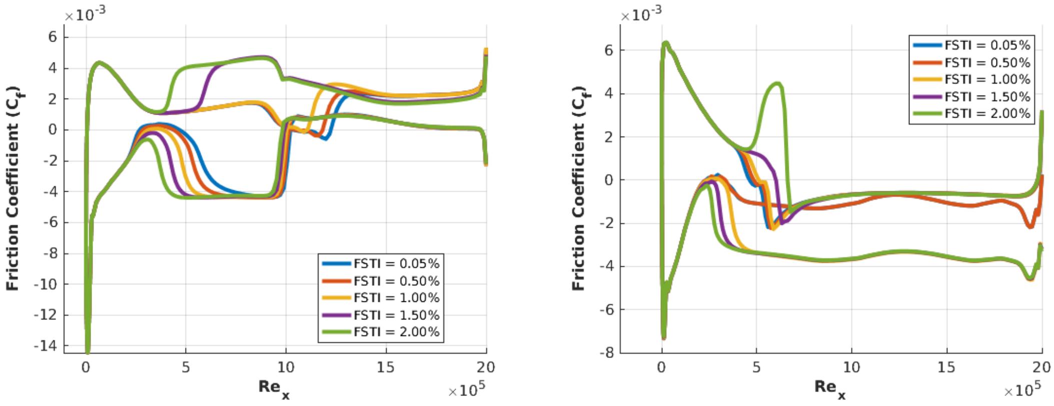

(c) C_f - AOA = -4° (d) C_f - AOA = 6°

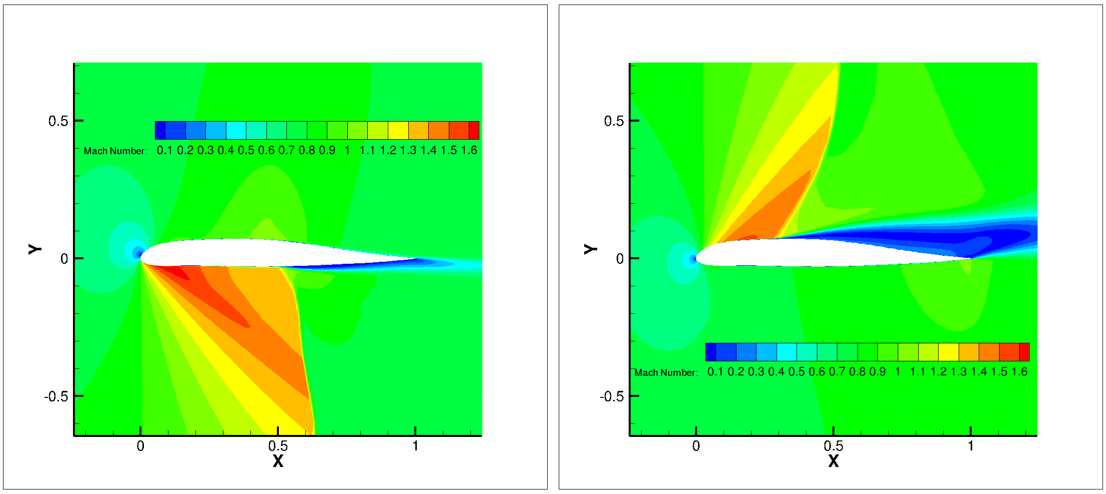

(e) Mach Plot - AOA = -4° - FSTI = 0.5% (f) Mach Plot - AOA = 6° - FSTI = 0.5%

Figure 4.46: Plots for RC(4)-10 Airfoil, Mach = 0.8, Re = 2×10^6

Chapter 5

Uncertainty Quantification Results

This chapter presents the results of the UQ analysis. In order to obtain these results, a Monte Carlo approach was used, as described in section 3.3.1. Results are shown for a mean FSTI of 1% with a standard deviation of 0.3333%, unless stated otherwise. A standard deviation of 0.3333 with a mean of 1.0% means that 99.73% of the input values are expected to be within 0% and 2.0%. The results consist of the expected means and standard deviations for each of the four airfoils for various Mach and Reynolds numbers, as specified in Table 3.1. The standard deviations can be used to determine the sensitivity of the coefficients of lift, drag, and momentum as various parameters are varied. These parameters include FSTI, angle of attack, Mach number, and Reynolds number. An increase in standard deviation indicates that the quantity of interest is more sensitive to uncertainty in FSTI. Trends in standard deviation can simply be explained by examining how the aerodynamic coefficients change as FSTI is varied at each AOA. However, this section explains these trends further by correlating the trends in sensitivity of the quantities of interest to the physics of the airflow.

5.1 S809 Airfoil Results

In order to demonstrate the importance of UQ analysis, Monte Carlo simulations were run for the S809 airfoil at an AOA of 2° with an input FSTI standard deviation of 0.3333%. Two mean input values were used for FSTI: 1.5% and 4.0%. Fig. 5.1 shows the distributions of the input FSTI values as well as the output moment coefficient. As illustrated by the figure, the mean input of 4.0% results in a normal distribution for the moment coefficient. However, when the mean input is changed to 1.5%, the output is not normally distributed. Instead, there is a second peak in the distribution near a pitching moment coefficient value of -0.059. This shows that even with a normally distributed input, the outputs could vary considerably. This also demonstrates why a large number of runs are required for the Monte Carlo simulation to reach statistical convergence. By applying UQ analysis using a Monte Carlo simulation, the true mean and standard deviation can be determined.

Monte Carlo simulations were run for the S809 airfoil for AOA from -4° to 12°, using different mean input FSTI values and different input standard deviations. Fig. 5.2 shows the results for a mean FSTI input of 1.0% and an input standard

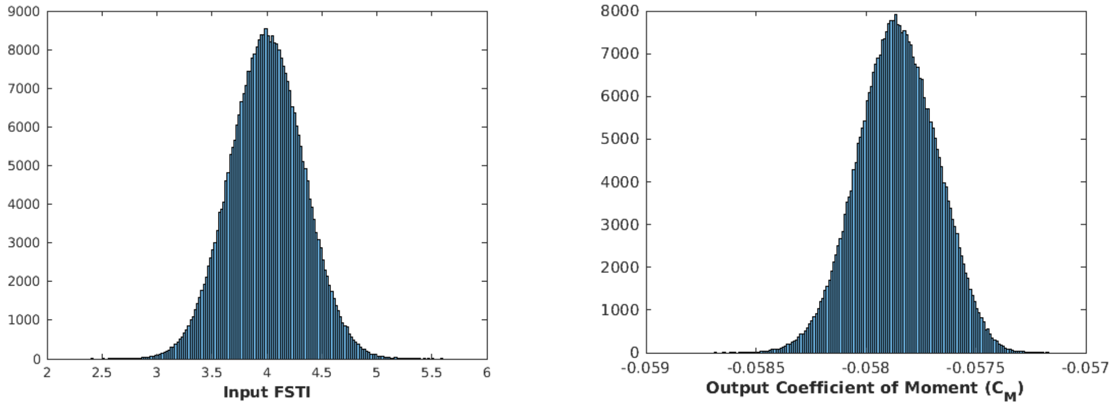

(a) Mean Input FSTI = 4.0%

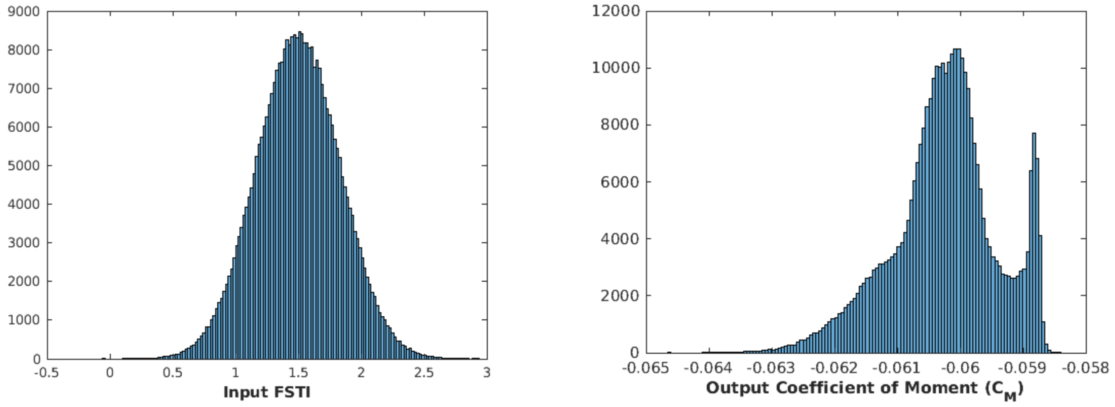

(b) Mean Input FSTI = 1.5%

Figure 5.1: Distributions of Inputs and Outputs for S809 Airfoil at AOA = 2°, Mach = 0.2, Re = 2×10^6, Input $\sigma = 0.3333\%$

deviation of 0.3333%. The error bars on the figure represents the output standard deviation. The values obtained for the discrete 1.0% FSTI value (i.e. without any input uncertainty) are shown for comparison. As shown in the figure, the discrete values are close in value to the values obtained with input uncertainty in FSTI, especially for lift and moment. However, there is a noticeable difference between the discrete values and the values obtained via Monte Carlo for the coefficient of drag, especially at low angles of attack. Note that the standard deviations for lift are also very small. On the other hand, the standard deviations for drag and moment are much larger with respect to the magnitude of the drag and moment coefficient, respectively. Variation in standard deviation values can be observed clearly as AOA increases.

Plots in Fig. 5.3 shows the results of varying the mean of the input FSTI value between 1.0% to 2.0%. This sweep was performed to narrow down the region of interest. In order to better visualize the trends present, the difference between the expected mean of the aerodynamic coefficients with uncertainty in the input FSTI and the discrete value obtained if no uncertainty was present is plotted against AOA in one plot, and the standard deviations are shown in a separate plot. Note that standard deviation is essentially a measure of sensitivity to the input uncertainty in FSTI. Proceeding forward, sensitivity is used interchangeably with the output standard deviation. The plots of the aerodynamic coefficients show that the trends vary as the mean input is increased. As was shown in the parameter sweeps for the S809 airfoil (see Fig. 4.2), the aerodynamic coefficients do not vary linearly with FSTI. Therefore changing the mean input FSTI value results in variation in the difference between the discrete values and mean Monte

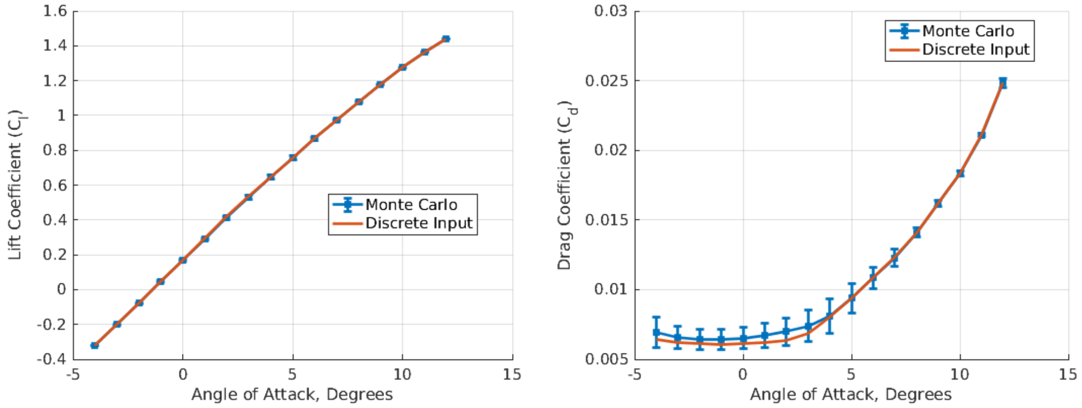

(a) Lift coefficient

(b) Drag coefficient

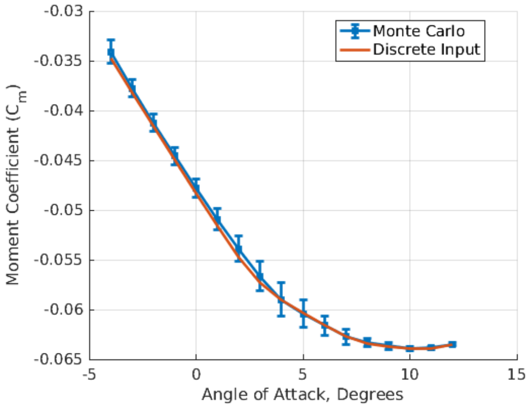

(c) Moment coefficient

Figure 5.2: Monte Carlo Results for S809 Airfoil for Mean Input FSTI 1.0% and Standard Deviation 0.3333%

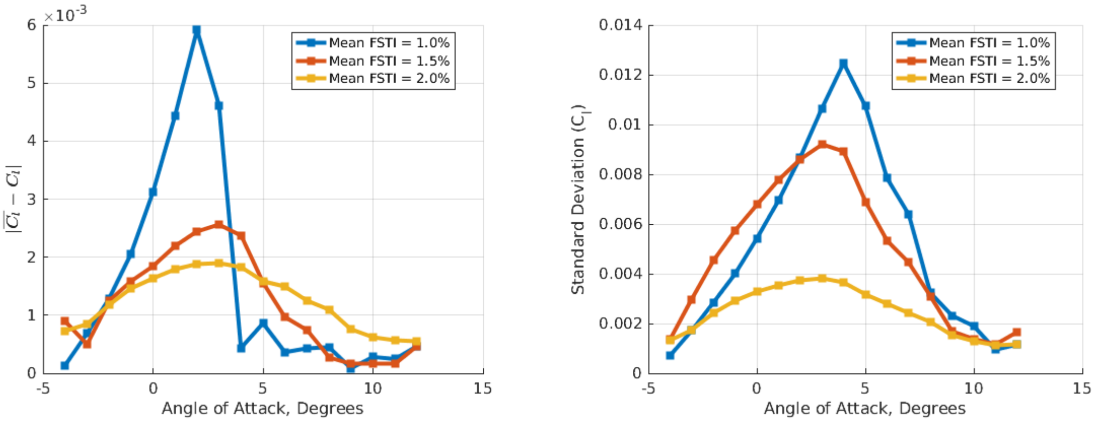

(a) Lift coefficient

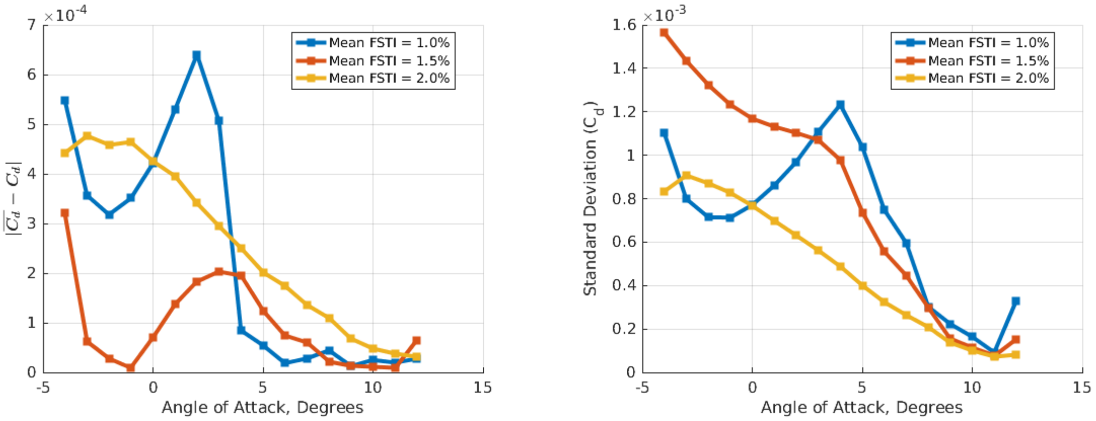

(b) Drag coefficient

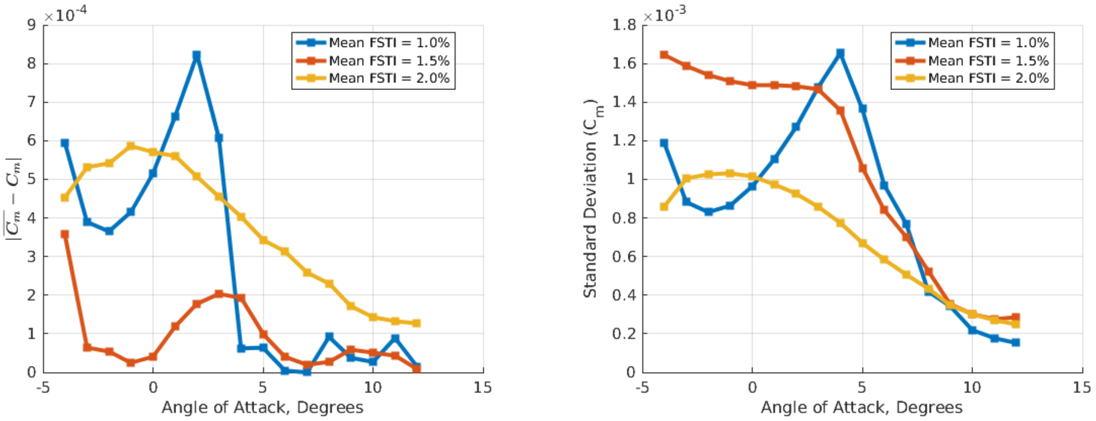

(c) Moment coefficient

Figure 5.3: UQ Results for S809 Airfoil at Mach $= 0.2$, Re $= 2 \times 10^6$, Input $\sigma = 0.3333\%$

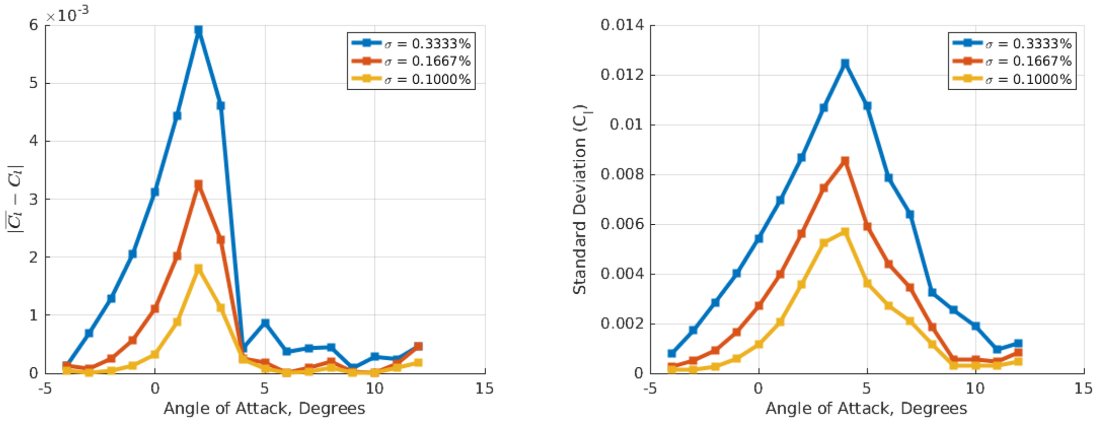

(a) Lift coefficient

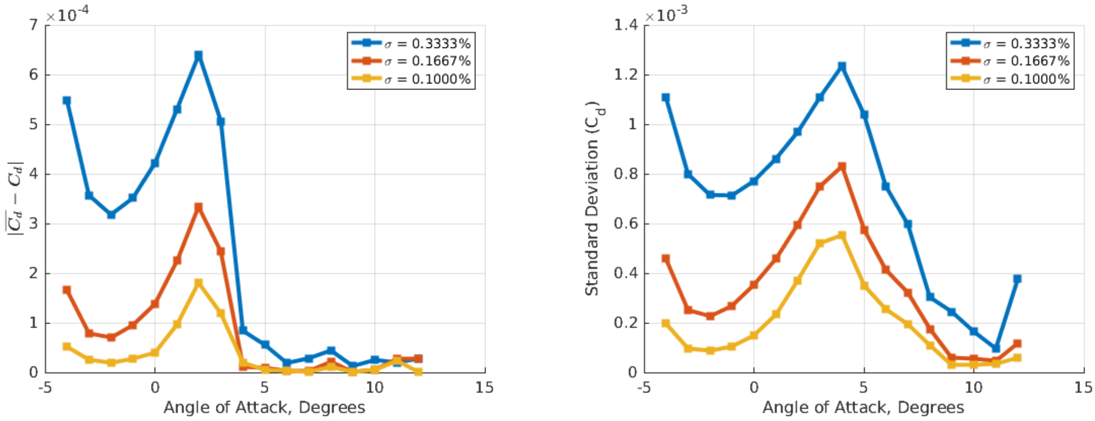

(b) Drag coefficient

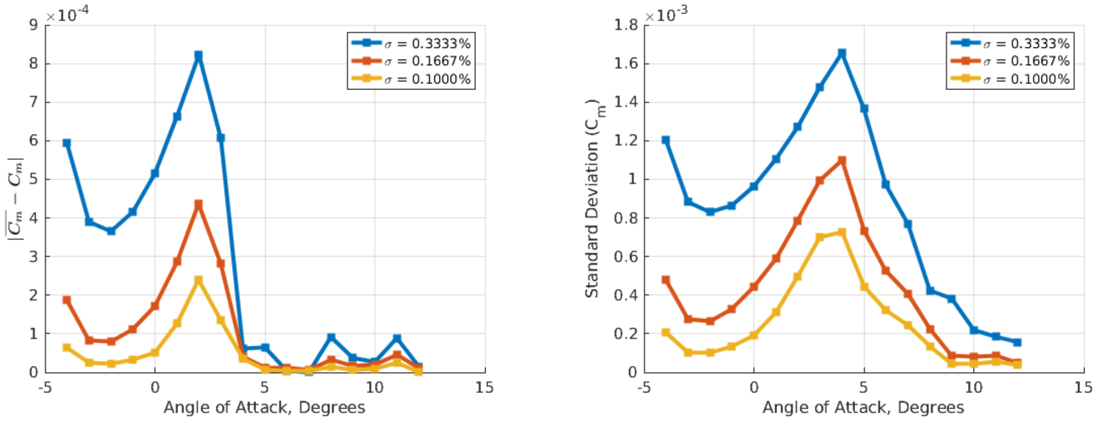

(c) Moment coefficient

Figure 5.4: UQ Results for S809 Airfoil at Mach = 0.2, Re = 2×10^6, Mean FSTI = 1.0%

Carlo outputs.

As can be seen from the standard deviation plots, the sensitivity of the quantities of interest are lower for a mean FSTI of 2.0%. The trends from the S809 parametric sweep support these results (see Fig. 4.2). As FSTI increases above 2.0%, the trends become relatively linear and do not vary as much. Therefore, the sensitivity of the quantities of interest to uncertainty in FSTI decreases for input FSTI values of 2.0% or greater. Fig. 5.3 shows that at low angles of attack (up to 3°), there is greater sensitivity for a mean FSTI of 1.5%, while at moderate to high angles of attack, sensitivity is greater for the mean input 1.0% case.

Fig. 5.4 shows the Monte Carlo results for different input standard deviations. As expected, decreasing the input standard deviation decreases the sensitivity to the aerodynamic coefficients and the difference between the discrete and mean coefficients. An input standard deviation of zero means that there is no uncertainty present. As the input standard deviations approach zero, the expected means approach the discrete values and the standard deviations approach zero. However, it is interesting to note that at high angles of attack (9° or greater), the curves approach a single value. This indicates that at angles of attack of 9° or greater, an increase in the amount of uncertainty in FSTI does not impact the final results as much as it would at angles of attack below 9°.

When comparing the difference in coefficients to the standard deviation plots, note that the trends and peaks do not necessarily correlate. The two types of graphs provide different information. While the difference between the discrete

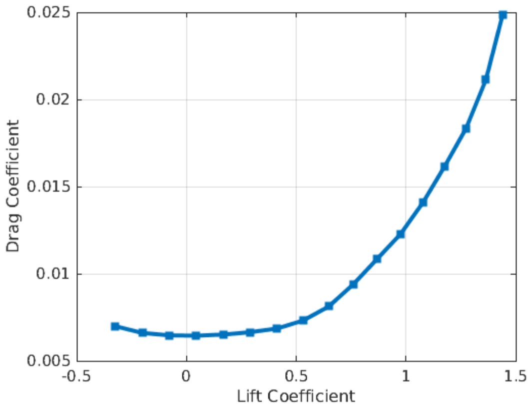

Figure 5.5: Drag Polar for S809 Airfoil at Mach = 0.2, Re = 2×10^6

and mean values may be important for practical application for a specific case, it does not provide any information about the sensitivity of each coefficient to the input uncertainty, which is the focus of the present work. The plots of the difference between the discrete and mean coefficients is therefore omitted when discussing the other three airfoils.

The standard deviations graphs show that all three coefficients have peaks in sensitivity at an angle of attack of 4° and after this point, the standard deviations decrease monotonically. This peak can be attributed to the "drag bucket" for the S809 airfoil (see the drag polar in Fig. 5.5) [50]. At angles of attack below 4°, the flow remains laminar over a significant portion of the leading edge of the airfoil. Since the pressure drag is low at these low angles of attack, the overall drag remains low, creating the laminar drag bucket. For these low angles of attack, small changes in FSTI result in small changes in the drag. At angles of attack above 6°, the pressure drag dominates the drag term and therefore changes in FSTI have relatively small impacts on the quantities of interest. However, for moderate angles of attack (i.e. near 4°-6°), the viscous drag, which is affected by FSTI, is the main contributor to the total drag. Small changes in FSTI therefore result in greater changes in the aerodynamic coefficients for these moderate angles of attack.

5.2 NACA 0012 Airfoil Results: Reynolds Number Sweep

Fig. 5.6 presents the standard deviations of the aerodynamic coefficients for the NACA 0012 airfoil. The Reynolds number has been varied from 500,000 to 4 million. There are a number of conclusions regarding the sensitivity to FSTI that can be reached by examining the trends in the standard deviation graphs. Observe that as the Reynolds number increases, the sensitivity curves change shape. This indicates that there is not a simple relationship between Reynolds number and sensitivity to uncertainty in FSTI. Detailed analysis for each Reynolds number is presented in the following sections.

Re = 500,000

Referring back to Fig. 5.6, a trend can be observed in the standard deviations of lift and moment coefficients for a Reynolds number of 500,000. There is a region of sharp increase in sensitivity between 2° and 5° AOA followed by a region of sharp decrease. This is attributed to the double separation bubble phenomenon mentioned in sec. 4.3. Fig. 5.7 shows skin friction plots for FSTI values of 0.3%,

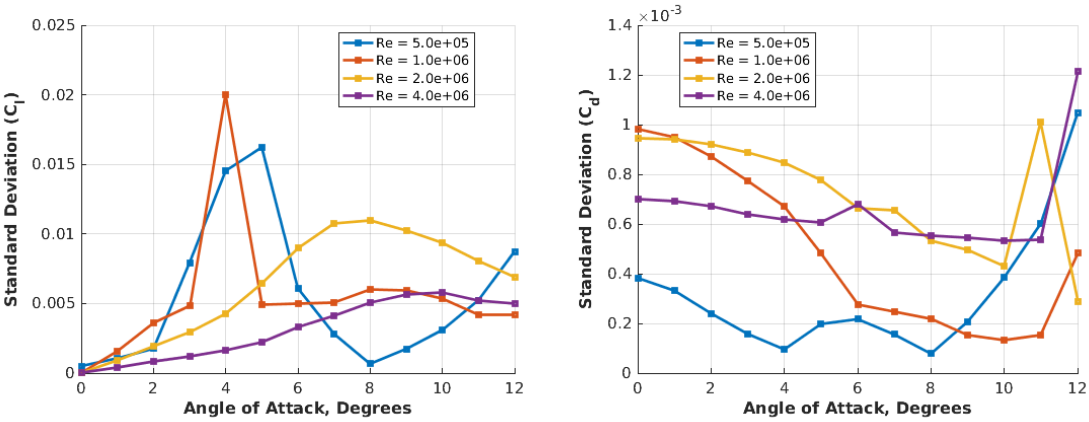

(a) Lift coefficient (b) Drag coefficient

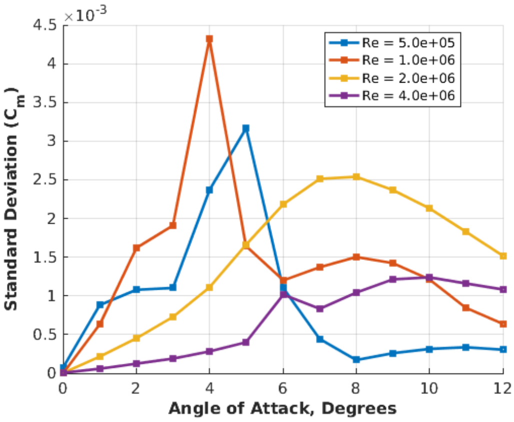

(c) Moment coefficient

Figure 5.6: Standard Deviations for NACA 0012 Airfoil at Mach = 0.2, Mean FSTI = 1%, Input $\sigma = 0.3333\%$

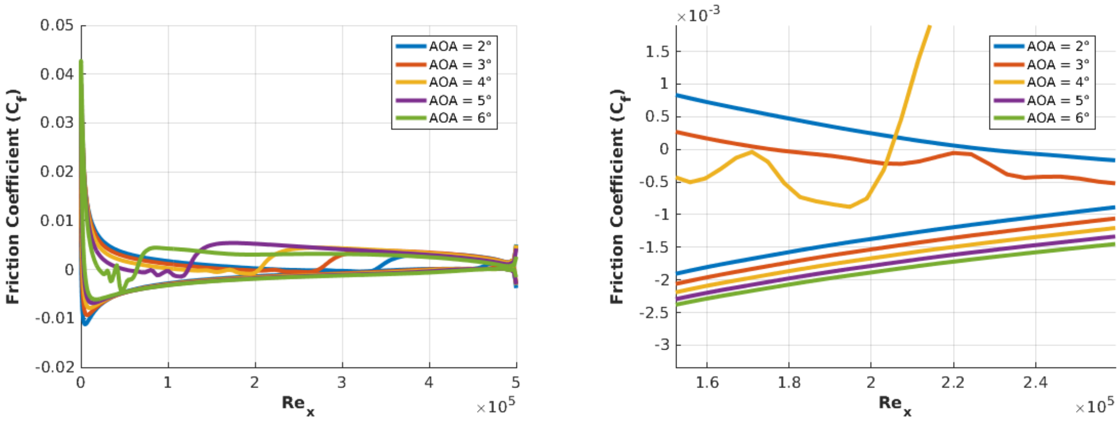

(a) FSTI = 0.3%

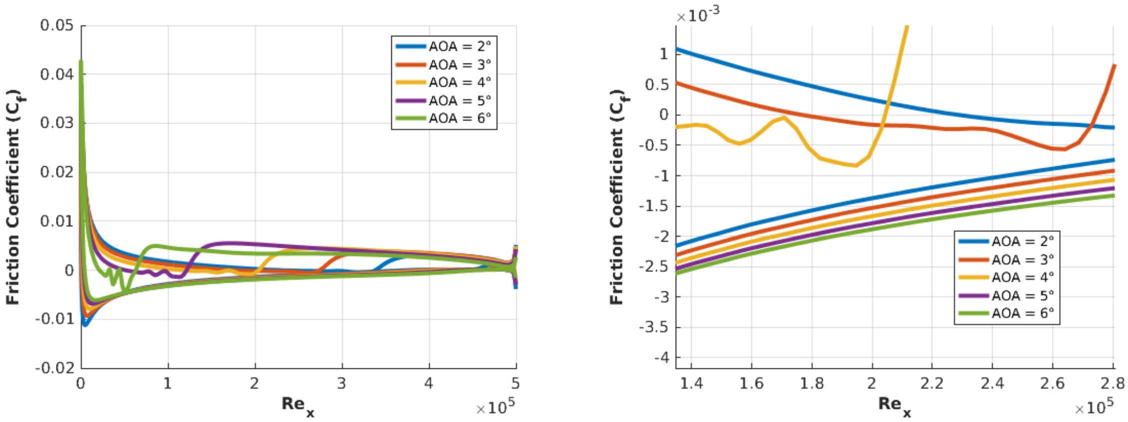

(b) FSTI = 0.4%

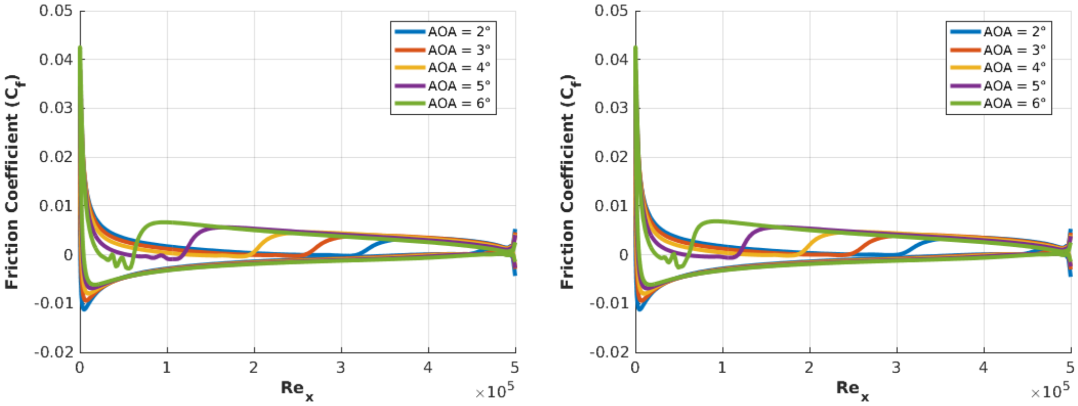

(c) FSTI = 0.875% (d) FSTI = 1.0%

Figure 5.7: Skin Friction Plots for NACA 0012 Airfoil at Mach = 0.2, Re = 500,000

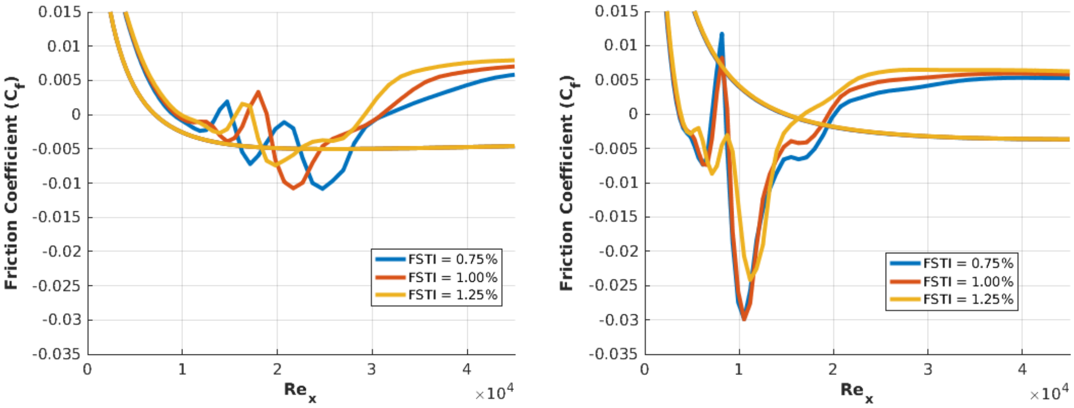

(a) AOA = 8°

(b) AOA = 12°

Figure 5.8: Skin Friction Plots for NACA 0012 Airfoil at Mach = 0.2, Re = 500,000 - AOA 8° versus 12°

0.4%, 0.875%, and 1.0%. Zoomed in portions of the 0.3% and 0.4% are provided to see the separation bubbles more clearly. The 0.3% FSTI case has the double separation bubble on the upper surface from 3° to 5° AOA. However, if the FSTI is slightly increased to 0.4%, then the double separation bubble appears for 4° and 5° AOA. At 3° AOA, there is only a single separation bubble. Likewise, 0.875% and 1.0% FSTI can be compared. At 5° AOA, there is a double separation bubble for 0.875% FSTI case but not for 1.0% FSTI. As mentioned in sec. 4.3, the double separation bubble increases the effective camber of the airfoil, thereby increasing lift and moment. Since these small changes in FSTI at AOA between 2° and 5° can result in the appearance/disappearance of the double separation bubble, the coefficients of lift and moment are more sensitive to uncertainty in FSTI in this AOA range. As FSTI approaches 1.0% (which is the mean input FSTI), the separation bubble appears/disappears near 5° AOA, which is why there is a peak at sensitivity at 5° AOA. The sensitivity decreases at 6° AOA because the double separation bubble is present for all values of FSTI up to 1.5% (not shown in figure).

Fig. 5.8 presents the skin friction plots at 8° and 12° AOA, focusing on the double separation bubble region. This figure explains why the sensitivity of the lift coefficient increases from 8° to 12° AOA. For FSTI values of 0.75% to 1.5% at 8° AOA, the values of the skin friction coefficient at the region of the separation bubble are close. However, at 12° AOA, there is a significant difference between FSTI values of 1.25% and 1.0%. This also explains the peak in sensitivity for the drag coefficient as well.

$\mathbf{Re = 1 \times 10^6}$

When examining the sensitivity curves for a Reynolds number of 1 million in Fig. 5.6, the most distinctive feature is the sharp peak in sensitivity at 4° AOA for lift and moment. Fig. 5.9 shows the skin friction plots from 3° to 5° AOA. At 3° AOA, the 1.0% and 1.25% FSTI cases undergo natural transition on the lower surface. This differs from the 0.75% FSTI case, which has a small separation bubble on the lower surface near the trailing edge. Compare this against the plot for 5° AOA. Here, there is a separation bubble near the trailing edge of the lower surface for both the 0.75% and 1.0% FSTI cases. However, at 4°, the 1.0% FSTI case does not behave like either of the other two FSTI cases at the lower surface. This unique behavior is responsible for the spike in sensitivity for lift and moment at 4° AOA. A small separation bubble at the lower surface near the trailing edge increases the negative effective camber of the airfoil, resulting in significant changes in lift and moment.

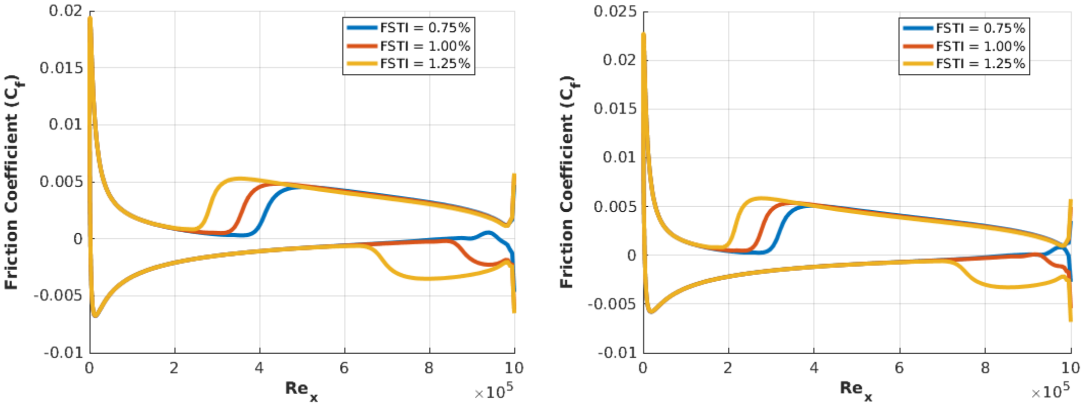

(a) AOA = 3°

(b) AOA = 4°

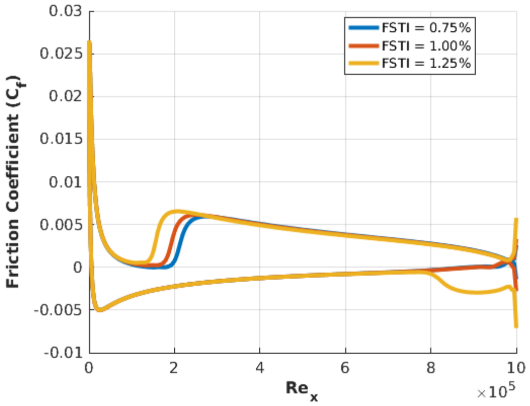

(c) AOA = 5°

Figure 5.9: Skin Friction Plots for NACA 0012 Airfoil at Mach = 0.2, Re = 1×10^6 - AOA 3° - 5°

Re = 2×10^6

In Fig. 5.6, the standard deviation of lift and moment at a Reynolds number of 2 million increase smoothly to a peak at 8° before decreasing gradually. Fig. 5.10 shows the skin friction plots for 4°, 8°, and 12° AOA respectively. When comparing the transition location on the lower surface, note that the transition location has the largest change for the 8° AOA case, which is why the sensitivity peaks at this

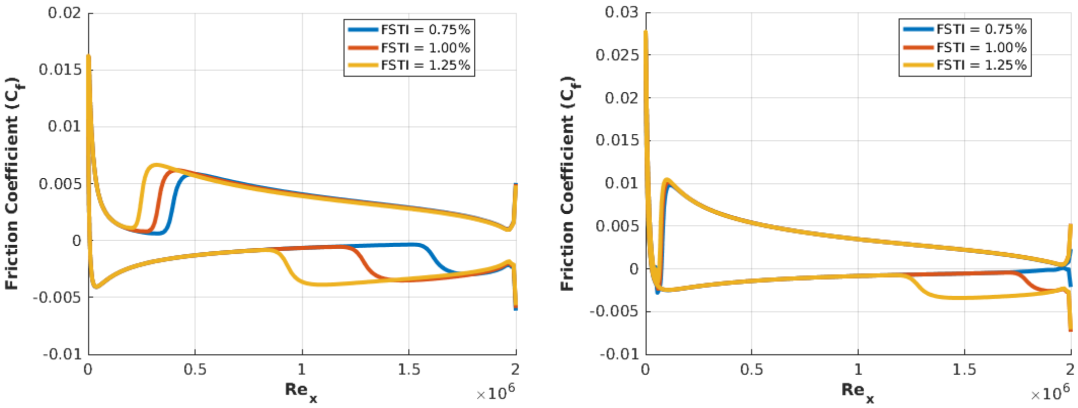

(a) AOA = 4°

(b) AOA = 8°

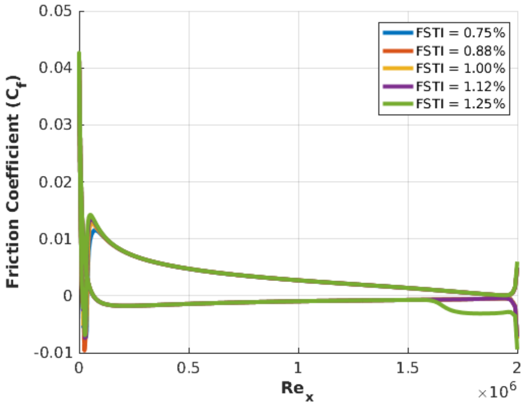

(c) AOA = 12°

Figure 5.10: Skin Friction Plots for NACA 0012 Airfoil at Mach = 0.2, Re = 2×10^6

point for lift and moment.

When examining the sensitivity of the drag coefficient in Fig. 5.6, one notes that the sensitivity generally decreases as AOA increases. However, there is a sharp peak in sensitivity at 11° AOA. Upon examining the pressure and skin friction plots from 10° to 12° AOA (see Fig. 5.11), the cause of this peak is not readily apparent. Further work is needed to explain the reason for this peak.

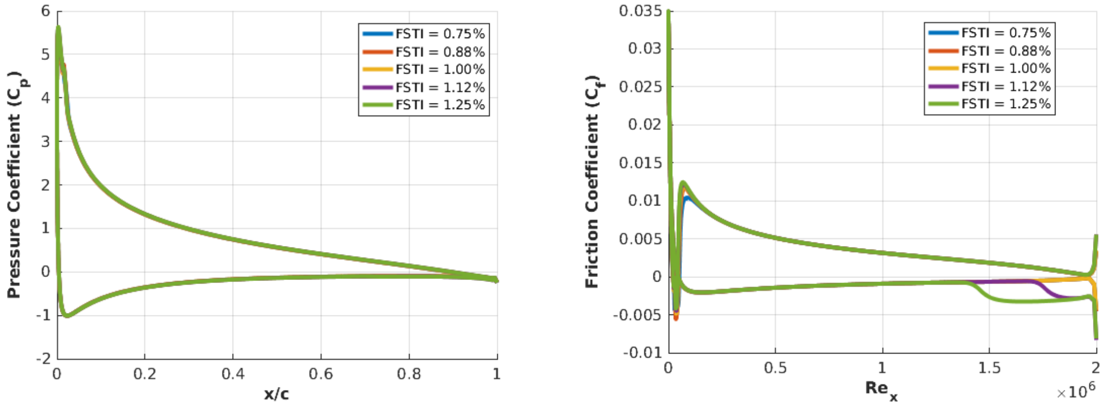

(a) AOA = 10°

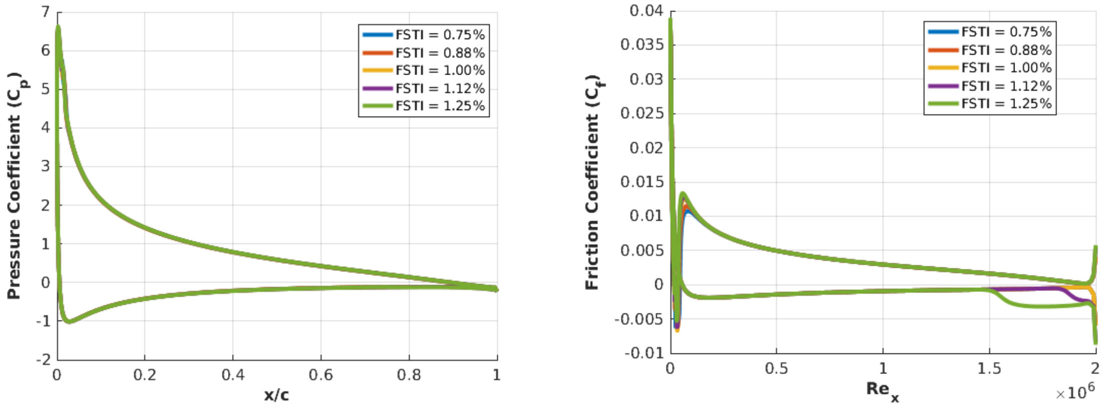

(b) AOA = 11°

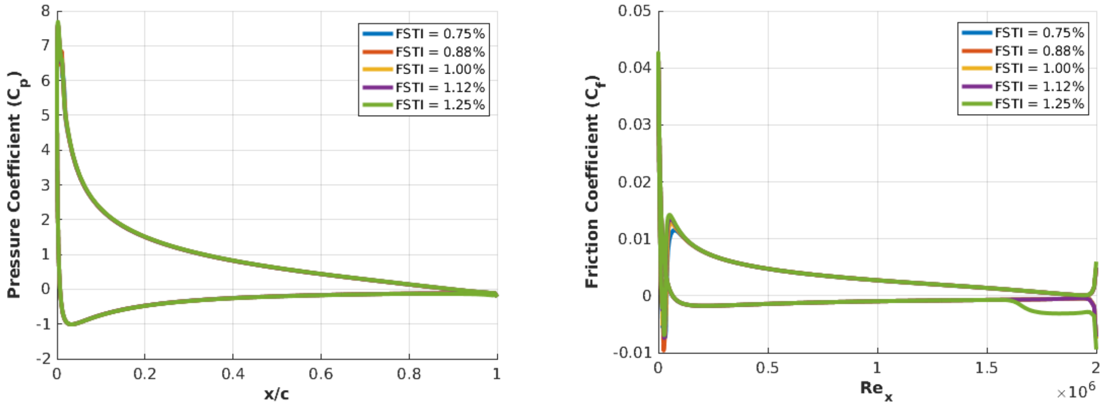

(c) AOA = 12°

Figure 5.11: Pressure and Skin Friction Plots for NACA 0012 Airfoil at Mach = 0.2, Re = 2×10^6

$\mathbf{Re = 4 \times 10^6}$

Going back to Fig. 5.6, one can observe that the standard deviation for lift at a Reynolds number of 4 million is fairly smooth, with a peak near 10° AOA. However, the sensitivity remains almost constant above 10°. Also note that the sensitivity of lift and moment at a Reynolds number of 4 million is lower than the sensitivity at a Reynolds number of 2 million. It is also observed that the sensitivity peaks at 6° AOA for both drag and moment. Fig. 5.12 shows the skin friction plots at 5°, 6°, 7°, 10°, and 12° AOA. However, the friction plots do not provide a clear explanation for the trends in aerodynamic coefficients; more work is required to determine the actual cause.

5.3 SC1095 Airfoil Results: Mach Number Sweep

Fig. 5.13 presents the standard deviations of the aerodynamic coefficients. The standard deviations correlate to the sensitivity of each coefficient to the uncertainty in FSTI. It can be observed from the figure that standard deviation curves for Mach 0.2, 0.4, and 0.6 follow similar trends for all three aerodynamic coefficients, with the exception of AOA between 3° and 6°. The similarities at these Mach numbers is due to the incompressibility of air at subsonic speeds. At Mach 0.7 and 0.8, transonic flow begins to appear, and compressibility effects change the trends in sensitivity.

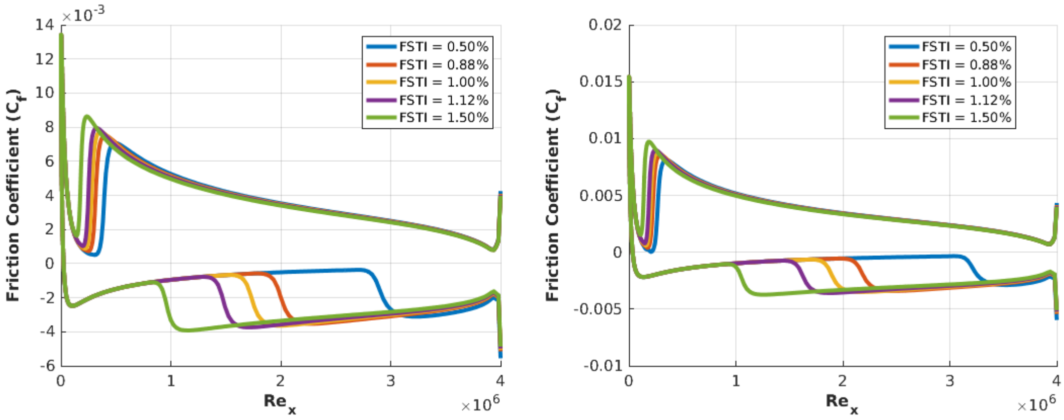

(a) AOA = 5°

(b) AOA = 6°

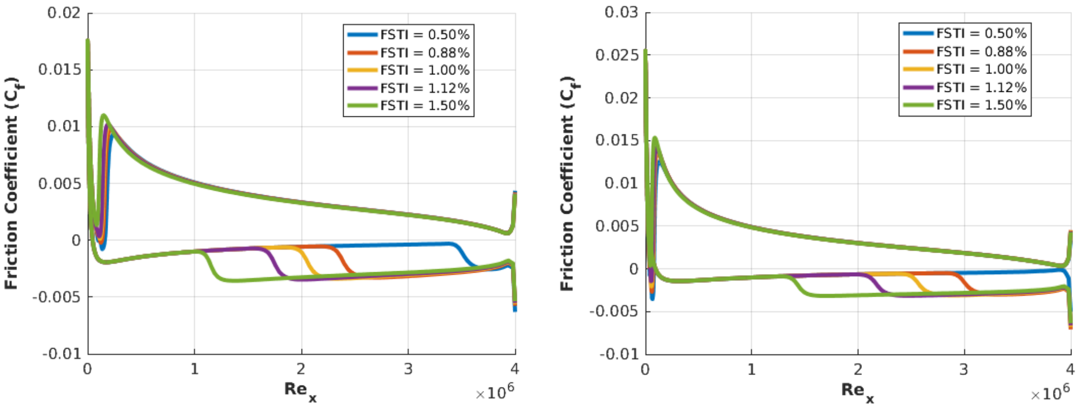

(c) AOA = 7°

(d) AOA = 10°

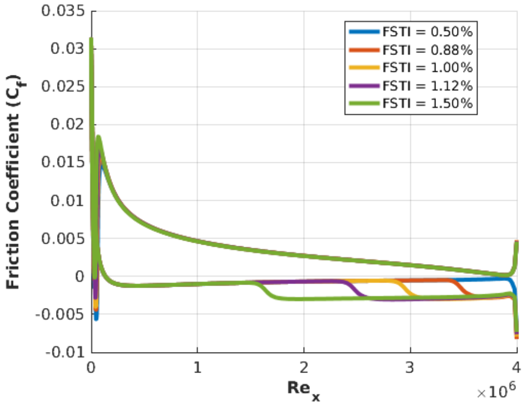

(e) AOA = 12°

Figure 5.12: Skin Friction Plots for NACA 0012 Airfoil at Mach = 0.2, Re = 4×10^6

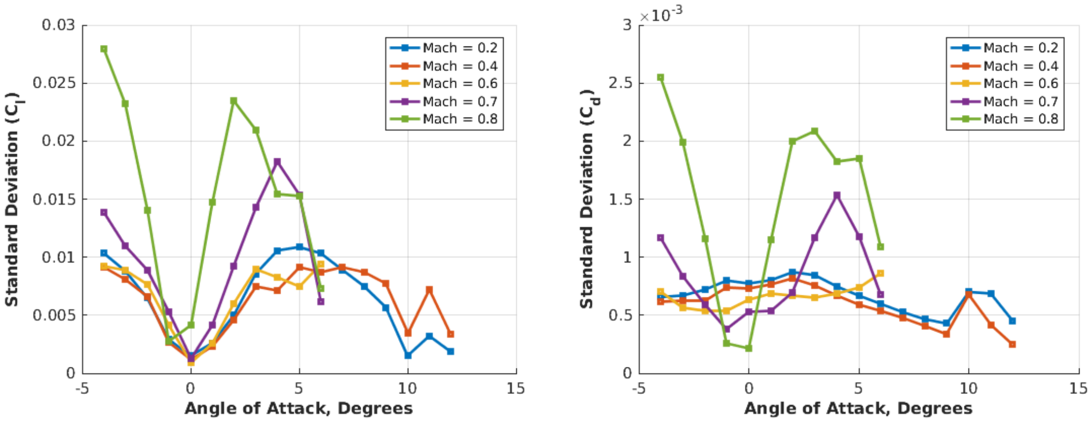

(a) Lift coefficient (b) Drag coefficient

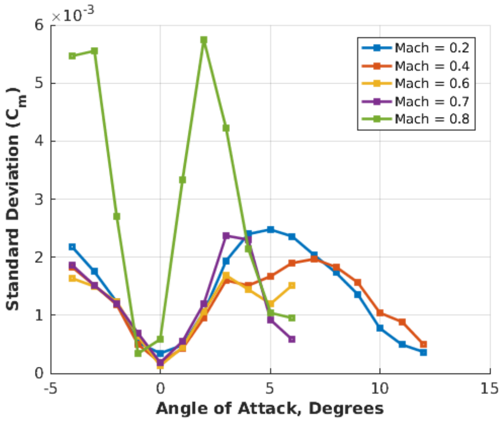

(c) Moment coefficient

Figure 5.13: UQ Results for SC1095 Airfoil at Re $= 2 \times 10^6$, Mean FSTI $= 1\%$, Input $\sigma = 0.3333\%$

Mach 0.2, 0.4, and 0.6

For Mach 0.2 and 0.4, the flow remains subsonic and the aerodynamic coefficients follow similar trends. At Mach 0.6, the flow is subsonic at AOAs below 3°. However, there are some differences between Mach 0.2, 0.4, and 0.6 between 3° and 6°. In this region, lift and moment are significantly more sensitive to FSTI uncertainty for Mach 0.2 compared to Mach 0.4 and 0.6. Also, the sensitivity of drag decreases over AOA 3° to 6° for Mach 0.2 and 0.4, but increases for Mach 0.6. Referring to Fig. 5.14, which depicts the Mach contours for AOA 6° at Mach 0.4 and 0.6, one can see that at Mach 0.4, there is no observable differences in the Mach contour plots between FSTI 0.5% and 2.0%. On the other hand, for Mach 0.6, the shock is observed to be stronger at FSTI 2.0% compared to 0.5%. The increase in drag sensitivity for Mach 0.6 between 3° and 6° can be attributed to this increase in shock strength, which would increase the drag over the airfoil.

Mach 0.7 and 0.8

Mach 0.7 and 0.8 differ in behavior compared to Mach 0.2 to 0.6. At almost all AOAs, the sensitivity of lift and drag are greater for Mach 0.7 and 0.8 than for Mach 0.2 to 0.6. For Mach 0.7, the sensitivity for lift and drag increases sharply as AOA increases between 0° and 4° AOA before decreasing sharply. For Mach 0.8, the sharp increase in sensitivity occurs at 2° AOA.

Fig. 5.15 shows the skin friction plots for Mach 0.7 at 2°, 4°, and 6°; and for Mach 0.8 at 0°, 2°, and 6° AOA. For Mach 0.7 at an AOA of 2°, all the cases

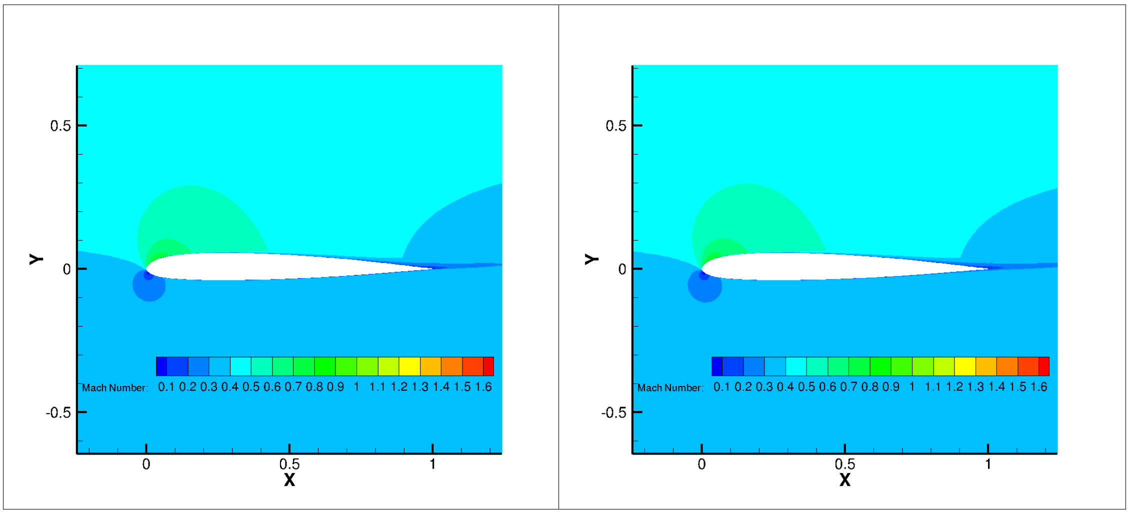

(a) Mach = 0.4, FSTI = 0.5%

(b) Mach = 0.4, FSTI = 2.0%

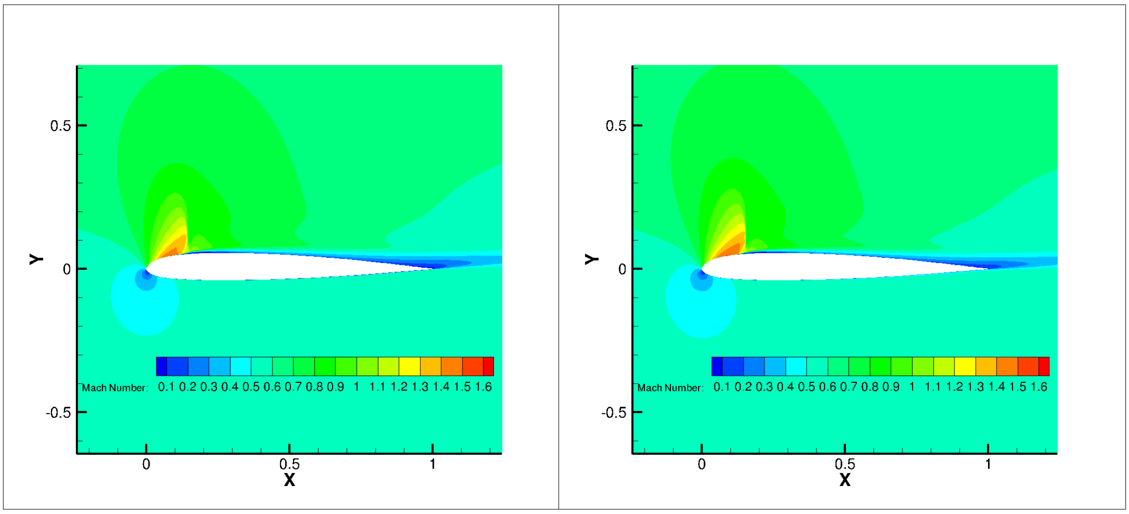

(c) Mach = 0.6, FSTI = 0.5%

(d) Mach = 0.6, FSTI = 2.0%

Figure 5.14: Mach Contours for SC1095 Airfoil at 6° AOA, Re $= 2 \times 10^6$

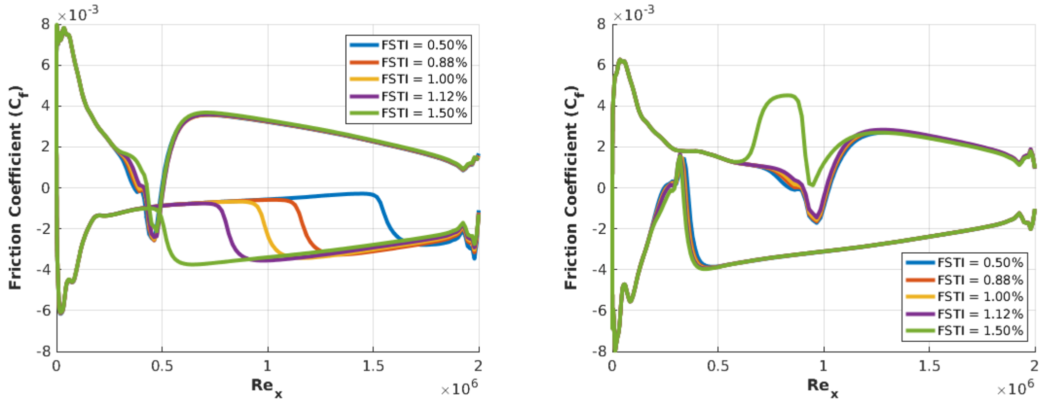

(a) Mach 0.7 - AOA = 2° (b) Mach 0.8 - AOA = 0°

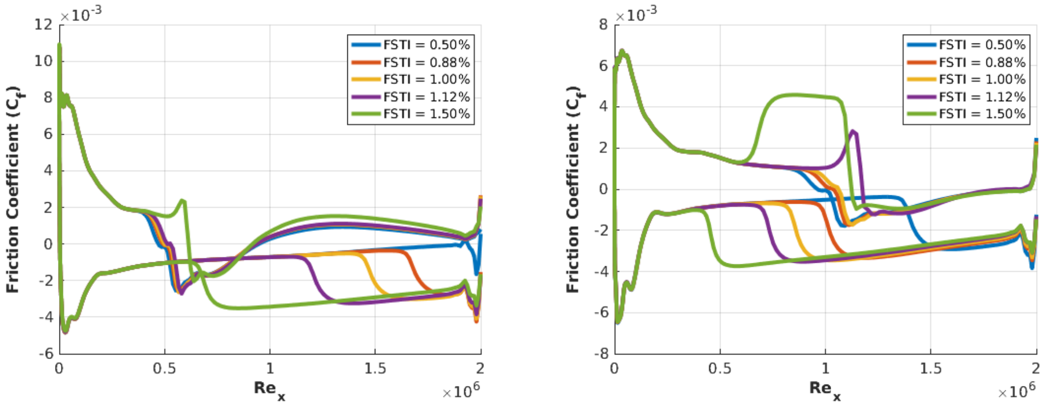

(c) Mach 0.7 - AOA = 4° (d) Mach 0.8 - AOA = 2°

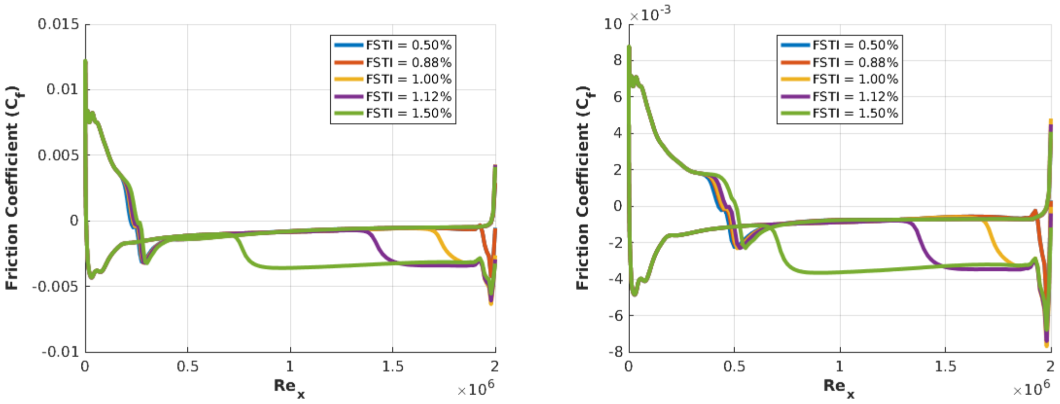

(e) Mach 0.7 - AOA = 6° (f) Mach 0.8 - AOA = 6°

Figure 5.15: Skin Friction Plots for SC1095 Airfoil, Mach = 0.7 - 0.8, Re = 2×10^6

undergo transition after the shock. For Mach 0.8 at an AOA of 0°, all of the cases undergo transition after the shock except the 1.5% FSTI case, which transitions completely before the shock. For Mach 0.7 at an AOA of 4° and Mach 0.8 at an AOA of 2°, there is one FSTI case which is mid-way through transition at the shock. For Mach 0.7, this is the 1.5% FSTI case; for Mach 0.8, this is the 1.12% case. Note that for both cases where transition is occurring at the shock, the transition location differs from all of the other FSTI cases. Since these FSTI values are relatively close to 1.0%, this results in an increase in sensitivity for lift and drag for a mean input of 1.0%. As the AOA increases, the sensitivity decreases once again, as all of the FSTI cases exhibit the same behavior, as shown in the Mach 0.7 and 0.8 plots at an AOA of 6°.

5.4 RC(4)-10 Airfoil Results: Mach Number Sweep

Fig. 5.16 presents the standard deviations of the aerodynamic coefficients for the RC(4)-10. The Mach number was varied from 0.2 to 0.8. Both the Mach 0.2 and 0.4 standard deviation curves follow similar trends. Similar to the SC1095 cases, at these Mach numbers, the flow remains subsonic. However, the sensitivity results for Mach 0.6 to Mach 0.8 become more erratic, once compressibility effects come into effect. Compare the sensitivity curves for the RC(4)-10 against the SC1095 sensitivity plots in Fig. 5.13. While the trends are similar for Mach 0.2 and 0.4, the sensitivities are very different for Mach 0.7 and 0.8.

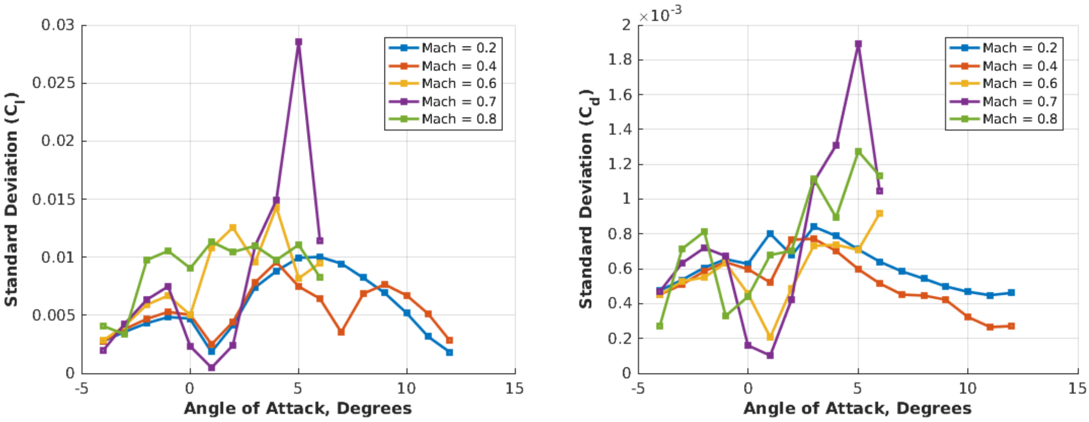

(a) Lift coefficient
(b) Drag coefficient

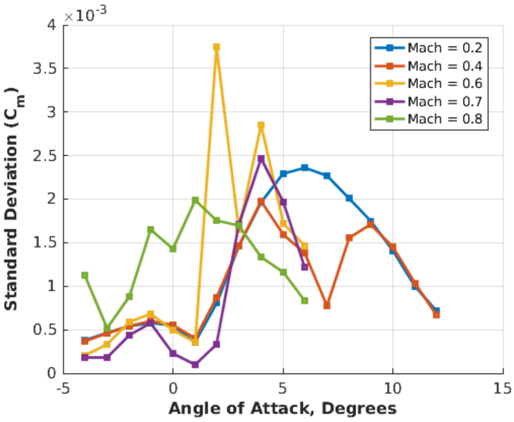

(c) Moment coefficient

Figure 5.16: UQ Results for RC(4)-10 Airfoil at Re $= 2 \times 10^6$, Mean FSTI = 1%, Input $\sigma = 0.3333\%$

Mach 0.2 and 0.4

The sensitivities for Mach 0.2 and 0.4 are very close to each other for all three coefficients, with a few exceptions:

- Lift and moment coefficients between 5° and 8° AOA
- Drag coefficient at 1° AOA

Fig. 5.17 presents skin friction plots for 1°, 6°, and 7° AOA for both Mach 0.2 and 0.4. Comparing the 1° AOA plots, one can see that at Mach 0.2 for an FSTI value of 0.5%, the flow relaminarizes on the lower surface but does not relaminarize at the same conditions for Mach 0.4. Since laminar flow results in significantly less drag than turbulent flow, the drag coefficient is much more sensitive to uncertainty in FSTI at Mach 0.2 than at 0.4. However, when examining the skin friction plots for AOA 6° and 7°, the graphs do not differ significantly between Mach 0.2 and 0.4. Additional investigation is required to determine why there is a difference in the sensitivity of lift and moment between Mach 0.2 and 0.4 for AOA 5° to 8°.

Mach 0.6 to 0.8

When examining Fig. 5.16, one can observe that the Mach 0.6 to 0.8 sensitivity curves are not as smooth as the Mach 0.2 and 0.4 curves; rather, they are characterized by jumps and fluctuations in sensitivity as AOA varies. Seven points of interest have been identified to explore further:

1. Mach 0.6: Peak in sensitivity of the moment coefficient at AOA of 2°.

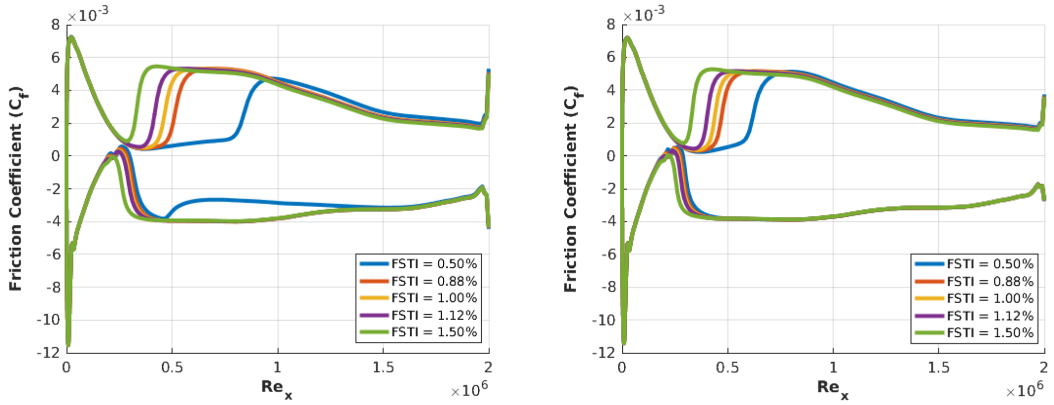

(a) Mach 0.2 - AOA = 1°

(b) Mach 0.4 - AOA = 1°

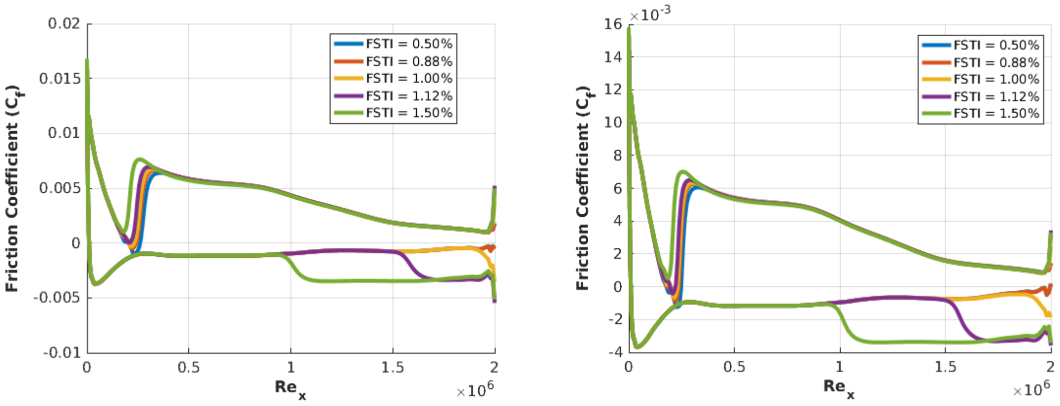

(c) Mach 0.2 - AOA = 6°

(d) Mach 0.4 - AOA = 6°

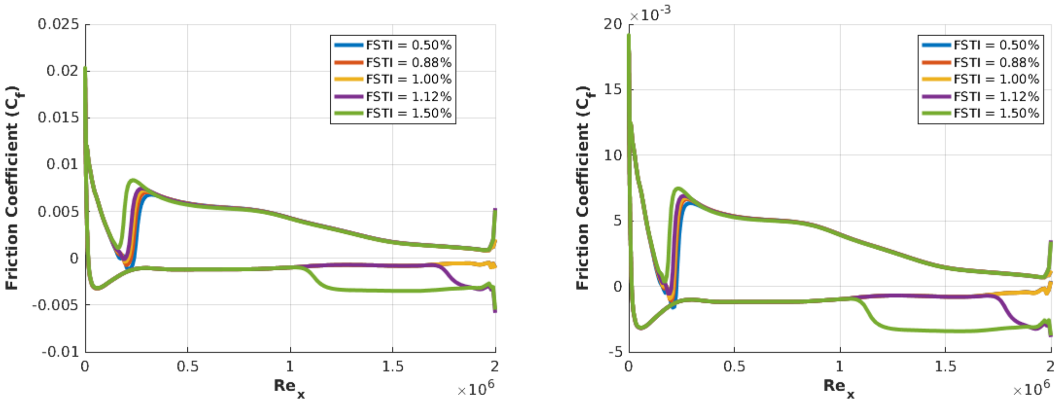

(e) Mach 0.2 - AOA = 7°

(f) Mach 0.4 - AOA = 7°

Figure 5.17: Skin Friction Plots for RC(4)-10 Airfoil, Mach = 0.2 - 0.4, Re = 2×10^6

2. Mach 0.6: Minimum sensitivity of the moment coefficient at AOA of 3°.
3. Mach 0.6: Peak in sensitivity of the moment coefficient at AOA of 4°.
4. Mach 0.7: Peak in sensitivity of the moment coefficient at AOA of 4°.
5. Mach 0.7: Peaks in sensitivity of the lift and drag coefficient at AOA of 5°.
6. Mach 0.8: Peak in sensitivity of the moment coefficient at AOA of 1°.
7. Mach 0.8: Peak in sensitivity of the drag coefficient at AOA of 5°.

Fig. 5.18 provides the skin friction plots for the three Mach 0.6 cases mentioned above, while Fig. 5.19 presents the skin friction plots for the Mach 0.7 and 0.8 cases. For the Mach 0.6 cases, at an AOA of 2° and an FSTI of 0.5%, the flow relaminarizes. This results in a peak in sensitivity for the moment coefficient. At AOA 3° and 4°, this relaminarization is not present. However, at AOA 4°, a separation bubble forms on the lower surface near the trailing edge for the FSTI 0.5% and 0.75% cases. At AOA 3°, the separation bubble only forms on the 0.5%. Since the mean input is 1.0%, the change in the transition mode between 0.75% and 1.0% FSTI results in a peak in the moment coefficient sensitivity.

Fig. 5.19 shows the skin friction plots for the four Mach 0.7 and 0.8 cases of interest. For Mach 0.7 at an AOA of 4°, both the upper and lower surfaces show different methods of transition. On the upper surface, at FSTI values of 0.5% to 1.0%, the flow transitions after the shock. At 1.25% FSTI, the flow transitions at the shock, while at 1.5% FSTI, the flow transitions before the shock. On the lower surface, at 0.5% FSTI, there is a small separation bubble at the trailing edge. For the FSTI values greater than 0.5%, the flow undergoes natural transition. The small changes in FSTI result in completely different methods of transition on both the upper and lower surface, resulting in a peak in sensitivity for the moment coefficient for Mach 0.7.

The Mach 0.7 case at an AOA of 5° also features different methods of transition as FSTI varies. On the upper surface, the flow transitions at the shock at an FSTI of 1.5% and transitions after the shock for all the other FSTI values. However, unlike the 4° AOA case, there is no separation bubble on the lower surface. On the lower surface, the 0.5% and 0.75% cases remain laminar, while the 1.0%, 1.25%, and 1.5% cases undergo natural transition. The moment sensitivity decreases due to the absence of the separation bubble on the lower surface, but the changes in the transition location on the lower surface result in a peak in sensitivity for both lift and drag.

For the Mach 0.8 case, at an AOA of 1°, the flow on the upper surface transitions before the shock for FSTI values of 1.25% and 1.5%. For FSTI values of 0.5%, 0.75%, and 1.0%, the flow transitions after the shock. The change in transition method results in a peak in moment sensitivity. For the Mach 0.8 case at an AOA of 5°, the relaminarization of the 0.5% FSTI case is responsible for the peak in drag sensitivity.

5.5 Summary

This chapter presented the results of the Monte Carlo simulation for each of the S809, NACA 0012, SC1095, and RC(4)-10 airfoils. The importance of UQ analysis was demonstrated by showing how a normally distributed FSTI input

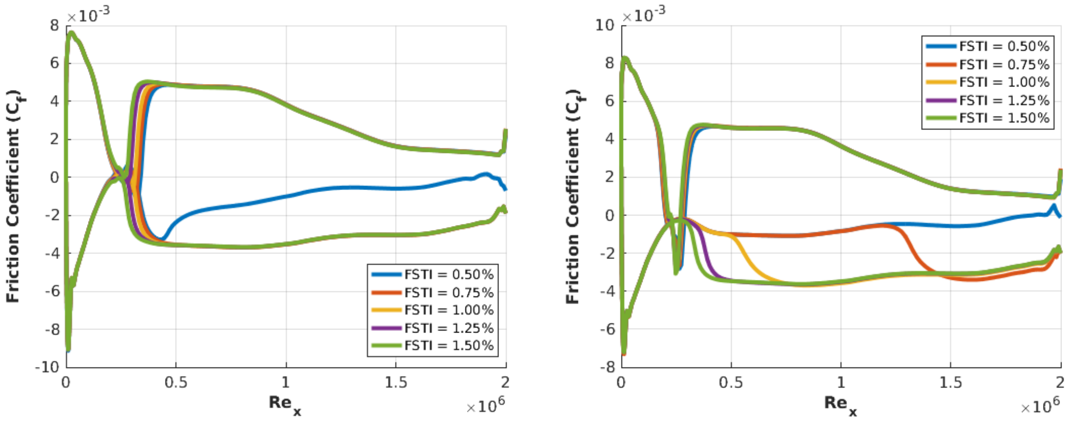

(a) AOA = 2°

(b) AOA = 3°

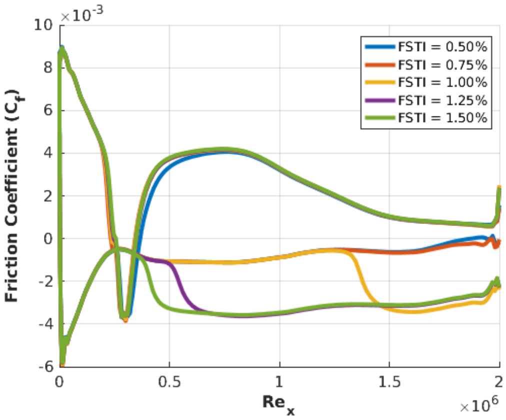

(c) AOA = 4°

Figure 5.18: Skin Friction Plots for RC(4)-10 Airfoil, Mach = 0.6, Re = 2×10^6

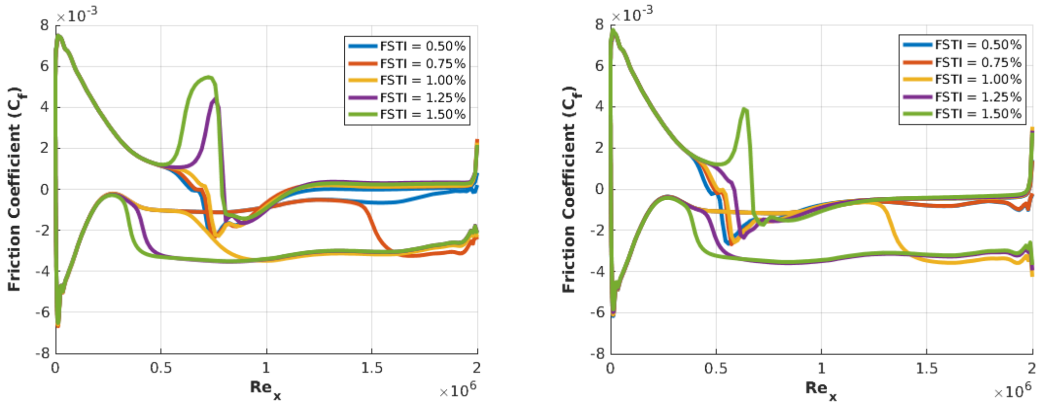

(a) Mach 0.7 - AOA = 4°

(b) Mach 0.7 - AOA = 5°

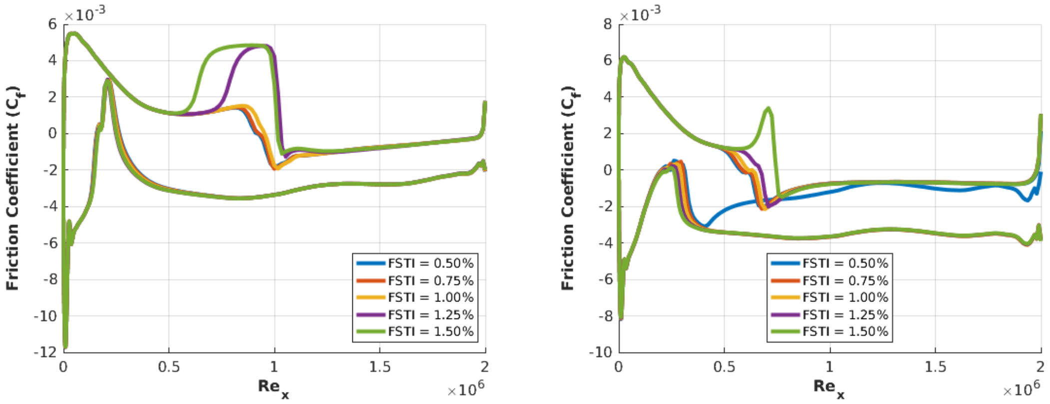

(c) Mach 0.8 - AOA = 1°

(d) Mach 0.8 - AOA = 5°

Figure 5.19: Skin Friction Plots for RC(4)-10 Airfoil, Mach = 0.7 - 0.8, Re = 2×10^6

could result in a non-Gaussian output, using a case from the S809 airfoil as an example. The mean input FSTI and standard deviations were varied for the S809 airfoil to show how this would affect the difference between discrete and mean outputs and the output standard deviations. For the NACA 0012, the Reynolds number was varied. The standard deviations of the aerodynamic coefficients featured spikes in sensitivity at certain AOA. The reasoning behind these peaks was explained for some of these cases, while the cause for some of the peaks require additional research. The results for the SC1095 and RC(4)-10 were also presented for Mach 0.2 to 0.8. Both airfoils showed similar sensitivity trends at Mach 0.2 and 0.4, when the flow is transonic. However, they exhibited different behavior at Mach 0.6 to 0.8. The physics behind some of the more interesting features of the graphs were explained.

Chapter 6

Conclusions

6.1 Summary

This thesis studied the effects of uncertainty on the aerodynamic coefficients of four airfoils. The study focused on the sensitivities of the aerodynamic coefficients to uncertainty in FSTI and examined how varying the mean FSTI, the input standard deviation, the Reynolds number, and the Mach number affected the sensitivity through UQ analysis.

The first chapter highlighted the importance of UQ and the motivation behind this work, before discussing boundary layer transition and providing an overview of UQ. The chapter went over the differences between laminar, turbulent, and transitional flow and described the physical mechanisms of transition and the different types of transition. The chapter then provided a brief overview of a few transition models that are currently used by CFD solvers. The chapter then described the field of UQ as well as different UQ techniques that were used for the present work.

The second chapter provided an overview of the CFD analysis used in this work. This included a description of the governing equations that are solved by the OVERTURNS flow solver and how these equations are non-dimensionalized. The RANS equations were then derived from the non-dimensionalized governing equations. A brief description of grid generation is provided. The chapter then reviewed how OVERTURNS uses numerical algorithms to solve the governing equations, including the incorporation of the turbulence and transition models.

The third chapter went through the UQ methodology used in this work. The chapter described how parametric sweeps were used to generate a surrogate surface to use in place of CFD calculations. The chapter then explained why the Monte Carlo method was chosen over stochastic collocation. Finally, the chapter described how the Monte Carlo method was implemented and provided validation results for the surrogate surface and the overall UQ analysis.

The fourth chapter presented the results of the parametric sweeps for the S809, NACA 0012, SC1095, and RC(4)-10. Results of interest were identified and the underlying physics were examined in order to understand the results. This uncovered cases with multiple laminar separation bubbles and cases with relaminarization. At higher Mach numbers, some cases with shock induced separation (with transition before or after the shock) were observed.

Finally, the fifth chapter went over the results of the UQ analysis. The Monte Carlo method was used to determine the expected means and standard deviations of the aerodynamic coefficients for each airfoil. The standard deviations provided a measure of the sensitivity of each aerodynamic coefficient to the uncertainty in FSTI. Cases were selected to be explored further to attempt to understand why the coefficients were more or less sensitive for a particular Mach/Reynolds number and AOA.

6.2 Key Observations

This section lists the key observations gleaned from the present work. Both general observations and specific results for each airfoil have been highlighted.

6.2.1 General Observations

- Although the input distribution of FSTI values was normally distibuted, the resulting output distributions were not always Gaussian.
- Mean values of lift and pitching moment were close to the values obtained with discrete FSTI inputs (i.e. without uncertainty). However, the mean drag values differed from the drag values obtained with discrete FSTI inputs when inside the drag bucket AOA range.
- Even when the mean outputs were close to the values obtained with discrete

FSTI, the standard deviations of the aerodynamic coefficients were large enough to be statistically relevant.

6.2.2 S809

- The UQ analysis performed on the S809 airfoil demonstrated that the sensitivity trends of the aerodynamic coefficients is dependent on the mean FSTI value. Although this was expected, the S809 cases provided confirmation as well as showed how much the sensitivity could change. For example, the standard deviation for the coefficient of lift was reduced by over a factor of 4 when the input mean FSTI value was changed from 1.0% to 2.0% for an AOA of 4°.
- The S809 case was also used to show how reducing the input standard deviation affects the sensitivity of the aerodynamic coefficients. While the trends remained the same, the standard deviations of the aerodynamic coefficients were reduced, which was expected. However, as the angle of attack increases, the difference in standard deviations decrease, indicating that varying FSTI at these high angles of attack does not impact the results as much.
- All three aerodynamic coefficients have peaks in standard deviation at an AOA of 4°. This is due to the drag bucket phenomenon. Near 4° AOA, the viscous drag increases rapidly in response to small increases in FSTI.

6.2.3 NACA 0012

- At Reynolds numbers of 500,000 and 1 million, a double separation bubble forms at certain AOA and FSTI values. This double separation bubble is responsible for fluctuations in sensitivity for the aerodynamic coefficients. For a given AOA, the double separation bubble will appear for a certain threshold of FSTI values. If the FSTI is increased/decreased slightly at the edges of this threshold, the double separation bubble will form or disappear, resulting in a relatively large change in drag. When the double separation bubble occurs near the leading edge, it also increases the effective camber, leading to changes in lift and moment as well. Therefore as threshold values approach the mean input FSTI value, the sensitivity of the coefficients increase.
- At Reynolds numbers of 2 million and 4 million, as AOA increases, the transition location approaches the leading edge of the airfoil. At high AOA, the flow transitions close to or at the leading edge and is therefore able to remain attached to the airfoil after transitions. This leads to increases in drag as FSTI increases. At Reynolds numbers of 500,000 and 1 million, at high angles of attack, the drag remains relatively constant as FSTI increases, since the flow separates after transition.
- Change in transition location affects the sensitivity of the aerodynamic coefficients. The more that the transition locations for a set increase/decrease in FSTI, the more that the sensitivity of the aerodynamic coefficients change.

- At Reynolds numbers of 2 million and 4 million, sharp peaks occur at certain AOA. The causes for these peaks were not able to be determined; further work is required to provide an explanation.

6.2.4 SC1095 and RC(4)-10

- The RC(4)-10 exhibits an interesting phenomenon at AOA of 2° for Mach 0.4 and Mach 0.6. At an FSTI value of 0.5% (and 0.05% at Mach 0.6), the flow on the lower surface transitions, but then relaminarizes. This does not occur for the SC1095. This relaminarization is attributed to the increased camber of the leading edge and the flatter lower surface of the RC(4)-10.
- For Mach numbers 0.2 and 0.4, the sensitivity trends are very similar. This is due to the fact that at these Mach numbers and AOA, the flow is subsonic and incompressible. However, for Mach 0.6 to 0.8, the flow becomes transonic and is no longer incompressible. This results in large fluctuations in the sensitivity of the aerodynamic coefficients to uncertainty in FSTI. At these Mach numbers, the trends differ between the SC1095 and the RC(4)-10.
- Spikes in sensitivity occur when small changes in FSTI near the mean input FSTI of 1.0% result in the transition location moving before, after, or at the shock location. Each scenario results in a different skin friction profile, which affects all three aerodynamic coefficients.

6.3 Contributions

Currently, UQ is not widely implemented in CFD results. Most CFD papers do not address the role of uncertainty in the published results. However, incorporating UQ analysis into CFD results can provide additional information to be used for design and reliability analysis. In addition, it will make CFD results more accurate by taking into account uncertainties that exist in the physical world in CFD calculations.

The present work takes the first step into incorporating UQ analysis for CFD results for uncertainty in FSTI specifically and lays the foundation for establishing a UQ framework for flow transition studies in general. Specifically, the sensitivity analysis provided in this work can be used in conjunction with CFD simulations in order to obtain more accurate results. The sensitivity analysis can also be used in rotor design, allowing designers to select airfoils which are less sensitive to uncertainty in FSTI at the expected operating conditions of the rotor. The present work also provides the UQ framework so that a similar approach can be taken for different airfoils as well as different input quantities besides FSTI.

Finally, this work required extensive parametric studies, varying FSTI, AOA, Reynolds number, and Mach number. The result was a treasure trove of data, from which several key points were highlighted. There has been little to no work previously that has examined small changes in FSTI values to this extent. While the present work has highlighted a number of key observations, there is always more that can be gleaned from all of the data.

6.4 Recommendations for Future Work

The work presented in this thesis represents only a small subsection of the work possible for applying UQ to CFD results. There are numerous ways to build upon this research and expand further. Some of the possible ways to do so are listed below:

- The sensitivity analysis unearthed a number of features that remain unexplained. Further work is required to determine why at certain conditions there are peaks in the sensitivity of the aerodynamic coefficients to uncertainty in FSTI.
- The present work assumed that the uncertainty in FSTI was Gaussian. However, the methodology presented here can easily be applied to any other probability distribution. Future work could include experimental studies to make the probability distribution of FSTI more representative of the physical world. This would improve the accuracy of the UQ analysis.
- While examining the results of the parametric studies, a number of key findings were highlighted. However, there were many additional findings that were left unaddressed. A thorough review of the parametric study results would yield additional findings.

- The present work was limited to isolated two-dimensional airfoils. However, the UQ methodology can be applied to FSTI for three dimensional objects, such as rotors as a whole and/or fuselages.

- The present work was concerned with the effect of uncertainty in FSTI on the aerodynamic coefficients. A possible subject of future work would be to utilize the distributions of sectional aerodynamics due to uncertainty in FSTI in a comprehensive rotor analysis. The effect of uncertainty can be propagated forward to see the impacts on performance, vibrations, and/or acoustics.

- While the present work was solely concerned with uncertainty in FSTI, the UQ methodology established here can be applied to other input variables. One example would be surface roughness, which is another factor which impacts transition onset. There are transition models, including the model used by OVERTURNS, which incorporate surface roughness in the model. The UQ methodology can therefore be applied in a similar fashion to uncertainty in surface roughness.

- The current work can be utilized as a small component in a much larger project to formalize the use of UQ in CFD. Such a project could take the form of a tool that could automate the UQ analysis and provide sensitivities of the aerodynamic coefficients for requested flow conditions. However, this would require that parametric studies are already conducted for the requested flow conditions and airfoil in use. Another possible form would be to use the current methodology to generate “uncertainty reference tables” for various airfoils.

Appendices

Appendix A

Complete Parametric Sweep Results

A.1 Introduction

In this work, parametric sweeps are used to generate the surrogate surfaces used for UQ analysis (see Sec. 1.3). The complete results of the parametric sweeps are provided for reference here for all four airfoils used in this study. The freestream conditions for the parametric sweeps are provided in Table 3.1.

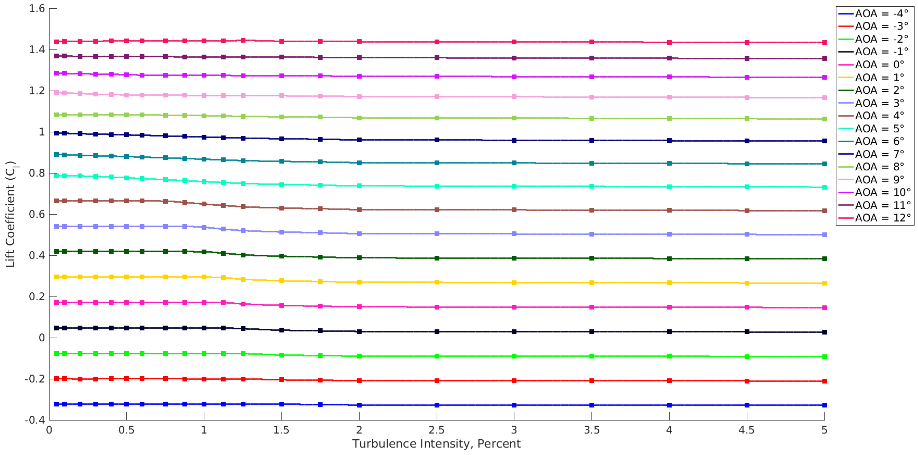

(a) Lift coefficient

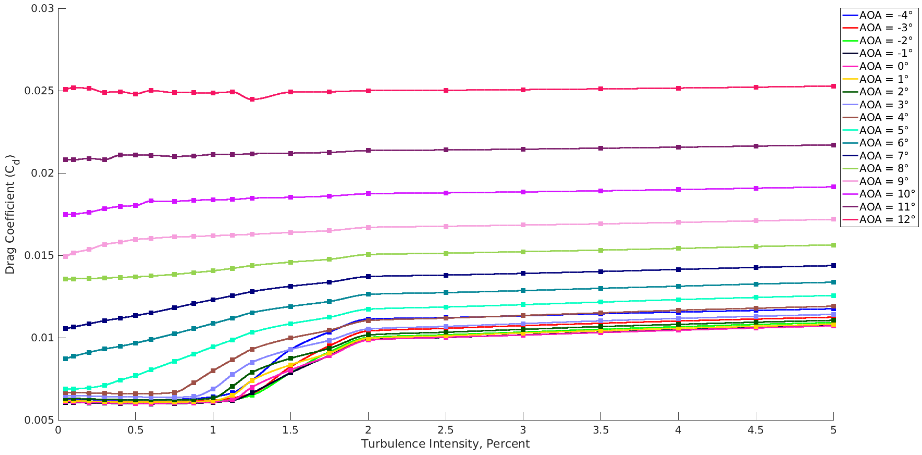

(b) Drag coefficient

Figure A.1: Parametric Sweep for S809 Airfoil at Mach = 0.2, Re = 2×10^6

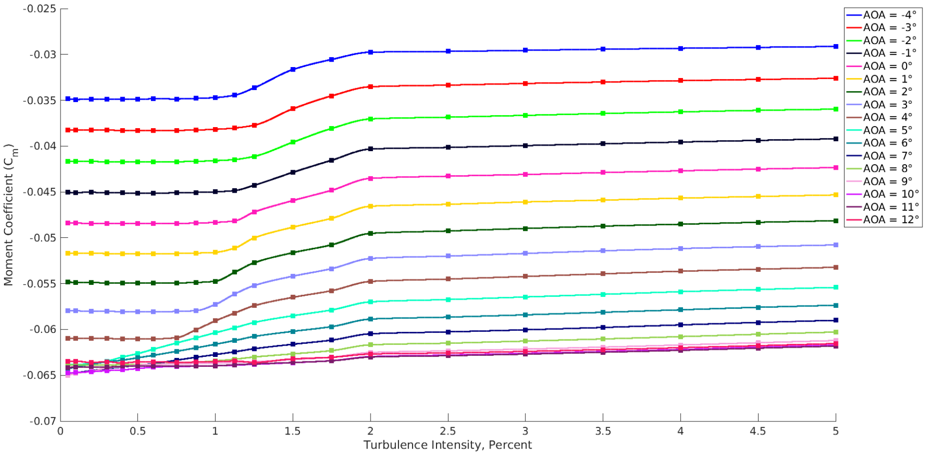

(c) Moment coefficient

Figure A.1: Parametric Sweep for S809 Airfoil at Mach = 0.2, Re = 2×10^6 (cont.)

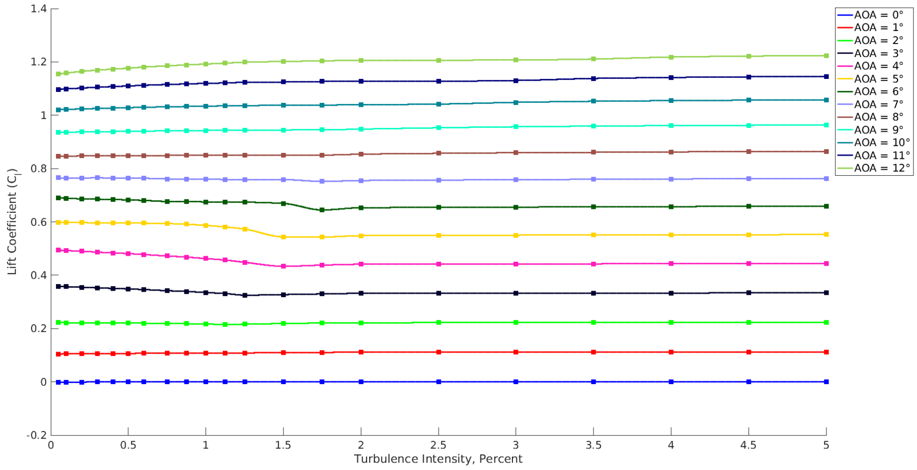

(a) Lift coefficient

Figure A.2: Parametric Sweep for NACA 0012 Airfoil at Mach = 0.2, Re = 0.5×10^6

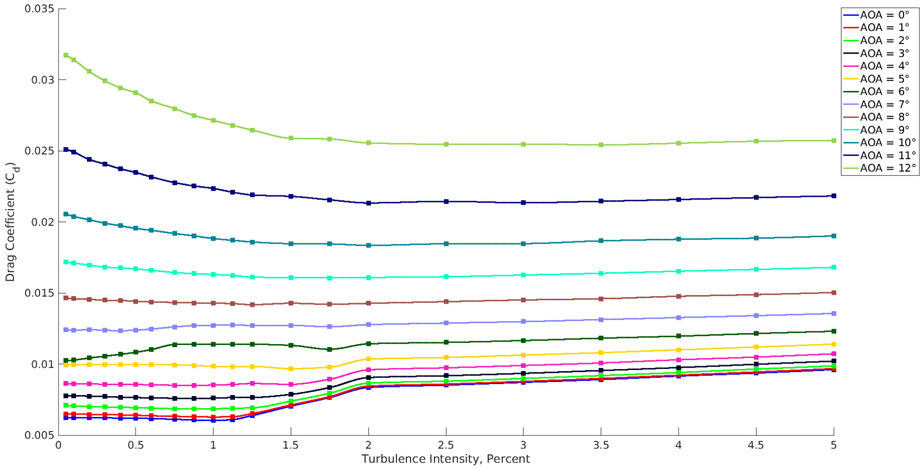

(b) Drag coefficient

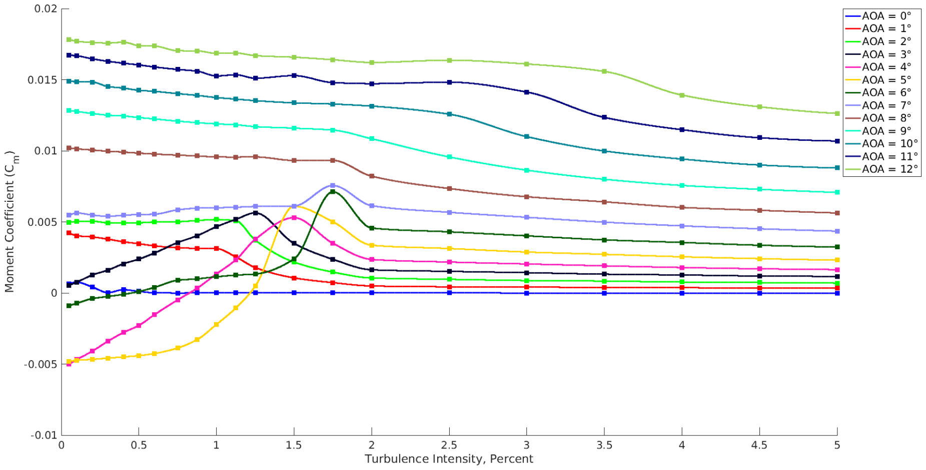

(c) Moment coefficient

Figure A.2: Parametric Sweep for NACA 0012 Airfoil at Mach = 0.2, Re = 0.5×10^6 (cont.)

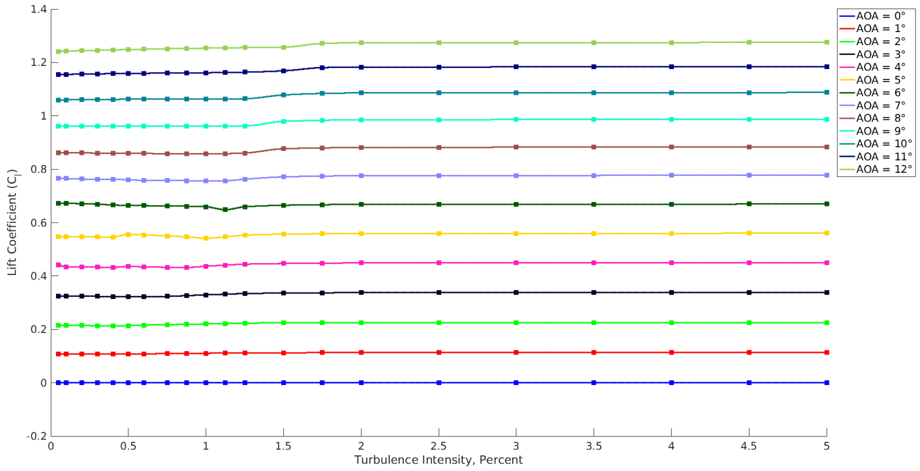

(a) Lift coefficient

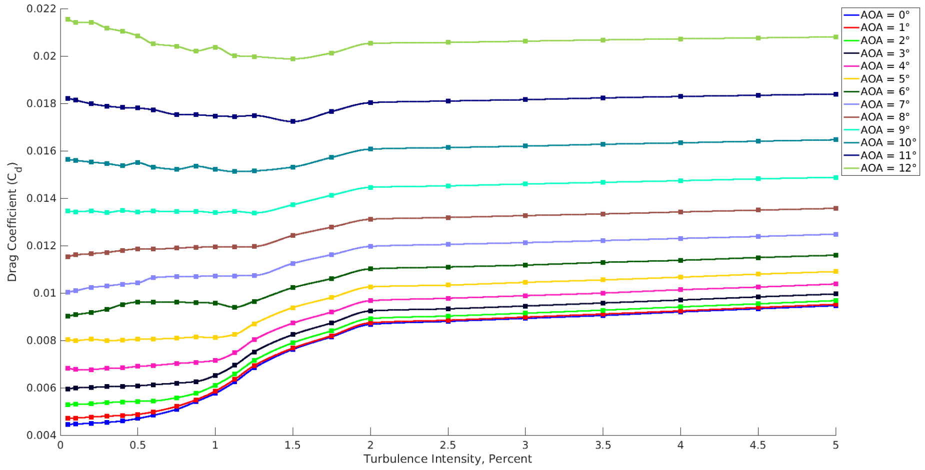

(b) Drag coefficient

Figure A.3: Parametric Sweep for NACA 0012 Airfoil at Mach = 0.2, Re = 1×10^6

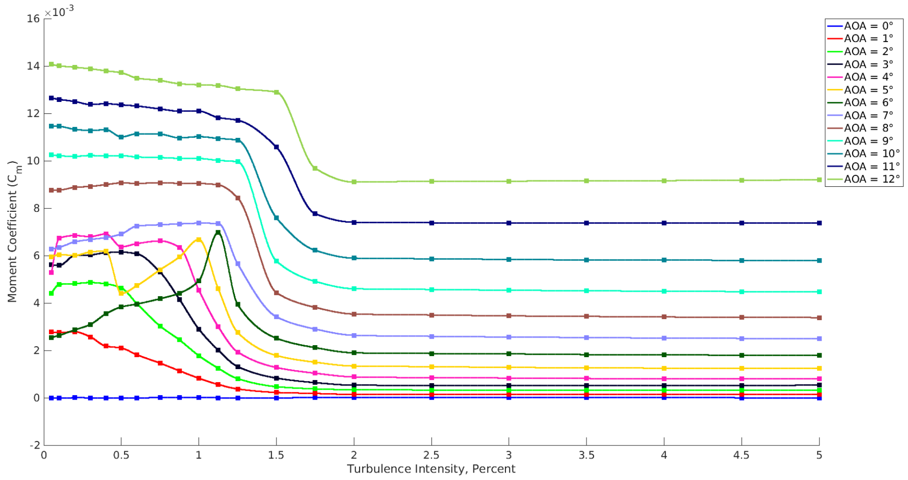

(c) Moment coefficient

Figure A.3: Parametric Sweep for NACA 0012 Airfoil at Mach = 0.2, Re = 1×10^6 (cont.)

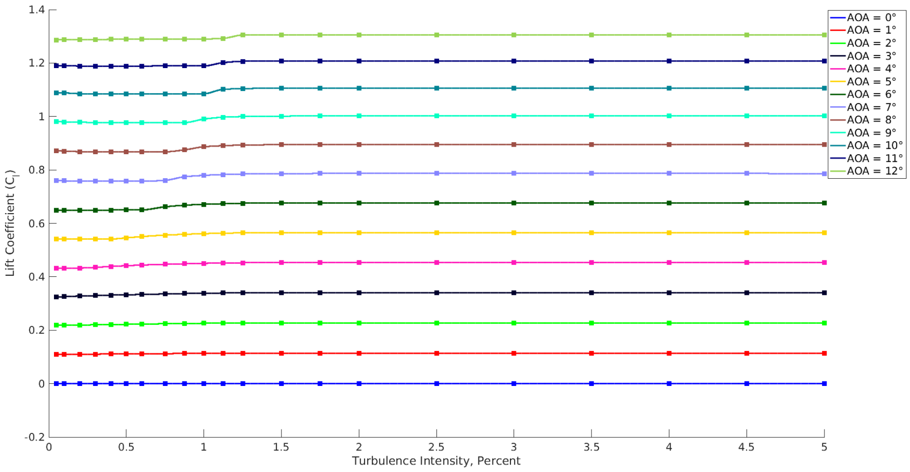

(a) Lift coefficient

Figure A.4: Parametric Sweep for NACA 0012 Airfoil at Mach = 0.2, Re = 2×10^6

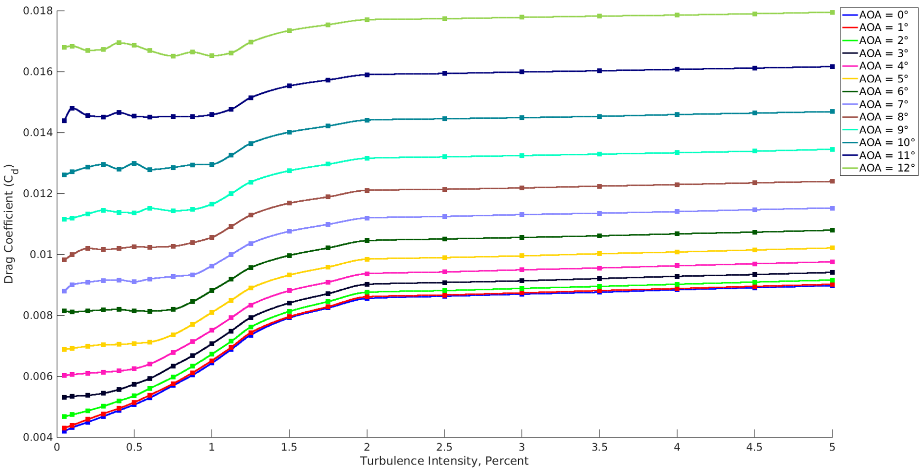

(b) Drag coefficient

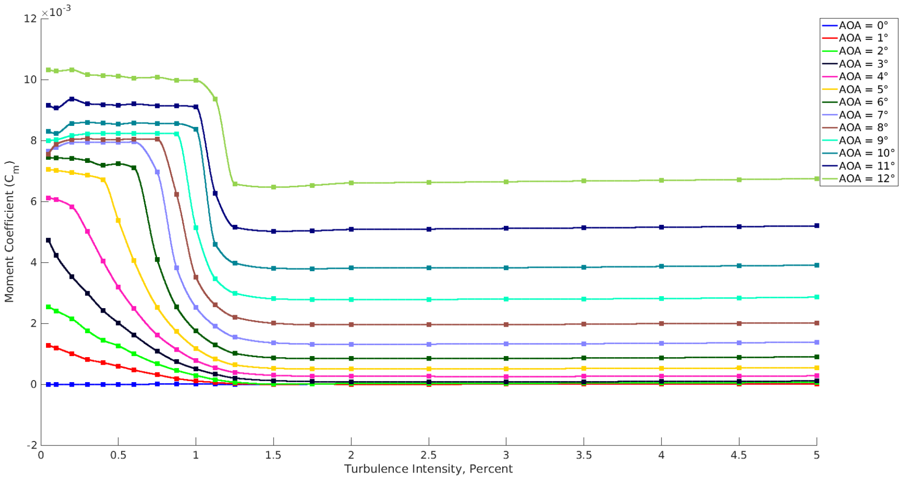

(c) Moment coefficient

Figure A.4: Parametric Sweep for NACA 0012 Airfoil at Mach = 0.2, Re = 2×10^6 (cont.)

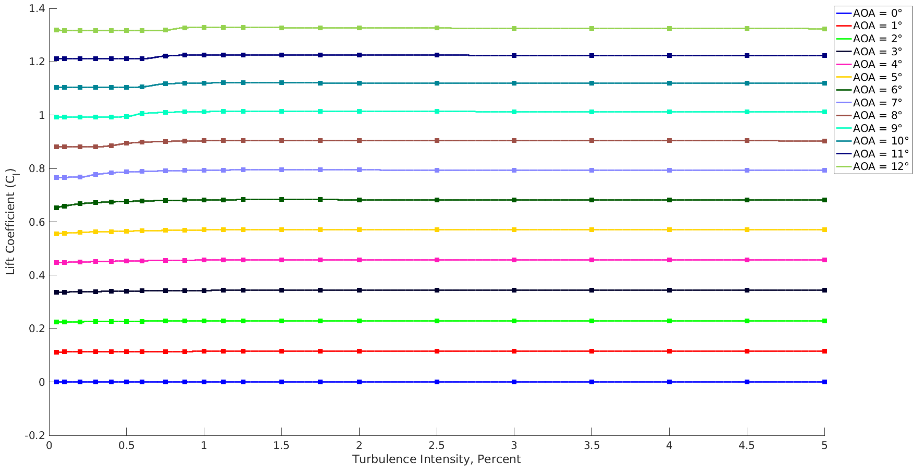

(a) Lift coefficient

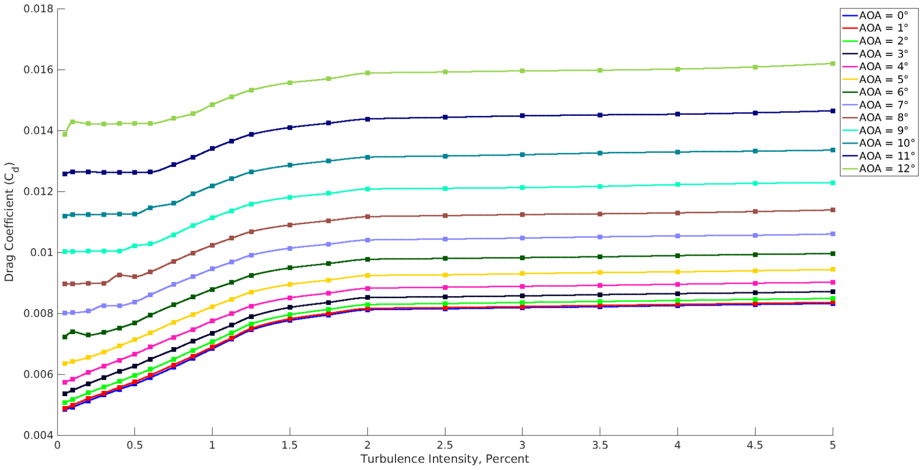

(b) Drag coefficient

Figure A.5: Parametric Sweep for NACA 0012 Airfoil at Mach = 0.2, Re = 4×10^6

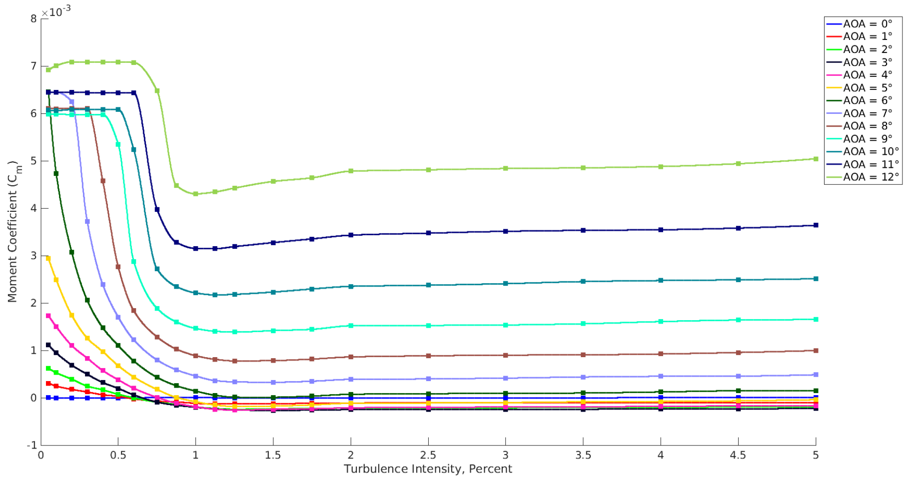

(c) Moment coefficient

Figure A.5: Parametric Sweep for NACA 0012 Airfoil at Mach = 0.2, Re = 4×10^6 (cont.)

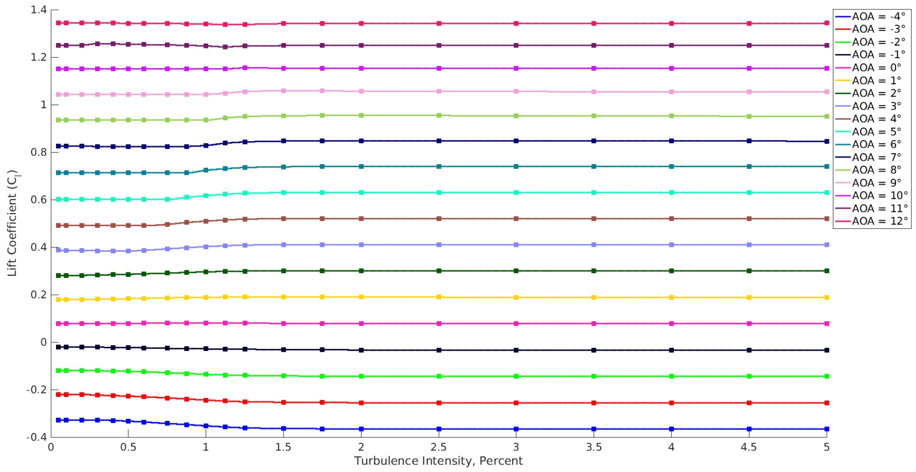

(a) Lift coefficient

Figure A.6: Parametric Sweep for SC1095 Airfoil at Mach = 0.2, Re = 2×10^6

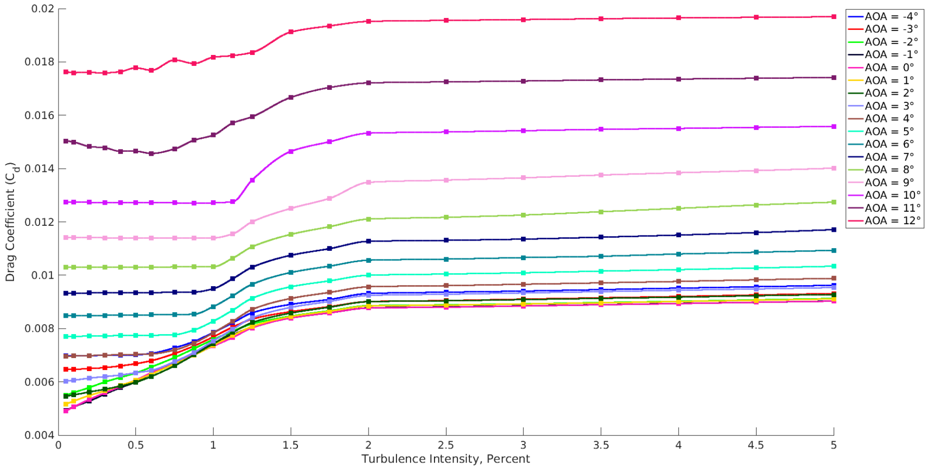

(b) Drag coefficient

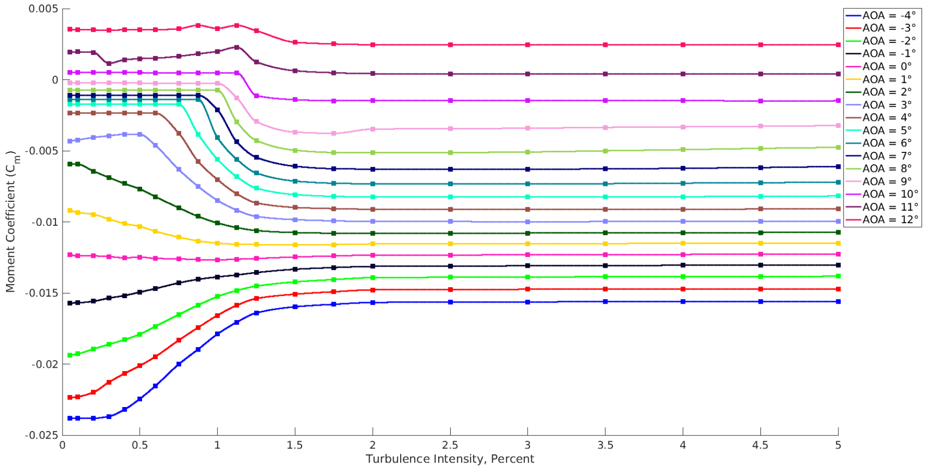

(c) Moment coefficient

Figure A.6: Parametric Sweep for SC1095 Airfoil at Mach = 0.2, Re = 2×10^6 (cont.)

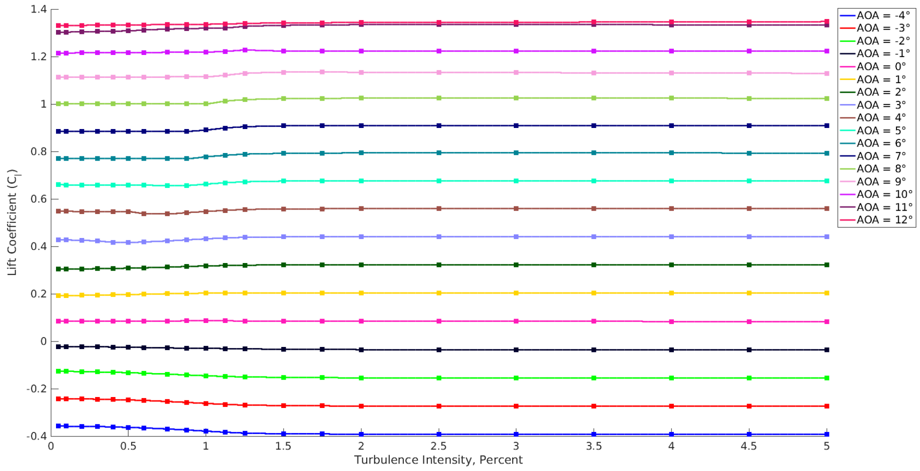

(a) Lift coefficient

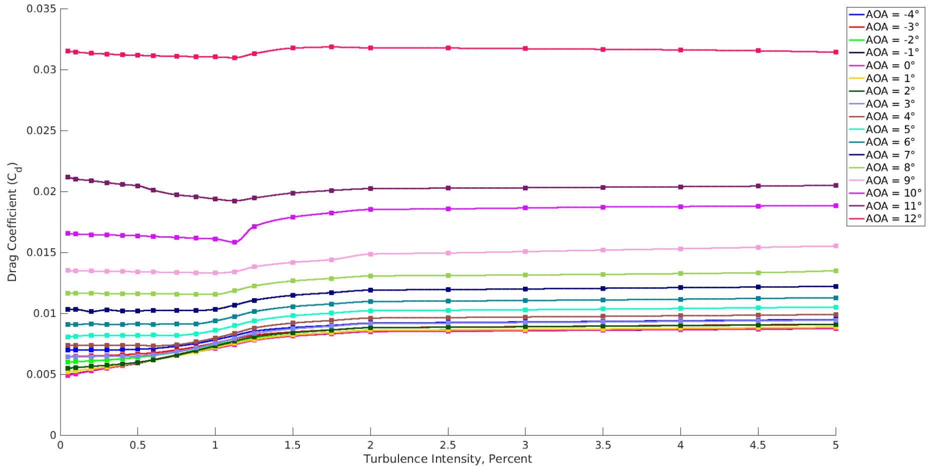

(b) Drag coefficient

Figure A.7: Parametric Sweep for SC1095 Airfoil at Mach = 0.4, Re = 2×10^6

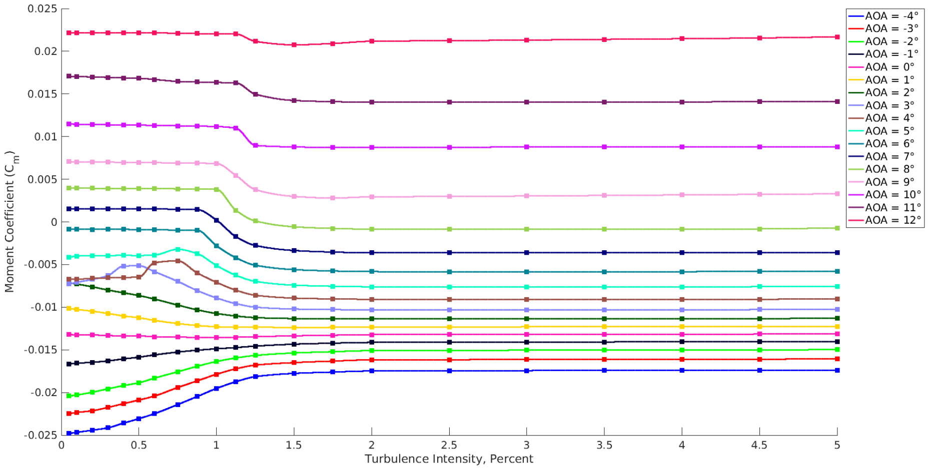

(c) Moment coefficient

Figure A.7: Parametric Sweep for SC1095 Airfoil at Mach = 0.4, Re = 2×10^6 (cont.)

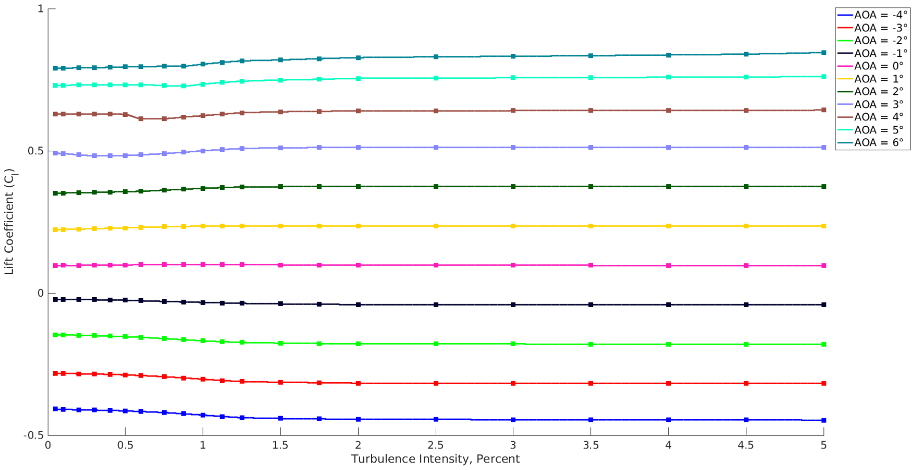

(a) Lift coefficient

Figure A.8: Parametric Sweep for SC1095 Airfoil at Mach = 0.6, Re = 2×10^6

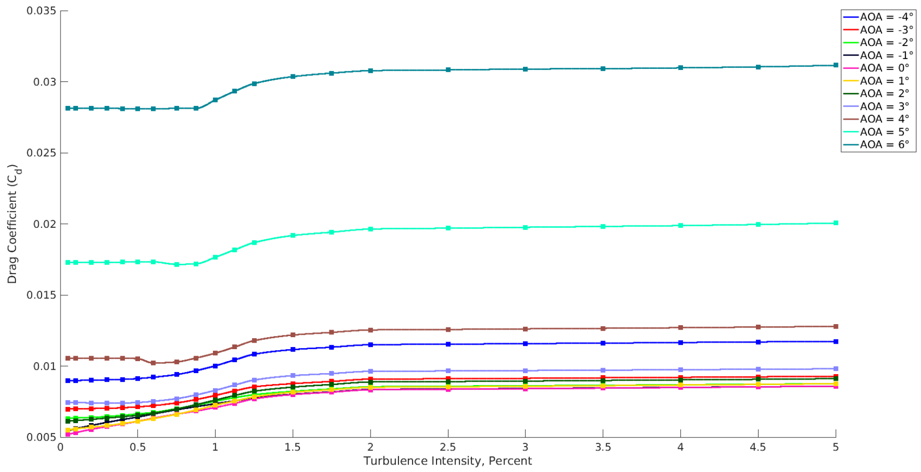

(b) Drag coefficient

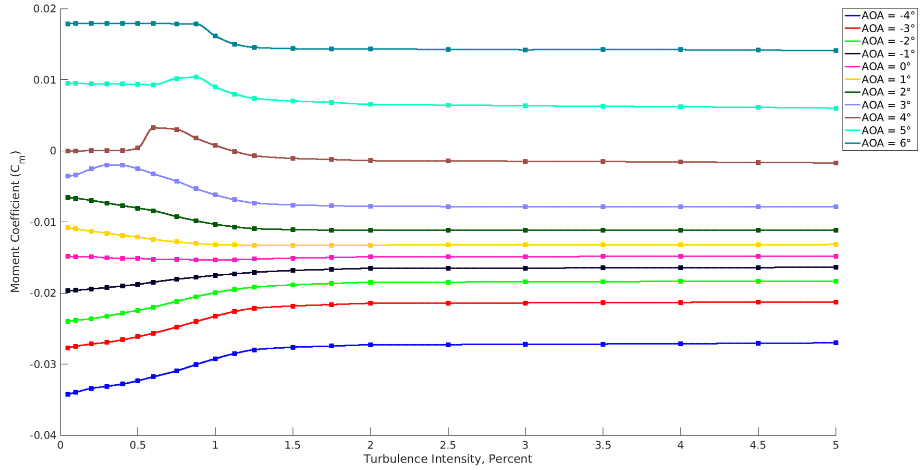

(c) Moment coefficient

Figure A.8: Parametric Sweep for SC1095 Airfoil at Mach = 0.6, Re = 2×10^6 (cont.)

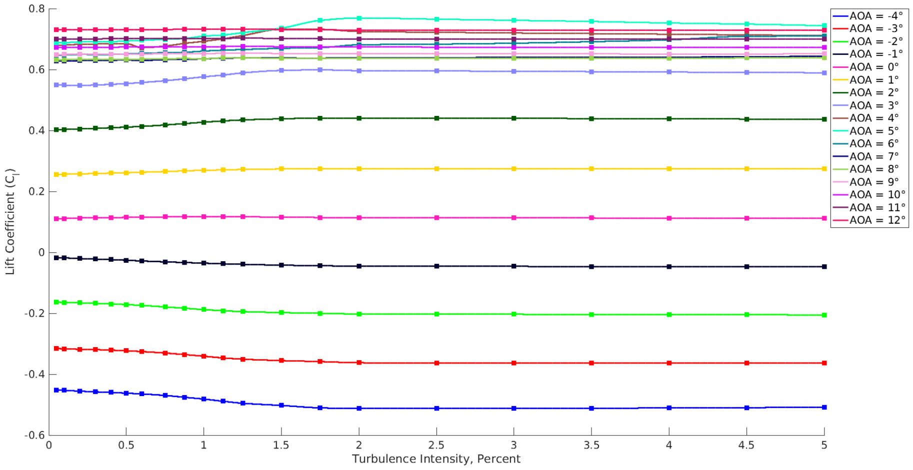

(a) Lift coefficient

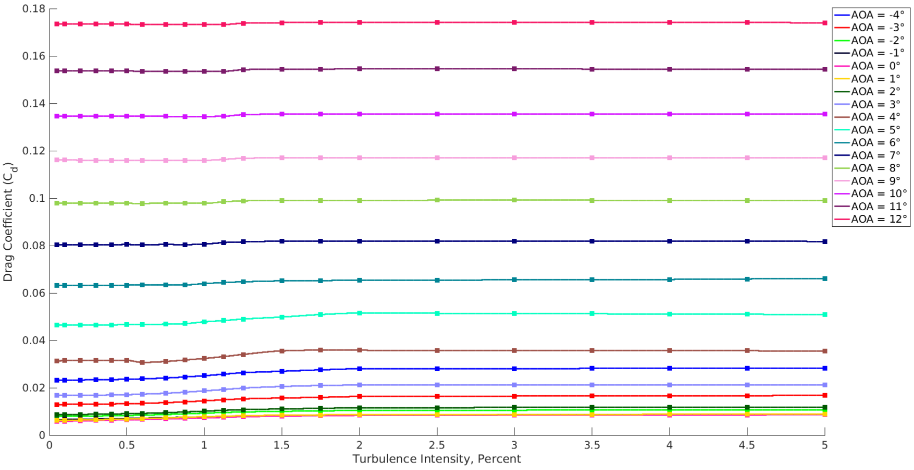

(b) Drag coefficient

Figure A.9: Parametric Sweep for SC1095 Airfoil at Mach = 0.7, Re = 2×10^6

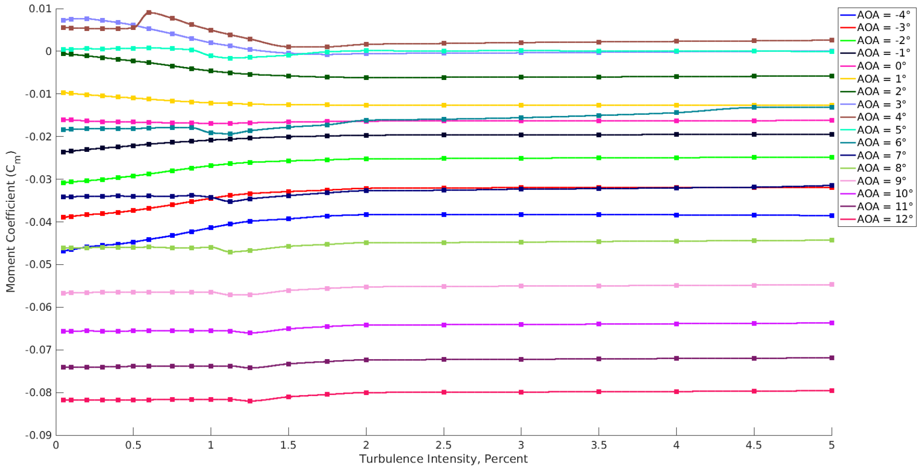

(c) Moment coefficient

Figure A.9: Parametric Sweep for SC1095 Airfoil at Mach = 0.7, Re = 2×10^6 (cont.)

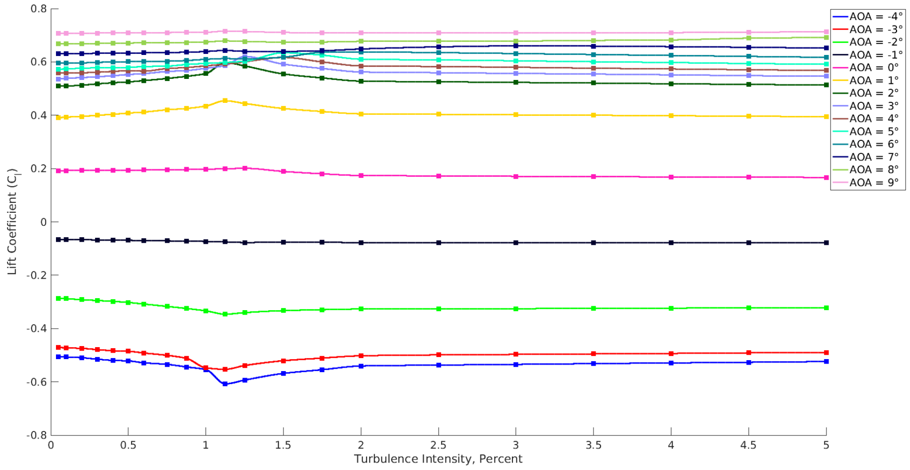

(a) Lift coefficient

Figure A.10: Parametric Sweep for SC1095 Airfoil at Mach = 0.8, Re = 2×10^6

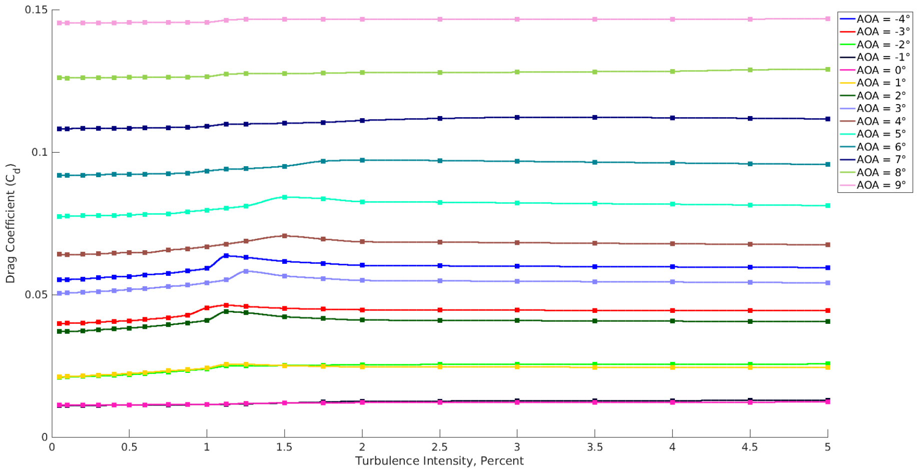

(b) Drag coefficient

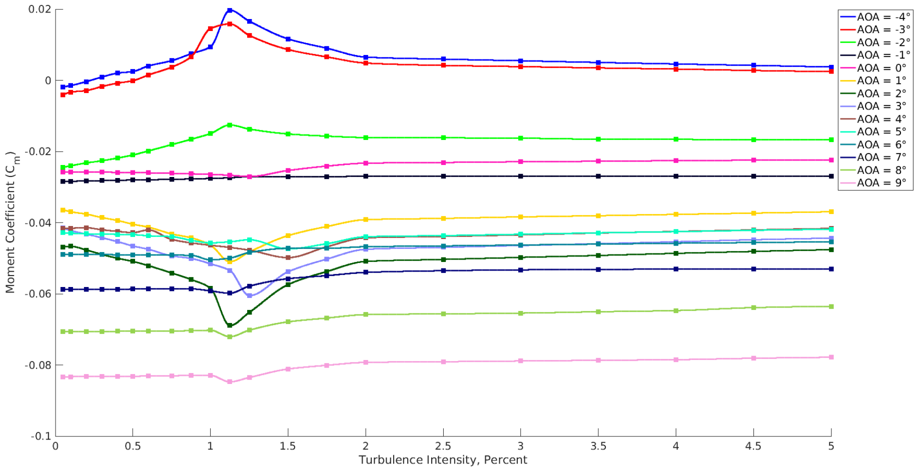

(c) Moment coefficient

Figure A.10: Parametric Sweep for SC1095 Airfoil at Mach = 0.8, Re = 2×10^6 (cont.)

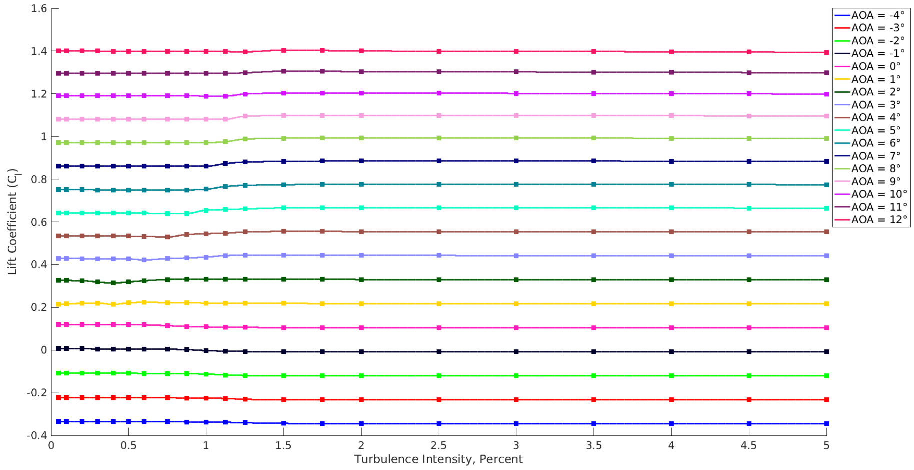

(a) Lift coefficient

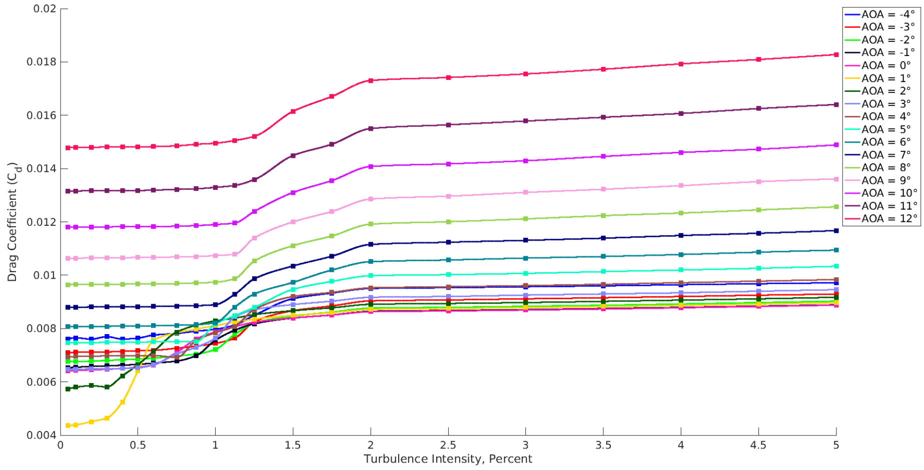

(b) Drag coefficient

Figure A.11: Parametric Sweep for RC(4)-10 Airfoil at Mach = 0.2, Re = 2×10^6

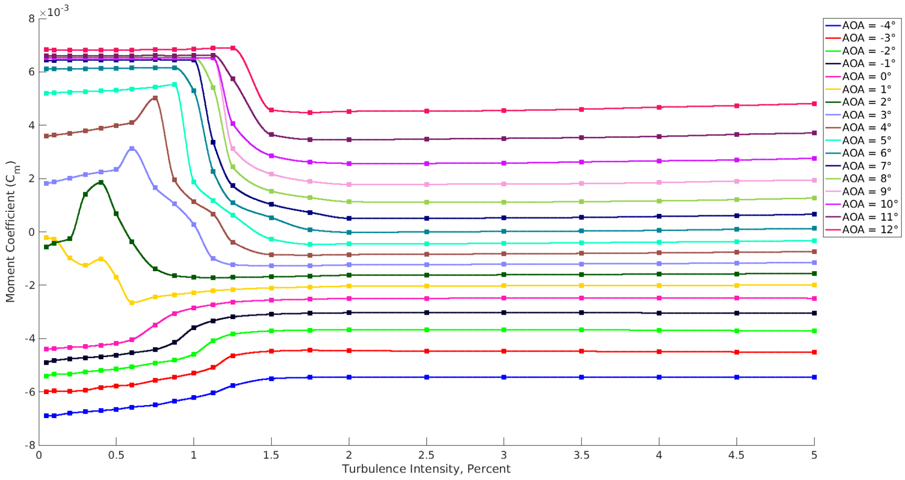

(c) Moment coefficient

Figure A.11: Parametric Sweep for RC(4)-10 Airfoil at Mach = 0.2, Re = 2×10^6 (cont.)

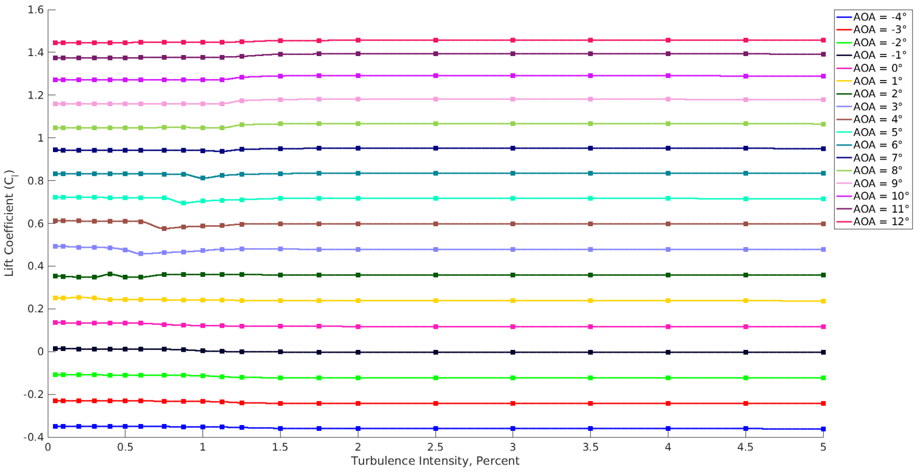

(a) Lift coefficient

Figure A.12: Parametric Sweep for RC(4)-10 Airfoil at Mach = 0.4, Re = 2×10^6

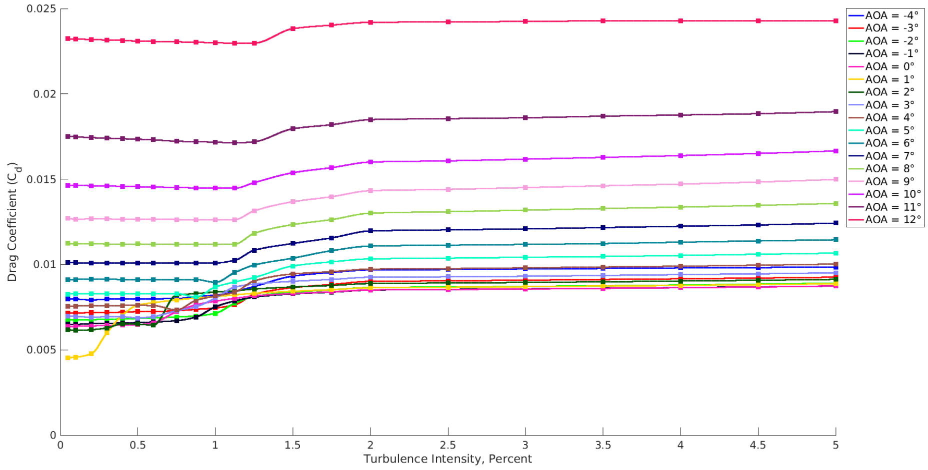

(b) Drag coefficient

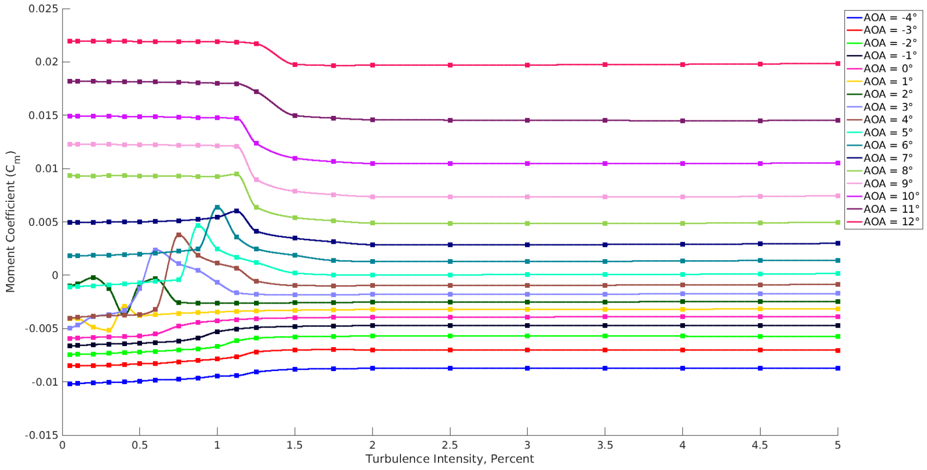

(c) Moment coefficient

Figure A.12: Parametric Sweep for RC(4)-10 Airfoil at Mach = 0.4, Re = 2×10^6 (cont.)

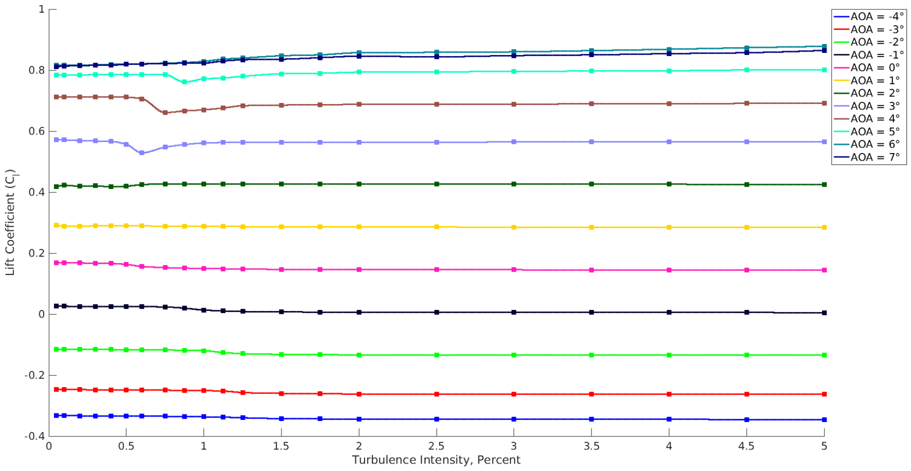

(a) Lift coefficient

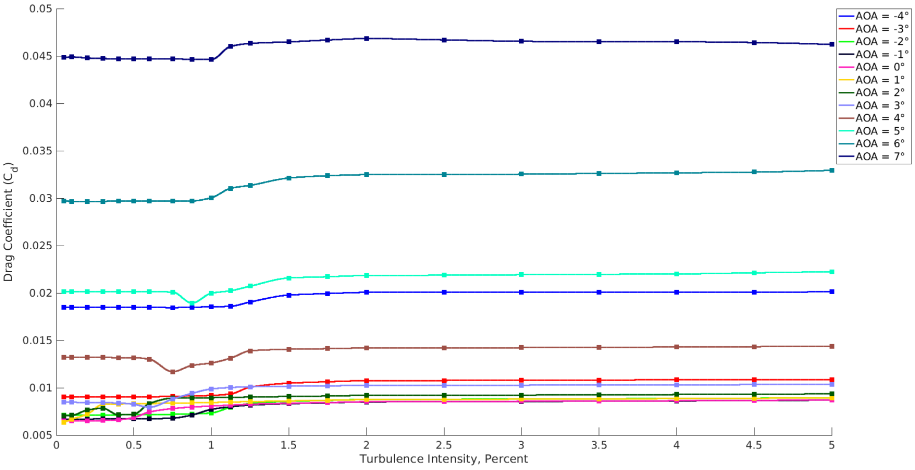

(b) Drag coefficient

Figure A.13: Parametric Sweep for RC(4)-10 Airfoil at Mach = 0.6, Re = 2×10^6

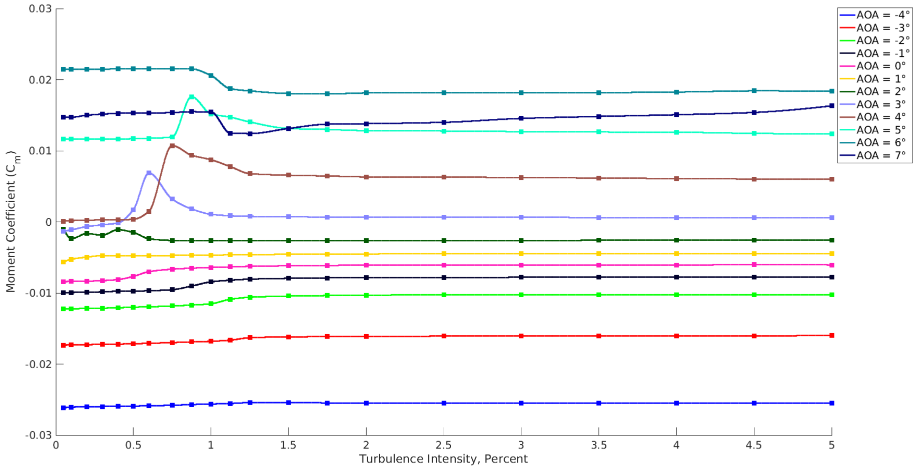

(c) Moment coefficient

Figure A.13: Parametric Sweep for RC(4)-10 Airfoil at Mach = 0.6, Re = 2×10^6 (cont.)

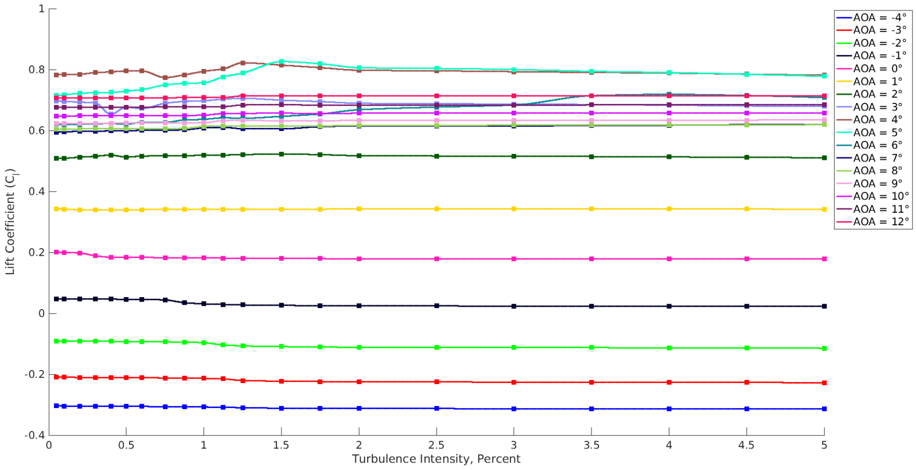

(a) Lift coefficient

Figure A.14: Parametric Sweep for RC(4)-10 Airfoil at Mach = 0.7, Re = 2×10^6

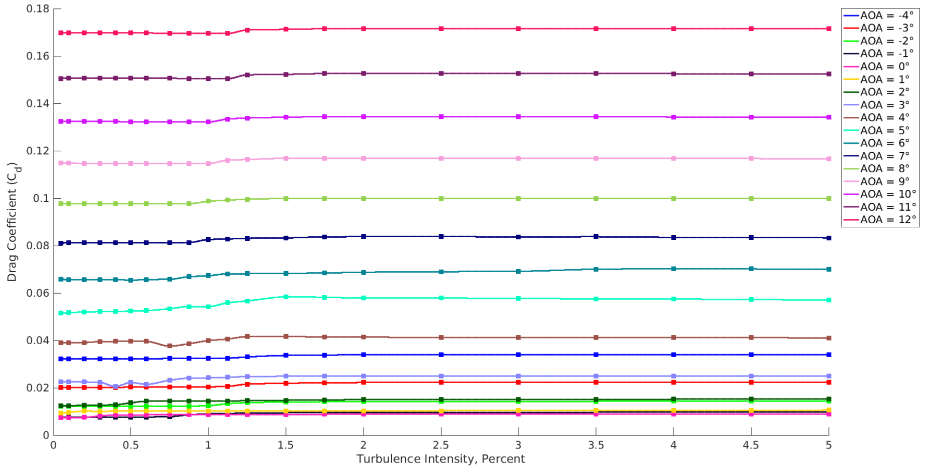

(b) Drag coefficient

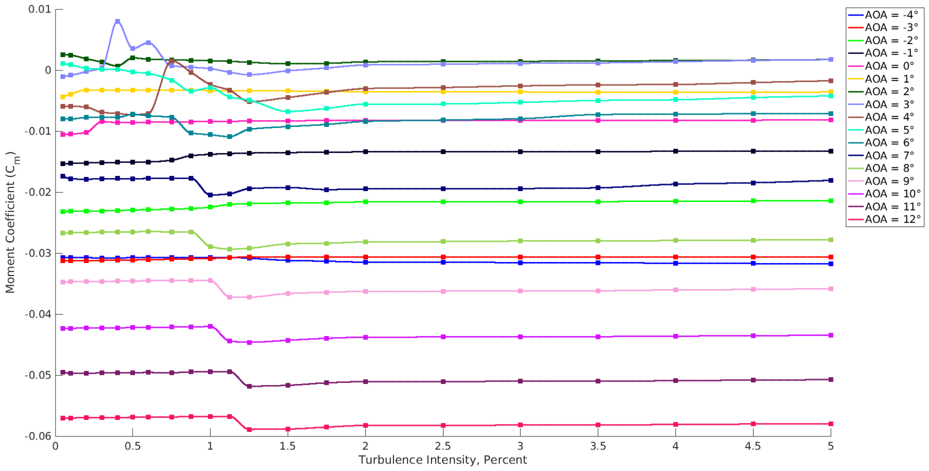

(c) Moment coefficient

Figure A.14: Parametric Sweep for RC(4)-10 Airfoil at Mach = 0.7, Re = 2×10^6 (cont.)

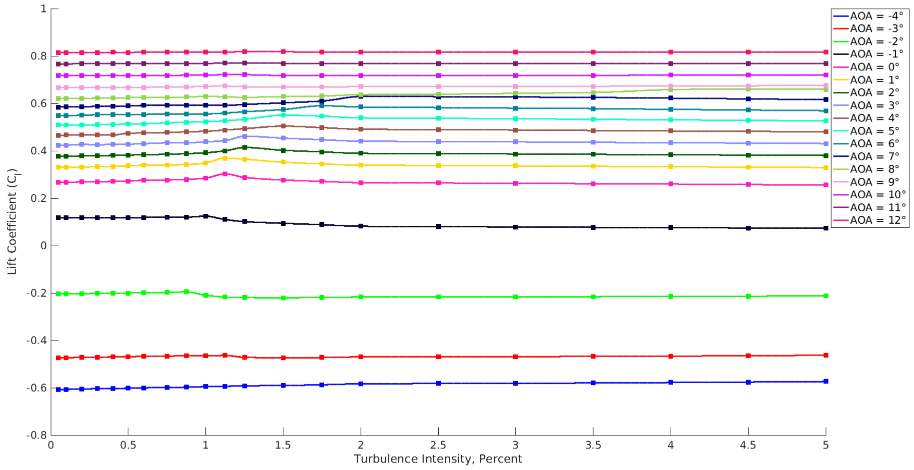

(a) Lift coefficient

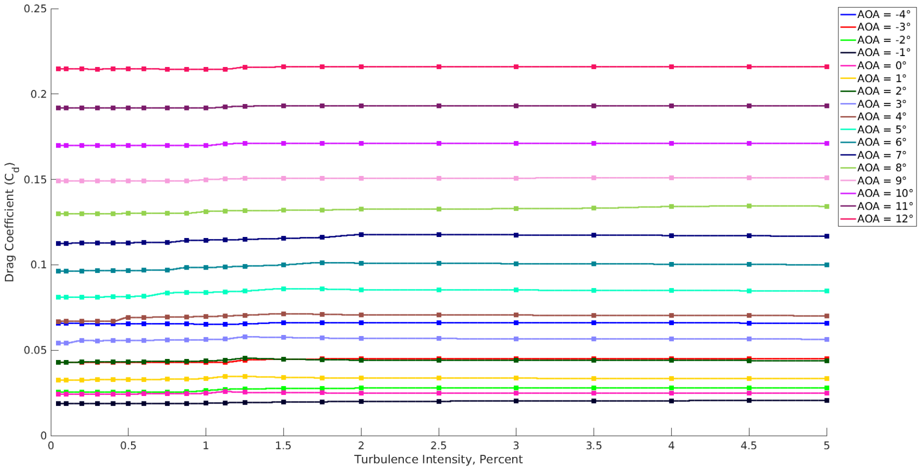

(b) Drag coefficient

Figure A.15: Parametric Sweep for RC(4)-10 Airfoil at Mach = 0.8, Re = 2×10^6

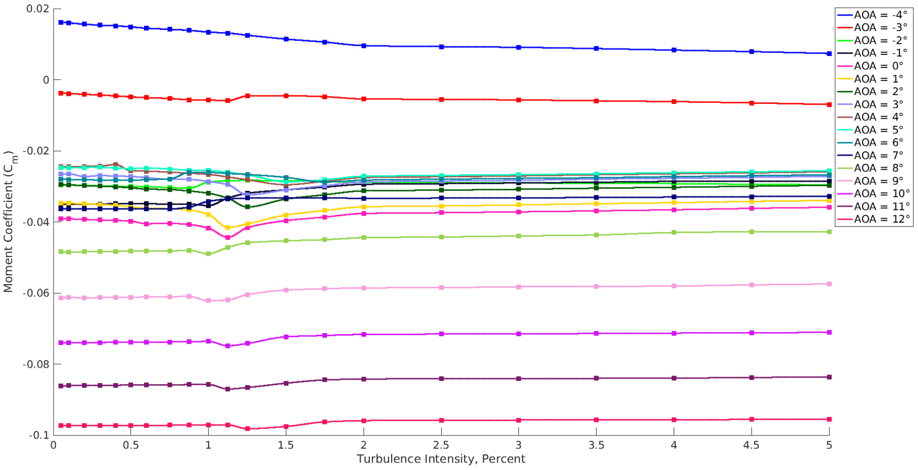

(c) Moment coefficient

Figure A.15: Parametric Sweep for RC(4)-10 Airfoil at Mach = 0.8, Re = 2×10^6 (cont.)

Bibliography

[1] Morkovin, M. V., Arnal, D., Mack, L. M., Reshotko, E., Poll, D. I. A., and Herbert, T., “Special Course on Stability and Transition of Laminar Flow,” Technical Report AGARD-R-709, AGARD, von Karman Institute Rhode-Saint-Genese, Belgium, 1984.

[2] Reshotko E., “Boundary-layer Stability and Transition,” Annual Review of Fluid Mechanics, vol. 8, pp.311–349, 1976.

[3] Morkovin, M. V., “On the Many Faces of Transition,” In Proceedings of the Symposium on Viscous Drag Reduction. Plenum Press, New York, 1969.

[4] Emmons, H. W., “The Laminar-Turbulent Transition in a Boundary Layer - Part 1,” Journal of Aerospace Science, 18(7), pp. 490–498, 1951.

[5] Dhawan, S. and Narasimha, R., “Some Properties of Boundary Layer Flow During the Transition from Laminar to Turbulent Motion,” Journal of Fluid Mechanics, vol. 3, no. 4, pp. 418–436, 1958.

[6] Medida, S., “Correlation-based Transition Modeling for External Aerodynamic Flows.” PhD thesis. University of Maryland, 2014.

[7] Orr, W. MF., "The Stability or Instability of the Steady Motions of a Perfect Liquid and of a Viscous Liquid. Part i: A Perfect Liquid," In Proceedings of the Royal Irish Academy A, number 27, pp. 9–68, 1907.

[8] Orr, W. MF., "The Stability or Instability of the Steady Motions of a Perfect Liquid and of a Viscous Liquid. Part ii: A Viscous Liquid," In Proceedings of the Royal Irish Academy A, number 27, pp. 69–138, 1907.

[9] Smith, A. M. O. and Gamberoni, N., "Transition Pressure Gradient and Stability Theory," Douglas Aircraft Company, Long Beach, California. Rep. ES 26388 , 1956.

[10] Kapsalis, P-C.S., Voutsinas, S., Vlachos, N., "Comparing the Effect of Three Transition Models on the CFD Predictions of a NACA0012 Airfoil Aerodynamics," Journal of Wind Engineering and Industrial Aerodynamics, vol. 157, pp. 158-170, 2016.

[11] Herbert, T., "Parabolized Stability Equations," Annual Review of Fluid Mechanics, vol. 29, pp 245-283, 1997.

[12] Van Ingen J. L., "A Suggested Semi-Empirical Method for Calculation of the Boundary Layer Transition Region," Technical Report Rep. VTH-74, University of Delft, Dept. of Aerospace Engineering, Delft, The Netherlands, 1956.

[13] Stock, H., and Degenhart, E., "A Simplified e^N Method for Transition Prediction in Two-Dimensional, Incompressible Boundary Layers," Z. Flugwiss. Weltraumforschung vol. 13, pp. 16–30, 1989.

[14] Coder, J. G., and Maughmer, M. D., "A CFD-Compatible Transition Model Using an Amplification Factor Transport Equation," In 51^{st} AIAA Aerospace Sciences Meeting including the New Horizons Forum and Aerospace Exposition, number 2013-0253. AIAA, 2013.

[15] Van Driest, E. R., and Blumer, C. B., "Boundary Layer Transition: Freestream Turbulence and Pressure Gradient Effects," AIAA Journal, vol. 1, no. 6, pp. 1303–1306, 1963.

[16] Langtry, R. B., and Menter, F. R., "Correlation-Based Transition Modeling for Unstructured Parallelized Computational Fluid Dynamics Codes," AIAA Journal, vol. 47, no. 12, pp. 2894-2906, 2009.

[17] Knupp, P., and Salari, K., Verification of Computer Codes in Computational Science and Engineering, Chapman and Hall/CRC, Boca Raton, FL, 2003.

[18] Iaccarino, G., "Quantification of Uncertainty in Flow Simulations Using Probabilistic Methods," VKI Lecture Series, Sept. 8-12, 2008.

[19] Roy, C. J., and Oberkampf, W. L., "A Comprehensive Framework for Verification, Validation, and Uncertainty Quantification in Scientific Computing," Comput. Methods Appl. Mech. Engrg., vol. 200, pp. 2131-2144, 2011.

[20] Lockwood, B. A., "Gradient-Based Approaches for Sensitivity Analysis and Uncertainty Quantification within Hypersonic Flows," PhD thesis, University of Wyoming, 2012.

[21] Sandor, Z., and Andras, P. "Alternative Sampling Methods for Estimating Multivariate Normal Probabilities," Econometric Institute Report EI 2003,05

[22] Xiu, D., Hesthaven, J.S., "High Order Collocation Methods for the Differential Equations with Random Inputs," SIAM J. Sci. Comput. vol. 27, pp. 1118-1139, 2005.

[23] Keryszig, E., Advanced Engineering Mathematics. Wiley, New York, 1979.

[24] Liu, Q., and Pierce, D., "A Note on Gauss-Hermite Quadrature," Biometrika, vol. 81, no. 3, pp. 624-629, 1994.

[25] Maître, O. L., and Knio, O., Spectral Methods for Uncertainty Quantification. Springer, 2010.

[26] Broomhead, D. and Lowe, D., "Multivariable Functional Interpolation and Adaptive Networks," Complex Systems, vol. 2, pp. 321–355, 1988.

[27] Gunn, S. R., "Support Vector Machines for Classification and Regression," Tech. Rep., University of Southampton, Tech. Rep., 1998.

[28] Hosder, S., and Walters, R. W., "Non-Intrusive Polynomial Chaos Methods for Uncertainty Quantification in Fluid Dynamics," 48^{th} AIAA Aerospace Sciences Meeting, AIAA 2010-129.

[29] Alexeenko, A., Weaver, A., Greendyke, R., and Camberos, J., "Flowfield Uncertainty Analysis for Hypersonic CFD Simulations," in 48^{th} AIAA Aerospace Sciences Meeting, AIAA, 2010-1180.

[30] Kawai, S., and Shimoyama, K., "Kriging-Model-Based Uncertainty Quantification in Computational Fluid Dynamics," 32^{nd} AIAA Applied Aerodynamics Conference, AIAA Aviation, AIAA 2014-2737.

[31] Peter, J., and Marcelet, M., “Comparison of Surrogate Models for Turbomachinery Design,” WSEAS Transactions on Fluid Mechanics, vol. 3, no. 1, pp. 10–17, 2008.

[32] Laurenceau, J., and Sagaut, P., “Building Efficient Response Surfaces of Aerodynamic Functions with Kriging and Cokriging,” AIAA Journal, vol. 46, no. 2, pp. 498–507, 2008.

[33] Laurenceau, J., and Meaux, M., “Comparison of Gradient and Response Surface Based Optimization Frameworks Using Adjoint Method,” in 49^{th} AIAA/ASME/ASCE/AHS/ASC Structures, Structural Dynamics, and Materials Conference, Schaumburg, IL, April 2008, AIAA Paper, 2008-1889.

[34] Baeder, J. D., and Srinivasan, G. R., “Turns: A Free-Wake Euler/Navier-Stokes Numerical Method for Helicopter Rotors,” AIAA Journal, vol. 31, no. 5, pp. 959–962, 1993.

[35] Spalart, P. R., and Allmaras, S. R., “A One-Equation Turbulence Model for Aerodynamic flows,” Recherche Aerospatiale, vol. 1, pp. 5–21, 1994.

[36] Lakshminarayan, V. K., “Computational Investigation of Micro-Scale Coaxial Rotor Aerodynamics in Hover,” PhD thesis, University of Maryland College Park, 2009.

[37] Van Leer, B., “Towards the Ultimate Conservative Difference Scheme: V. A Second-Order Sequel to Godunov’s Method,” Journal of Computational Physics, vol. 135, no. 2, pp.229–248, 1997.

[38] Koren, B., “Upwind Schemes, Multigrid and Defect Correction for the Steady Navier-Stokes Equations,” In Proceedings of the 11^{th} International Conference on Numerical Methods in Fluid Dynamics, 1988.

[39] Roe, P., “Approximate Riemann Solvers, Parameter Vectors and Difference Schemes,” Journal of Computational Physics, vol. 135, no. 2, pp. 250–258, 1997.

[40] Hirsch, C., Numerical Computation of Internal and External Flows, Vol. 2, Wiley Publishers, 1990.

[41] Boussinesq, J., “Essai Sur la The’orie des eaux Courantes,” Mem. Pres. Acad. Sci., XXIII, 46, Paris, 1877.

[42] Boussinesq, J., “Theorie de I’ Ecoulement Tourbillonant et Tumubteur des Liquides Dans les Lits Rectiligues,” Comptes Rendus de 1’ Acad. des Sciences, CXXII, pp. 1293, 1896.

[43] Pulliam, T. H., and Chaussee, D. “A Diagonal Form of an Implicit Approximate Factorization Algorithm,” Journal of Computational Physics, vol. 39, no. 2, pp.347–363, 1981.

[44] Iserles, A., A First Course in the Numerical Analysis of Differential Equations, Cambridge University Press, 1996.

[45] White, F. M., Viscous Fluid Flow, McGraw-Hill, 3^{rd} edition, 2005.

[46] MATLAB, “Piecewise Cubic Hermite Interpolating Polynomial (PCHIP),” MATLAB version 9.2.0 (R2017a) Documentation, The MathWorks Inc., Natick, 2017.

[47] Hand, M. M., Simms, D. A., Fingersh, Jager, D. W., Cotrell, J. R., Schreck, S., and Lawood, S. A., "Unsteady Aerodynamics Experiment Phase VI: Wind Tunnel Test Configurations and Available Data Campaigns," Technical Report TP-500-29955, NREL, 2001.

[48] Leishman, J. G., Principles of Helicopter Aerodynamics. Cambridge University Press, 2^{nd} edition, 2002.

[49] Noonan, K., "Aerodynamic Characteristics of Two Rotorcraft Airfoils Designed for Application to the Inboard Region of a Main Rotor Blade," Technical Paper TP-3009, NASA, 1990.

[50] Somers, D. M., "Design and Experimental Results for the S809 Airfoil," NREL/SR-440-6918, Jan. 1997.

[51] Vos, R., and Farokhi, S., Introduction to Transonic Aerodynamics, Vol. 110, Springer, 2015.